# Defect chemistry of mixed conducting perovskites: Interplay of protonic defects, oxygen vacancies and electron holes

Von der Fakultät Chemie der Universität Stuttgart
zur Erlangung der Würde eines Doktors der
Naturwissenschaften (Dr. rer. nat.) genehmigte Abhandlung

Vorgelegt von
**Giulia Raimondi**
aus Mussomeli, Italien

Hauptberichter: Prof. Dr. Joachim Maier
Mitberichter: Prof. Dr. Thomas Schleid
Prüfungsvorsitzender: Prof. Dr. Joris Van Slageren
Tag der mündlichen Prüfung: 28.04.2022

Max-Planck-Institut für Festkörperforschung
2022

*"Gli dissi che non mi pareva giusto che il mondo sapesse tutto di come vive*
*il medico, la prostituta, il marinaio, l'assassino, la contessa, l'antico romano,*
*il congiurato e il polinesiano,*
*e nulla di come viviamo noi trasmutatori di materia;*
*ma che in questo libro avrei deliberatamente trascurato la grande chimica,*
*la chimica trionfante degli impianti colossali e dei fatturati vertiginosi,*
*perché questa è opera collettiva e quindi anonima.*
*A me interessavano di più le storie della chimica solitaria,*
*inerme e appiedata,*
*a misura d'uomo,*
*che con non poche eccezioni è stata la mia:*
*ma è stata anche la chimica dei fondatori,*
*che non lavoravano in équipe ma soli,*
*in mezzo all'indifferenza del loro tempo,*
*per lo più senza guadagno,*
*e affrontavano la materia senza aiuti,*
*col cervello e con le mani,*
*con la ragione e la fantasia."*

Primo Levi – Il Sistema Periodico

## Erklärung über die Eigenständigkeit der Dissertation

Ich versichere, dass ich die vorliegende Arbeit mit dem Titel *Defect chemistry of mixed conducting perovskites: Interplay of protonic defects, oxygen vacancies and electron holes* selbständig verfasst und keine anderen als die angegebenen Quellen und Hilfsmittel benutzt habe; aus fremden Quellen entnommene Passagen und Gedanken sind als solche kenntlich gemacht.

## Declaration of Authorship

I hereby certify that the dissertation entitled *Defect chemistry of mixed conducting perovskites: Interplay of protonic defects, oxygen vacancies and electron holes* is entirely my own work except where otherwise indicated. Passages and ideas from other sources have been clearly indicated.

Name/Name: Giulia Raimondi

Unterschrift/Signed: _____

Datum/Date:

# Acknowledgements

I greatly thank all the people contributing to this dissertation's work.

First, I really thank Prof. Joachim Maier for giving me the opportunity to join his department at the Max Planck Institute for Solid State Research, as a Ph.D. student and working in this highly stimulating research (and also social) environment.

I thank Prof. Schleid and Prof. Van Slageren for revising my thesis and being part of the examination committee. Additionally, I thank Prof. Van Slageren also for being my mentor in the Mentor-Mentee framework set by the Athena Group MPI-FKF, his advice have been precious.

I also thank Dr. Jürgen Nuss for taking part of my three Annual Thesis Committee meeting and his valuable comments.

A sincere thank goes to my daily supervisor, Dr. Rotraut Merkle, who has been my scientific guide and patiently taught me to ask myself the right questions when doing research. I greatly thank her for all of her time spent in stimulating experimental discussions, proof-readings of the thesis, papers and presentations.

I am grateful to Prof. Maier's secretaries Sofia Weiglein and Madeleine Burkhardt, and the IMPRS coordinators Dr. Hans George Libuda, Dr. Eva Benckiser for the great administrative support.

Many thanks to Dr. Helga Hoier, who measured all the XRD patterns included in this thesis. Thanks also to the technician of the department, Florian Kaiser, Udo Klock, Annette Fuchs, Armin Sorg and Uwe Traub for been always available when some sort of technical issue arose, you all teach me a lot of useful things that can also be applied to everyday life.

The crystal preparation group, in particular Barbara Baum, is also thanked for their effort in several samples preparation. I'm also grateful for all the ICP-OES measurements performed by Samir Hammoud.

I also thank our collaborators in the synchrotron-based research projects included in this thesis: Dr. Alessandro Longo, Prof. Francesco Giannici, Dr. Alessandro Chiara, Prof. Antonino Martorana, Dr. Christoph Sahle, Dr. Chiara Cavallari, Dr. Olivier Mathon.

I am also particularly grateful to have shared, partially or entirely, my time in MPI with amazing and cheerful colleagues and friends, here reported in no particular order: Dr. Yuanye Huang, Dr. Markus Joos, Dr. Christian Berger, Dr. Robert Usiskin, Dr. Davide

Moia, Dr. Jelena Popovic-Neuber, Dr. Igor Moudrakovski, Dr. Eugene Kotomin, Dr. Klaus Dieter Kreuer, Dr. Matteo Minola, Dr. Davide Betto, Dr. Alessandro Senocrate, Dr. Andreas Muenchinger, Dr. Torben Saatkamp, Dr. Pinar Kaya, Dr. Gee Yeong Kim, Dr. Gints Kucinskis, Dr. Ashkan Moradabadi, Dr. Reihaneh Zohourian, Dr. Anna Niemczyk, Dr. Simon Longer, Dr. Maximilian Hoedl, Dr. Maximilian Schaube, Dr. Maryam Noyabee, Kyungmi Lim, Ya-ru Wang, Chuanlian Xiao, Mina Jung.

I also express my gratitude also to my life-long friends, Manuela Ingrasci and Claudia Pardi; my new friends, my flatmate Paola Forte and my boyfriend for their invaluable support over these past years.

Last but not least, a big thank you goes to my family, my grandmother, those who are still here and those who are not anymore, for supporting me and putting a real effort in understanding what I am actually doing. Finally, I thank my beloved parents, Luigi and Carmela, for always believing in me and for teaching me that I could be whoever I wanted to be.

# Abstract

Mixed conducting oxides are key functional materials for clean energy technologies, and their chemical and electrical properties need to be carefully tuned to optimize the device performance. They can be employed as cathodes for Protonic Ceramic Fuel Cells (PCFCs) which work at intermediate temperatures (400-600 °C), bridging the gap between polymer membrane and solid oxide fuel cells. A cathode with mixed hole, oxygen vacancy, and proton conductivity extends the reactive zone for the oxygen reduction to water beyond the triple phase boundary, making the whole cathode surface an active electrocatalyst. The defect chemistry (concentrations and mobilities of point defects) of such materials with three charge carriers is complex, and some of the desired properties for a PCFC cathode materials are in mutual conflict (*i.e.,* proton uptake, electronic conductivity, catalytic activity, long-term chemical stability).

The present thesis deals with fundamental questions such as the relation between proton uptake and structural and electronic properties, or point defect interactions. It also aims at extending the experimental data basis by varying the cation stoichiometry in $BaFeO_{3-\delta}$-based perovskites. Protons are incorporated into $BaFeO_{3-\delta}$-based perovskites via hydration at expense of oxygen vacancies (acid-base reaction), or by hydrogen uptake at expense of holes (redox reaction). Their concentration can be determined by thermogravimetric analysis (TGA). Doping has strong effects on the materials properties. Acceptor dopants directly affect defect concentrations via the electroneutrality condition, increasing the oxygen vacancy and/or hole concentration. In addition, oversized B-site dopants such as $Zn^{2+}$, $Mg^{2+}$, $Ca^{2+}$ and $Y^{3+}$ can lead to local distortions, which furthermore affect the electronic structure.

This thesis comprises three groups of materials, they are investigated with a combination of methods to obtain a comprehensive understanding of their defect chemistry.

The first part investigates the effect of oversized $Zn^{2+}$ and $Y^{3+}$ substituting 20% of iron in $(Ba,La,Sr)FeO_{3-\delta}$. These dopants are found to increase the proton uptake compared to the undoped composition. This study reveals a complex interplay of cation composition, structural distortion and electronic features affecting the hydration properties of these materials. Extended x-ray Absorption Fine Structure (EXAFS) analysis demonstrates that a high degree of disorder corresponding to B-O-B buckling is present in reduced samples, and for Zn,Y- doped samples even in oxidized state. This is also supported by the Fe *K*-edge x-ray Absorption Near Edge Spectroscopy (XANES). For doped and reduced samples the spectra can be simulated only when configurations with iron in strongly distorted 5-fold coordination geometry are used, compared to the

undoped composition. Moreover, the simulations for the O *K*-edge show that in reduced and Zn,Y -doped samples the TM*3d*-O*2p* hybridization is decreased relative to undoped $Ba_{0.95}La_{0.05}FeO_3$. This is reflected in the semiempirical parameters termed *screening* and *dilatorb* which are used for simulating the experimental spectra. The B-O-B buckling directly decreases the Fe-O bond covalency because of a less effective Fe*3d*-O*2p* orbitals overlap. This also decreases the hole transfer from iron to oxygen, leaving more negative oxide ions with more basic character, which are more favourable for proton attachment. This relation helps to understand the proton uptake reported for Y, Zn-doped compositions. These considerations on the interplay of chemical, geometrical, and electronic structure features and their effect on the proton uptake can be extended to a larger range of compositions, and therefore serve as guidelines for further PCFC cathode material optimization.

The second part deals with the solid solution series $BaZr_{0.88-x}Fe_xY_{0.12}O_{3-\delta}$ ($0 \leq x \leq 0.8$), which ranges from electrolyte-type materials for low Fe content to cathode-type materials for large x. This series is investigated using TGA, EXAFS, XRS, Electrochemical Impedance (EIS) and UV-Vis Spectroscopy. The Fe-content strongly influences the electronic structure and the proton uptake: already 10% of iron leads to the formation of an impurity band, and decreases the degree of hydration by one order of magnitude. Enthalpy and entropy of the hydration reaction show systematic variations with x. The partial proton, oxygen vacancy and hole conductivities are determined using an oxygen-pump integrated EIS setup. The protonic conductivity decreases by more than one order of magnitude when increasing the iron content, with values ranging between $\approx 10^{-5}$-$10^{-6}$ S/cm. This would still allow the activation of the bulk path in a PCFC cathode. The decrease of the proton conductivities in iron rich samples is to a larger share caused by a decrease in the proton mobilities, and to a smaller degree by the decreased proton concentration.

The proton migration activation energies are hardly affected by the modified hydration thermodynamics, and remain in the range of 0.39-0.5 eV, still relatively close to the value reported for $BaZr_{0.9}Y_{0.1}O_{2.95}$ (0.43 eV). The oxygen non-stoichiometry measurements clearly demonstrate the appearance of a non-negligible hole-hole interaction in iron rich samples. O *K*-edge (XRS) measurements show an increase of Fe*3d*-O*2p* hybridization with increasing amount of iron. This is beneficial for the electronic conductivity of the material, leading to percolation phenomena: for more than 10% of iron the electronic conductivity as well as the hole mobility increase steeply (the migration barrier for hole polaron hopping in a $FeO_6$ sub-lattice is smaller than for Fe centers in a $ZrO_6$ matrix). Regarding the structural analysis, the cations' local

environment is not impacted below 10% of iron doping. For heavily iron-doped samples the buckling of the B-O-B connections starts to appear. Moreover, for very high iron content (>0.3) the oxygen vacancies tend to cluster around iron. EIS measurements in the oxygen pump indicate that percolation phenomena are relevant also for the diffusion of protons and oxygen vacancies, but only at higher iron doping concentration ([Fe]>0.3).

In the third part, the effect of B-site doping with first row transition metals is explored (Mn, Co, Ni, Cu, Zn), focusing on proton uptake and electronic conductivity. This is important because the electronic conductivity of $BaFeO_{3-\delta}$-based perovskites is at the lower end of the desired range for an electrode material. It is found that Zn and Ni doping favor the proton uptake, also copper is slightly beneficial for the hydration. Co, Ni, and Cu improve the electronic conductivity. This yields two correlation lines when plotting the proton uptake versus $\sigma_{eon}$: (i) Zn and Co doped $Ba_{0.95}La_{0.05}FeO_{3-\delta}$ show a negative correlation, (ii) Cu and Ni doped samples show a positive correlation. This demonstrates that just using the TM-O bond covalency as a single descriptor does not suffice for the hydration behavior of triple conductors, and further effects need to be considered. The covalency is the dominating effect for Co-doped composition, which show high TM-O bond covalency and low proton uptake because of decreased oxide ion basicity. This correlation applies also for Zn-doped samples where local distortions strongly decrease the TM-O bond covalency resulting in higher proton uptake. However, it fails for Ni, Cu-doped samples. In the latter compositions, the high *d* orbital occupancy disfavors the O→TM electron transfer, preserving the basicity of the oxide ion (*i.e.,* favoring proton uptake) even if the TM-O bond covalency is high.

The last part of this thesis deals with the hydration properties of several perovskite-related crystal structures. It is proven that the proton uptake decreases in the order cubic perovskite > hexagonal perovskite > orthorhombic structures/superstructures such as $Ba_2Fe_2O_5$). This is caused by several effects such as $BO_6$ octahedra connectivity (corner sharing, face sharing), oxygen vacancy ordering, and TM-O bond covalency.

Summarizing, this thesis provides a systematic study of the interplay of cation composition, geometrical and electronic structure in triple conducting oxides and the resulting effects on the concentration and mobility of the relevant defects (protonic defects, oxygen vacancies and electron holes). The understanding obtained from disentangling these effects can be helpful in optimizing the composition and the performance of PCFC cathode materials.

# ZUSAMMENFASSUNG

Gemischtleitende Oxide sind wichtige Funktionsmaterialien für saubere Energietechnologien, und ihre chemischen und elektrischen Eigenschaften müssen sorgfältig abgestimmt werden, um die Leistung entsprechender Bauteile zu optimieren. Sie können als Kathoden für protonenleitende keramische Brennstoffzellen (PCFC) eingesetzt werden, die bei mittleren Temperaturen (400-600 °C) arbeiten und die Lücke zwischen Polymermembran- und Festoxidbrennstoffzellen schließen. Eine Kathode mit gemischter Loch-, Sauerstoffleerstellen- und Protonenleitfähigkeit erweitert die reaktive Zone für die Sauerstoffreduktion zu Wasser über die Dreiphasengrenze hinaus, und aktiviert die gesamte Kathodenoberfläche für die katalysierte Reaktion. Die Defektchemie (Konzentrationen und Mobilitäten von Punktdefekten) solcher Materialien mit drei Ladungsträgern ist komplex, und einige der gewünschten Eigenschaften für ein PCFC-Kathodenmaterial stehen in gegenseitigem Konflikt.

Die vorliegende Arbeit befasst sich mit grundlegenden Fragen wie dem Zusammenhang zwischen Protonenaufnahme und strukturellen und elektronischen Eigenschaften sowie Punktdefektwechselwirkungen. Sie strebt außerdem eine Erweiterung der experimentellen Datenbasis durch Variation der Kationenstöchiometrie in $BaFeO_{3-\delta}$-basierten Perowskiten an. Protonen werden in $BaFeO_{3-\delta}$-basierte Perowskite durch Hydratisierung auf Kosten von Sauerstoffleerstellen (Säure-Base-Reaktion) oder durch Wasserstoffaufnahme auf Kosten von Löchern (Redoxreaktion) eingebaut. Ihre Konzentration kann durch thermogravimetrische Analyse (TGA) bestimmt werden. Die Dotierung hat starke Auswirkungen auf die Materialeigenschaften. Akzeptordotierungen wirken einerseits durch die Elektroneutralitätsbedingung (Erhöhung von Sauerstoffleerstellen und/oder Löchern). Darüber hinaus können B-Platz-Dotierungen wie $Zn^{2+}$, $Mg^{2+}$, $Ca^{2+}$ und $Y^{3+}$ mit deutlich größerem Ionenradius als $Fe^{3+/4+}$ zu lokalen Verzerrungen führen, die wiederum die elektronische Struktur beeinflussen.

Drei Materialgruppen bilden den Hauptteil dieser Arbeit, sie werden mit einer Kombination von Methoden untersucht, um ein umfassendes Verständnis ihrer Defektchemie zu erlangen.

Im ersten Teil wird die Wirkung der übergroßen $Zn^{2+}$- und $Y^{3+}$-Dotierionen untersucht wenn sie 20 % des Eisens in $(Ba,La,Sr)FeO_{3-\delta}$ ersetzen. Es wurde festgestellt, dass diese Dotierungen die Protonenaufnahme im Vergleich zur undotierten Zusammensetzung erhöhen. Dies zeigt ein komplexes Zusammenspiel von Kationenzusammensetzung, struktureller Verzerrung und elektronischen Eigenschaften,

die die Hydratationseigenschaften dieser Materialien beeinflussen. EXAFS-Analyse (Extended x-ray Absorption Fine Structure) zeigt, dass in reduzierten Proben mit hoher Sauerstoffleerstellenkonzentration ein hoher Grad an Unordnung vorliegt, der gewinkelten B-O-B-Verbindungen entspricht, und dass dies bei Zn,Y-dotierten Perowskiten sogar für oxidierte Proben gilt. Dies wird auch durch die Daten der Röntgenabsorptions-Nahkanten-Spektroskopie (XANES) an der Fe *K*-Kante bestätigt. Für dotierte und reduzierte Proben können die Spektren nur simuliert werden, wenn stark verzerrte Konfigurationen mit 5-fach koordiniertem Eisen stärker gewichtet werden als für undotierte Proben. Darüber hinaus zeigen die Simulationen der O *K*-Kanten-Spektren, dass in reduzierten und Zn,Y-dotierten Proben die TM*3d*-O*2p* Hybridisierung im Vergleich zu undotiertem $Ba_{0,95}La_{0,05}FeO_3$ verringert ist. Dies spiegelt sich in den semiempirischen Parametern *screening*- und *dilatorb* wieder, die für die Simulation der gemessenen Spektren verwendet werden. Die gewinkelte B-O-B-Verbindung verringert die Kovalenz der Fe-O-Bindung, da die *3d-2p* Orbitale weniger effektiv überlappen. Dadurch verringert sich auch der Loch-Transfer von Eisen zu Sauerstoff, so dass stärker negativ geladene Oxidionen (mit verstärkt basischem Charakter) vorliegen, die eine Protonenanlagerung begünstigen. Dies hilft, die für Y,Zn-dotierte Proben beobachtete erhöhte Protonenaufnahme zu verstehen. Diese Überlegungen zum Zusammenspiel chemischer, geometrischer und elektronischer Strukturmerkmale und deren Auswirkungen auf die Protonenaufnahme können auf eine größere Gruppe von Zusammensetzungen ausgedehnt und als Leitlinien für die weitere Optimierung von PCFC-Kathodenmaterialien verwendet werden.

Der zweite Teil behandelt die Mischkristallreihe $BaZr_{0.88-x}Fe_xY_{0.12}O_{3-\delta}$ ($0<x<0.8$), die von elektrolytartigen Materialien mit niedrigem Fe-Gehalt bis zu kathodenartigen Materialien mit hohem Fe-Gehalt reicht. Die Reihe wird mittels TGA, EXAFS, XRS, elektrochemischer Impedanz (EIS) und UV-Vis-Spektroskopie untersucht. Der Fe-Gehalt hat einen starken Einfluss auf die elektronische Struktur und die Protonenaufnahme: bereits 10 % Eisen führen zur Bildung eines Verunreinigungs-Bands und verringern den Hydratisierungsgrad um eine Größenordnung. Enthalpie und Entropie der Hydratationsreaktion variieren systematische mit dem Eisengehalt. Die partiellen Protonen-, Sauerstoffleerstellen- und Lochleitfähigkeiten wurden mittels EIS in einer elektrochemischen Sauerstoffpumpe bestimmt. Die Protonenleitfähigkeit nimmt um mehr als eine Größenordnung ab, wenn der Eisengehalt steigt, wobei die Werte zwischen $\approx 10^{-5}$-$10^{-6}$ S/cm liegen. Dies würde immer noch die Aktivierung der gesamter Oberfläche in einer PCFC-Kathode ermöglichen. Die Abnahme der Protonenleitfähigkeiten in

eisenreichen Proben ist zu einem größeren Teil auf die Abnahme der Protonenmobilitäten zurückzuführen, zu einem kleineren Teil auf die verringerte Mobilität.

Die Aktivierungsenergien der Protonenmigration werden kaum durch die veränderte Thermodynamik der Hydratisierung beeinflusst, und bleiben mit Werten von 0.39-0.5 eV nahe am Wert von 0.43 eV für das $BaZr_{0.9}Y_{0.1}O_{2.95}$-Elektrolytmaterial. Messungen der Sauerstoff-Nichtstöchiometrie zeigen, dass in eisenreichen Proben eine nicht vernachlässigbare Loch-Loch-Wechselwirkung besteht. Die O *K*-Kanten-Spektroskopie (XRS) zeigt eine wachsende Fe*3d*-O*2p* Hybridisierung mit zunehmendem Eisengehalt. Dies erhöht die elektronische Leitfähigkeit des Materials und führt zu Perkolationsphänomenen: Bei mehr als 10 % Eisen steigen die elektronische Leitfähigkeit und die Mobilität der Löcher steil an (die Migrationsbarriere für das *polaron hopping* der Löcher in einem $FeO_6$-Gitter ist kleiner als für Fe-Zentren in einer $ZrO_6$-Matrix). Bei einer Eisendotierung von weniger als 10% wird die lokalen Umgebungen der Kationen strukturell nicht verändert. Bei eisenreichen Proben stellt sich ein Abknicken der B-O-B-Bindungen ein. Bei einem sehr hohen Eisengehalt (>0.3) neigen die Sauerstoffleerstellen außerdem dazu, sich bevorzugt um das Eisen anzuordnen. Mit EIS-Messungen in der Sauerstoffpumpe konnte für fast alle Proben der Beitrag der verschiedenen Ladungsträger zur Leitfähigkeit in diesen dreifach leitenden Oxiden aufgetrennt werden. Perkolationsphänomen werden auch für die Diffusion von Protonen und Sauerstoffleerstellen beobachtet, allerdings bei höherer Eisendotierung ([Fe]>0.3) als im Fall der elektronischen Leitfähigkeit ([Fe]>0.1).

Im dritten Teil werden die Auswirkungen der B-Platz-Dotierung mit Übergangsmetallen der ersten Reihe (Mn, Co, Ni, Cu, Zn) untersucht, wobei der Schwerpunkt auf der Protonenaufnahme und der elektronischen Leitfähigkeit liegt. Dies ist wichtig, da die elektronische Leitfähigkeit von $BaFeO_{3-\boldsymbol{\delta}}$-Perowskiten am unteren Ende des für ein Elektrodenmaterial gewünschten Bereichs liegt. Die Dotierung mit Zn und Ni begünstigt die Protonenaufnahme, auch Kupfer ist vorteilhaft für die Hydratisierung. Co, Ni und Cu fördern die elektronische Leitfähigkeit. Dies ergibt zwei Korrelationslinien zwischen Protonenaufnahme und $\sigma_{eon}$: (i) Zn- und Co-dotiertes $Ba_{0.95}La_{0.05}FeO_{3-\delta}$ zeigen eine negative Korrelation, (ii) Cu- und Ni-dotierte Proben zeigen eine positive Korrelation. Dies zeigt, dass die Kovalenz der Übergangsmetall-Sauerstoff-Bindung (TM-O) als alleiniges Kriterium für die Hydratisierung von kombinierten Protonen/Sauerstoffleerstellen/Löcherleitern nicht ausreicht und weitere Effekte berücksichtige werden müssen. Das Kovalenzkriterium dominiert für Co-dotierte Zusammensetzungen, die eine hohe TM-O-Kovalenz und eine niedrige

Protonenaufnahme wegen der verringerte Basizität der Oxidionen aufweisen. Diese Korrelation gilt auch für Zn-dotierte Proben, in denen die lokale Verzerrung die TM-O-Kovalenz stark verringert, was zu einer höheren Protonenaufnahme führt. Sie versagt jedoch bei Ni,Cu-dotierten Proben. In diesen unterdrückt die hohe d-Orbitalbesetzung den O→TM Elektronentransfer weitgehend, wodurch die Basizität der Oxidionen und damit die hohe Protonenaufnahme trotz hoher TM-O-Kovalenz erhalten bleiben.

Der letzte Teil dieser Arbeit befasst sich mit der Hydratisierung verschiedener Perowskit-verwandter Kristallstrukturen. Es wird gezeigt dass die Protonenaufnahme in der Reihe kubischer Perowskit > hexagonaler Perowskit > orthorhombische Struktur/Überstruktur wie $Ba_2Fe_2O_5$ abnimmt. Dies wird durch mehrere Effekte verursacht, wie die Konnektivität der $BO_6$-Oktaeder (ecken- oder flächenverknüpft), die Ordnung der Sauerstoffleerstellen zu Überstrukturen und Unterschiede in der TM-O-Kovalenz.

Diese Arbeit liefert eine systematische Untersuchung des Zusammenwirkens von Kationenzuammensetzung und geometrischer sowie elektronischer Struktur in gemischtleitenden Oxiden, und ihrer Auswirkungen auf die Konzentration und Beweglichkeit der relevanten Defekte (Protonen, Sauerstoffleerstellen, Löcher). Das dabei erreichte tiefergehende Verständnis der einzelnen Effekte kann zur weiteren Optimierung von PCFC-Kathodenmaterialien genutzt werden.

# Contents

# List of acronyms and symbols

| | |
|---|---|
| **FC** | Fuel Cell |
| **EC** | Electrolyser Cell |
| **PCFC** | Proton Ceramic Fuel Cell |
| **SOFC** | Solid Oxide Fuel Cell |
| **PLD** | Pulsed Laser Deposition |
| **TPB** | Triple Phase Boundary |
| **ORR** | Oxygen Reduction reaction |
| **MIEC** | Mixed Ionic Electronic Conductor |
| **TM** | Transition Metal |
| **XRD** | X-Ray Diffraction |
| **ICP-OES** | Inductively Coupled Plasma – Optical Emission Spectroscopy |
| **TG** | Thermogravimetry |
| **TGA** | Thermogravimetric Analysis |
| **XAS** | X-Ray Absorption Spectroscopy |
| **XRS** | X-Ray Raman Scattering |
| **MS** | Mass spectrometry |
| $K_{hydr}$ | Mass action constant for the hydration reaction |
| $K_{ox}$ | Mass action constant for the oxygenation reaction |
| **XANES** | X-ray Absorption Near Edge Spectroscopy |
| **EXAFS** | Extended X-Ray Absorption Fine Structure |
| **FT** | Fourier Transform |
| $\sigma_{eon}$ | Electronic conductivity |
| $\sigma_{ion}$ | Ionic conductivity |
| $\sigma$ | Electrical conductivity |
| **EIS** | Electrochemical Impedance Spectroscopy |
| **YSZ** | Yttria-Stabilized Zirconia |
| $p_c$ | Critic percolation |

# 1 Introduction

## 1.1 Protonic Ceramic Fuel Cells

The necessity of a decarbonised energy sector as well as the awareness of the environmental crisis are growing. This requires developing a future energy grid using renewable and clean energy carriers (*e.g.,* hydrogen). The intermittent character of most of the renewable energy sources (*e.g.,* solar, wind, etc…) could be overcome by the storage of the surplus energy using batteries (limited capacities), or electrolyser cells for green hydrogen production (large capacities, long time storage). Regarding the latter, hydrogen has the power of playing a central role in the smart grid, as (i) an energy vector, (ii) a storage medium and (iii) a clean fuel.

Hydrogen is a key gas in fuel cells (FC) and in electrolyser cells (EC). FCs are devices for highly efficient conversion of chemical to electrical energy using electrochemical reactions. A variety of fuel cells exists, which operate at different temperatures, using different materials. This thesis will focus on protonic ceramic fuel cells (PCFC) which are based on solid oxide proton conductor materials, and thus can operate at intermediate temperatures (400-600 °C) bridging the gap between the already established, low temperature and high temperature FC technologies (see **Figure 1**).

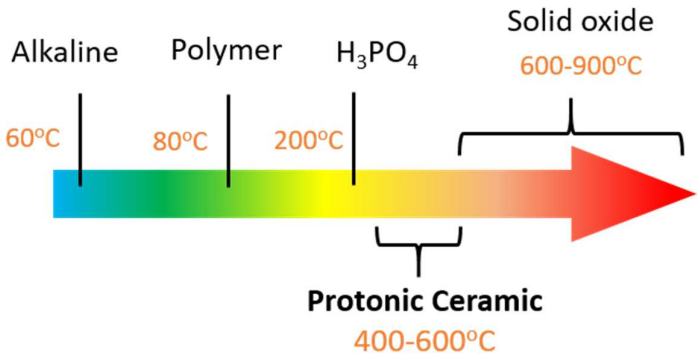


**Figure 1** Operation temperatures of the available FCs technologies.

A PCFC is composed of three main parts: (i) anode where the hydrogen fuel is oxidized to protons, (ii) solid electrolyte which is a protons conductor, (iii) cathode where the oxygen reduction from air occurs and water vapour is released. The two redox reactions,

at the electrodes, force electrons into an external circuit. This is summarized in the scheme in **Figure 2**.

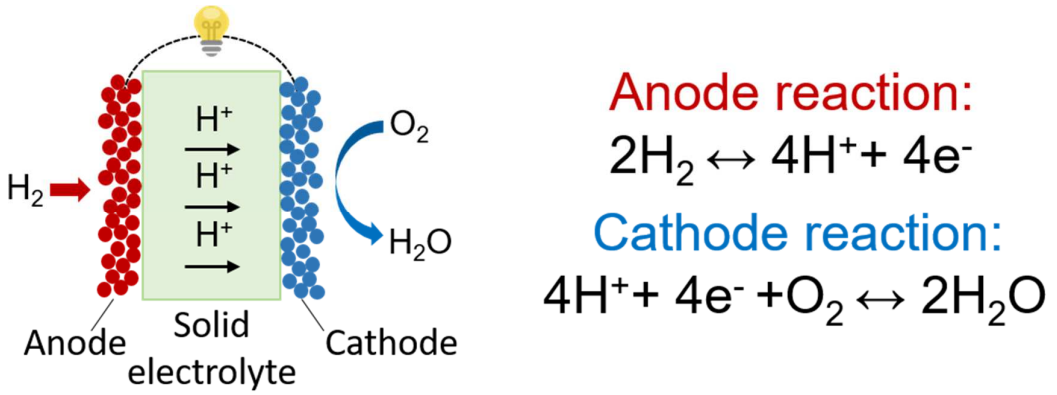


**Figure 2** Scheme of a PCFC highlighting the fundamental constituents. Electricity is produced by the electrochemical reactions occurring at the anode and at the cathode, which inject electronic carriers into the outer circuit.

PCFCs have notable advantages with respect to their 'parent technology' Solid Oxide Fuel Cell based on oxide ion conducting electrolytes (SOFC): (i) A lower operation temperature is enabled thanks to the lower activation energy for proton transport compared to oxide ion transport, which will decrease degradation processes. (ii) Water is produced at the cathode side, therefore the $H_2$ fuel is not diluted allowing for high fuel utilization.

PCFC are based on proton conducting oxides. These are typically simple perovskites $ABO_3$. Occasionally also more complex structures were investigated (double perovskites, Ruddlesden-Popper, etc…), brownmillerites $A_2B_2O_5$, $LnBO_4$- type orthophosphates, ortho-niobates or ortho-tantalates (see refs. [1-3]).

In 1964, Francis Forat discovered proton conduction in $LaAlO_3$ [4]. Two years later the mechanism of proton formation via hydration was clarified by Wagner and Stotz [5]. Iwahara and collaborators' work brought forward the potential of acceptor-doped $(Ba,Sr)(Ce,Zr)O_3$ materials thanks to optimization of the material composition, synthetic routes, and fabrication processes [6-14]. A thorough understanding of the defect chemistry and transport properties is summarized in a review [1]. Despite considerable efforts, the poor sinterability of protonic ceramics and the blocking character of the grain boundaries still impeded the development of an applicable PCFC. New procedures were developed towards lower sintering temperatures and improved densification. The most successful

ones use sintering aids (ZnO, NiO, CuO and CoO) [15-16] and employ the developed Solid State Reactive Sintering (SSRS) [17-19]. In 2015, lab-scale PCFC with promising performance were fabricated, [20] and since then further progress has been made. **Figure 3** (taken from ref. [3]) summarizes some of the most outstanding recent results.

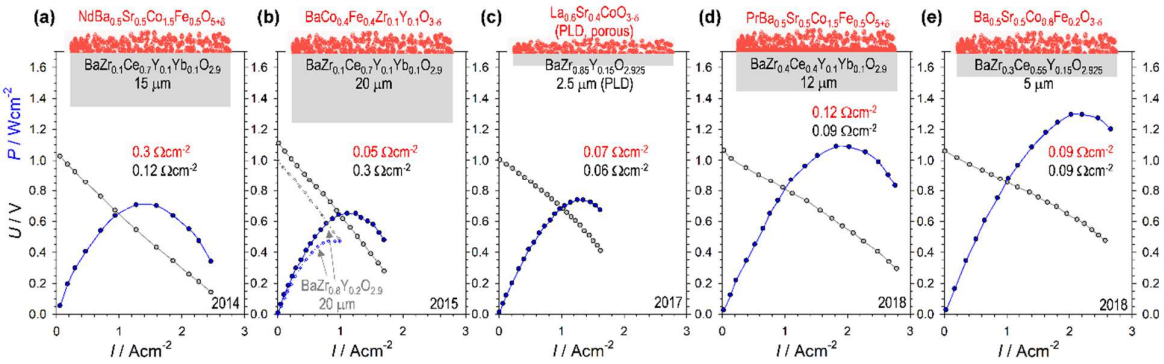


**Figure 3** Results for lab-scale PCFC at 600 °C, operated with air (cathode) and humid $H_2$ (anode). The anode is a Ni/electrolyte composite. The insets indicate the electrolyte and cathode materials, inset numbers give the area-specific resistances of electrolyte (black) and cathode (red) at open cell voltage. The cell voltage curves are in grey, the power density curves are in blue. Taken from [3].

*Materials used for the anode.* The anode material should be a mixed conductor for protons and electrons in order to efficiently catalyse the hydrogen oxidation reaction. The anode design for PCFC follows the one used for SOFC: a composite of the electrolyte materials mixed with an electron conductor (usually nickel based). It is important to maximize the Triple Phase Boundary (TBP, contact zone between gas phase, electrode and electrolyte) in order to achieve good performance. Usually the anode is also the mechanical support of the PCFC architecture.

*Materials used for the electrolyte.* The electrolyte material should be an electronically insulating proton conductor, stable in reducing and oxidizing conditions, and chemically compatible with the electrodes. The single phase material is sintered to a pore-free membrane to avoid gas leakage. The most common compositions are: $Ba(Zr,Y)O_{3-z}$, $Ba(Ce,Zr,Y)O_{3-z}$, $Ba(Ce,Zr,Y,Yb)O_{3-z}$. Earlier works used comparably high Ce contents which facilitate sintering and improve grain boundary conductivity, but induce long-term stability issues. The Ce content and electrolyte resistance could be decreased with improved processing, such as decreasing the thickness of the electrolyte.

*Cathode Materials for Proton Ceramic Fuel Cell.* The cathode side is often the bottleneck of the fuel cell. The oxygen reduction reaction (ORR) is kinetically more difficult than hydrogen oxidation, and causes major electrode polarization losses.

In general, a well-performing cathode material should have: (i) high electronic conductivity (>10 $Scm^{-1}$) to ensure fast charge transfer and current collection, (ii) good hydrothermal stability since water is formed at this side of the cell, (iii) high catalytic activity toward the ORR, (iv) chemical and mechanical compatibility with the electrolyte, (v) stability against secondary phases formation.

Regarding the possible paths for the ORR, two classes of cathode materials can be defined: (i) single conductors (electron holes) or mixed conductors (MIECs ,electron holes and oxygen vacancies) and (ii) triple conductors (electron holes, oxygen vacancies and protons). In the first class just the surface path is active for the ORR, therefore the active zone is restricted to the triple phase boundary. For the second class, an additional path (bulk path) is available in which protons are transported through the cathode material to the surface (**Figure 4**).

The surface path comprises: (1) Diffusion of the oxygen molecule toward the TPB; (2) Surface adsorption, reduction and dissociation of the oxygen molecule; (3) Proton diffusion from the electrolyte to the TPB; (4) Formation and desorption of the water molecule. In the bulk path, steps (1) and (2) are the same as in the surface path, but the third step consists of proton migration from the electrolyte through the cathode towards the surface adsorbed oxygen species. The water is formed there, and released to the gas phase. The advantage of the bulk path is that this extends the reactive zone beyond the TPB length and can make the whole cathode surface active for oxygen reduction. Already a proton conductivity in the range $10^{-6}$ - $10^{-4}$ S/cm suffices for activating the bulk path [21]. Therefore, a moderate proton conductivity is desirable for a well-performing cathode material.

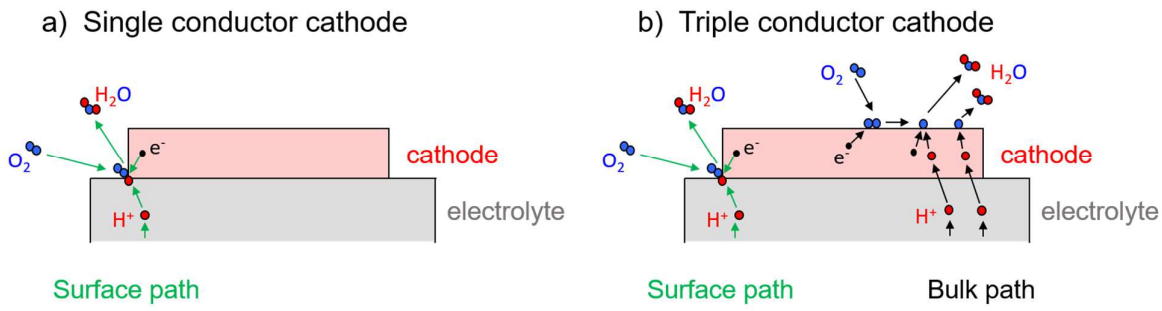


**Figure 4** ORR reaction steps for (a) single conductor or hole/vacancy conducting cathode, and (b) triple conductor cathode. The green arrows refer to the surface path, the black arrows refer to the bulk path. Adapted from [21].

PCFC cathode materials are typically perovskite or perovskite related materials with a transition metal (TM) in the B-site, and many are related to SOFC cathode materials. Some examples are: $Ba(Co,Fe,Zr)O_{3-\delta}$ [22] and $Ba(Co,Fe,Zr,Y)O_{3-\delta}$ [20] based on the well characterized MIEC $(Ba,Sr)(Co,Fe)O_{3-\delta}$ where Y and Zr doping stabilizes the cubic perovskite structure, and high barium content is beneficial for the proton uptake. Double perovskites $Nd(Ba,Sr)(Co,Fe)O_{5+\delta}$ and $Pr(Ba,Sr)(Co,Fe)O_{5+\delta}$ [23] showed very low electrode polarization resistance of 0.12 $\Omega/cm^2$ at 600 °C. $(Ba,La)(Fe,Zn)O_{3-\delta}$ [24] exhibits a high proton concentration of 10% per formula unit at 250 °C. Also some materials with different structure such as Ruddlesden-Popper [25] and Brownmillerite [26] are investigated. Another attempt in literature is to dope typical electrolyte composition with transition metals to induce electronic conduction [27]. These "in-between" compositions are explored since they have the potential to overcome the classical poor sinterability of the electrolyte material while obtaining a material with comparably high protonic conductivity. The materials investigated in the present thesis are presented in **Section 1.3**.

## 1.2 Defect formation in perovskites

Any deviation from the perfect atom arrangement in a crystal is called a defect. Defects are often introduced in a structure for changing its properties (mechanical, transport, electrical, etc…). Defects can be classified by their dimension: (i) 0-D or point defects, such as vacancies (atoms missing from their regular lattice sites), interstitials (atoms occupying interstitial voids), substitutional defects or dopants (atoms occupying the sites of a different element), Schottky defects, colour centres, Frenkel defects, polarons and excitons. (ii) 1-D defects such as edge and screw dislocations, (iii) 2-D defects such as stacking faults and grain boundaries. (iv) 3-D defects such as voids (pores) and

inclusions. The present thesis will focus on point defects since they are the most common in the investigated compositions, and their concentration can be equilibrated (in contrast *e.g.* to dislocations).

The most widely used nomenclature for describing point defects is the Kröger-Vink notation. In this notation the ion (or vacancy, V) presents a subscript which indicates the lattice site it occupies (*i.e.,* another ion position or an interstitial site, i) and a superscript which refers to the charge relative to the site the ion is occupying. Positive charges are indicated with bullets, negative ones with apostrophes, neutral with x. Therefore an oxygen vacancy which carries a double positive charge is written as $V_O^{\bullet\bullet}$ , a protonic defect, which is an hydroxide ion in an oxide ion site, as $OH_O^{\bullet}$.

Oxygen vacancies are key defects in this kind of materials, and they appear in the lattice when dopants with lower charge are introduced, or, in the case of cathode materials, when a transition metal cation is reduced. This is a combined consequence of electroneutrality and mass action.

The equilibration of an oxide with the surrounding oxygen gas atmosphere, which is a redox reaction, can be expressed as **Eq. 1**.

**Eq. 1** $$\frac{1}{2}\ O_2 + V_O^{\bullet\bullet} \rightleftarrows O_O^{x} + 2\ h^{\bullet} \qquad K_{ox} = \frac{[O_O^x][h^{\bullet}]^2}{\sqrt{pO_2}[V_O^{\bullet\bullet}]}$$

In humid gas, water can be dissociatively incorporated by a pure acid-base reaction (**Eq. 2**).

**Eq. 2** $$H_2O + O_O^x + V_O^{\bullet\bullet} \rightleftarrows 2OH_O^{\bullet} \qquad K_{hydr} = \frac{[OH_O^{\bullet}]^2}{pH_2O[O_O^x][V_O^{\bullet\bullet}]}$$

Another reaction that could occur is the hydrogenation reaction (**Eq. 3**): the combination of **Eq. 1** and **Eq. 2** describes the proton defect formation at expenses of holes. One expects that **Eq. 2** dominates for high $[V_O^{\bullet\bullet}]$ (electrolyte or cathode material in low $pO_2$), while **Eq. 3** prevails for high $[h^{\bullet}]$ (high $pO_2$, cathode materials).

**Eq. 3** $$H_2O + 2\ O_O^x + 2h^{\bullet} \rightleftarrows 2OH_O^{\bullet} + \frac{1}{2}\ O_2 \qquad K = \frac{\sqrt{pO_2}[OH_O^{\bullet}]^2}{pH_2O[O_O^x]^2[h^{\bullet}]^2}$$

Numerical calculations [28] give $[V_O^{\bullet\bullet}]/[h^{\bullet}]$ as quantitative criterion.

Combining the previous equations with the oxygen site balance (**Eq. 4**, for a $ABO_{3-\delta}$ perovskite) and the electroneutrality condition (**Eq. 5**), one can draw a "material map" (**Figure 5**) with the defects concentrations for different gas atmosphere and the mass action constants. This was done in ref. [28].

**Eq. 4** $$[O_O^x] + [V_O^{\bullet\bullet}] + [OH_O^{\bullet}] = 3$$

**Eq. 5** $$[Acc'] = 2[V_O^{\bullet\bullet}] + [h^{\bullet}] + [OH_O^{\bullet}]$$

Depending on the defect concentrations is possible to recognize different regimes and type of material. Proton and oxide ion conducting electrolytes show low $K_{ox}pO_2^{1/2}$ and they are located in the left and back corner of the plot. Mixed conductors (high $K_{ox}pO_2^{1/2}$) are located in the right and front corner of the material map.

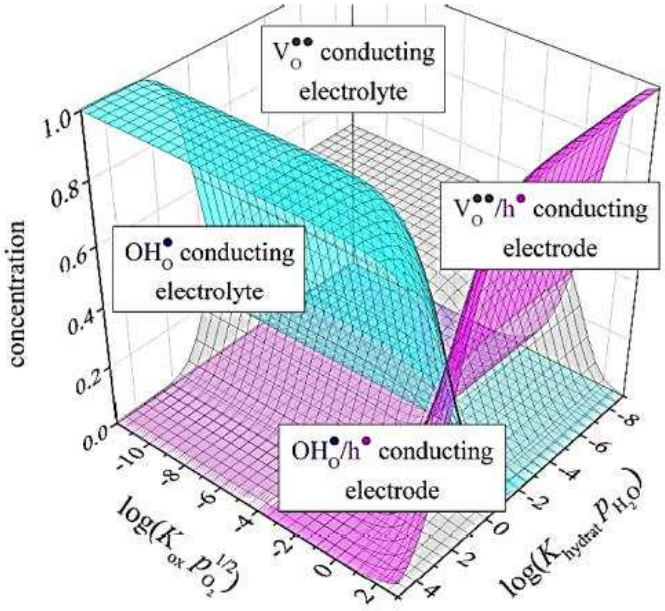


**Figure 5** Material map. Concentrations of protons (blue), holes (pink) and oxygen vacancies (black) as a function of $\log(K_{ox}\sqrt{pO_2})$ and $\log(K_{hydr}pH_2O)$. Taken from ref. [28].

### 1.2.1 Proton uptake and protonic transport

Protons are not native in the lattice of most oxides. One way to incorporate protons in the material is the hydration reaction (**Eq. 2**) at the expense of oxygen vacancies. The

hydration reaction comprises the protonation of a regular oxygen ion, and a hydroxide ion filling an oxygen vacancy. Both yield a protonic defects $OH_o^{\bullet}$, therefore, for one water molecule two protonic defects $OH_o^{\bullet}$ are formed. This is depicted in **Figure 6**.

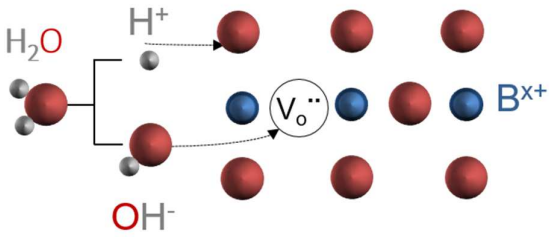


**Figure 6** Dissociative incorporation of water generating protonic defects, according **Eq. 2**.

The proton transport mechanism in perovskite was investigated by experiments and Quantum Molecular Dynamics (QMD) simulation [29]. The proton transport involves transfer of a proton between oxide ions (a Grotthuss-related mechanism), as well as rotational motion of the hydroxyl unit. The theoretical calculations and experiments both confirm that the rate-limiting step is the proton-transfer between oxide ions. This transfer is assisted by lattice phonons, which make approach the two oxygen to a distance that is suitable for hydrogen bonding and proton transfer. The rotational motion is fast, with a lower barrier. A visual representation of this process is shown in **Figure 7**.

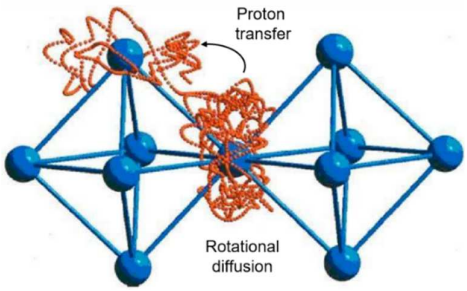


**Figure 7** Proton transport in perovskite from ref. [29]. Protons diffuse in the perovskite via a two steps process: (i) fast rotational diffusion and (ii) transfer to neighbouring O (blue spheres). The red spheres indicate the trajectory of a simple proton.

#### 1.2.1.1 Differences in the hydration behaviour of cathode and electrolyte materials

The hydration thermodynamics of cathode and electrolyte materials differs and the reasons are not trivial and still under investigation. In humid gas, acceptor-doped $Ba(Ce,Zr)O_3$ electrolytes get fully hydrated. In contrast, cathode materials become hydrated only to small degree. In fact, at temperatures below 400 °C less than 10% of oxygen vacancies accommodates protonic defect in the latter. The degree of hydration can be quantified using **Eq. 6**.

**Eq. 6**
$$\alpha = \frac{[OH_o^{\bullet}]}{2\,[V_o^{\bullet\bullet}]_{max}}$$

**Figure 8** reports the proton concentrations and degree of hydration for a typical $Ba(Zr,Y)O_{3-z}$ electrolyte and a cathode material $(Ba,La)(Fe,Zn)O_{3-\delta}$.

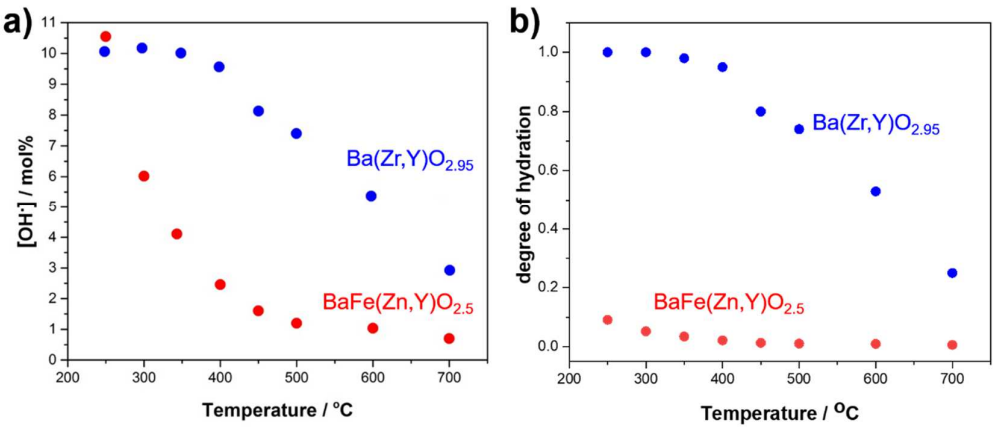


**Figure 8** Proton concentration (a) and degree of hydration (b) as a function of temperature of $Ba(Zr,Y)O_{3-z}$ and $(Ba,La)(Fe,Zn)O_{3-\delta}$. Data are taken from refs.[1,24].

The values of the degree of hydration show a difference of an order of magnitude between the cathode and the electrolyte material, even if the proton concentration at 250 °C is, within the error bar, the same. Thus, although cathode materials usually have a larger oxygen vacancy concentration than electrolytes, only a small fraction of the vacancies can be hydrated.

Other interesting considerations arise from **Figure 9**, which shows the standard entropy $\Delta S^o_{hydr}$ and enthalpy $\Delta H^o_{hydr}$ of hydration for a series of compositions ranging from typical cathode materials ($SrFeO_{3-\delta}$ or $BaFeO_{3-\delta}$ based) to electrolytes.

Cathode materials show less negative enthalpy values, and more negative hydration entropies compared to the electrolytes (only $Ba(Ce,Y)O_{3-\delta}$ shows more negative entropies than the cathodes, which can be ascribed to the orthorhombic structure creating energetically inequivalent oxygen sites for the protonation [30]). So far, there is no systematic explanation for this behaviour in literature; it is probably related to various effects including local lattice distortions, and modified electronic structure.

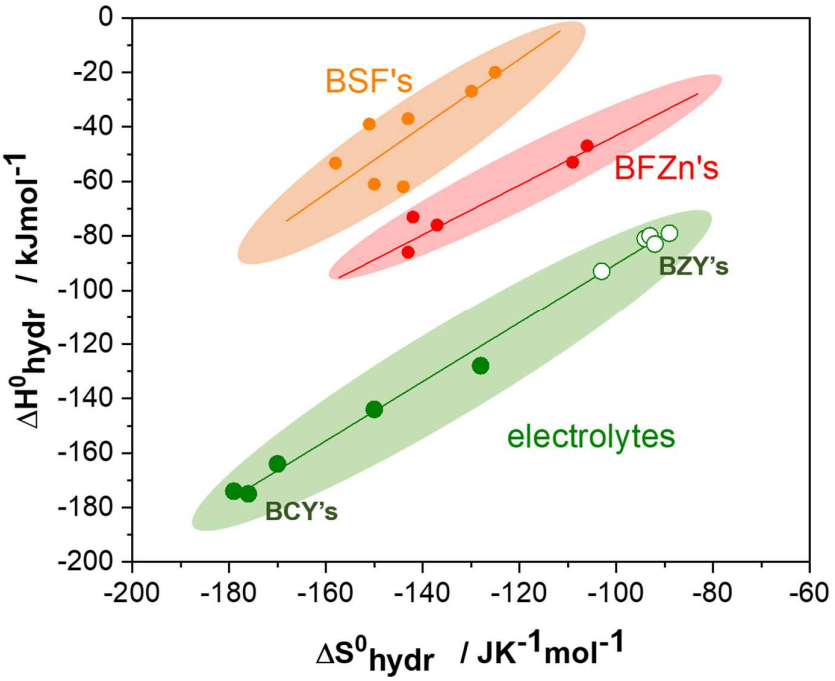


**Figure 9** Plot of $\Delta H^o_{hydr}$ vs $\Delta S^o_{hydr}$ of various composition with stoichiometries $SrFeO_{3-\delta}$, $(Ba,Sr)FeO_{3-\delta}$ (BSF), $Ba(Fe,Y,Zn)O_{3-\delta}$ (BFZn), $Ba(Zr,Y)O_{3-z}$ (BZY), $Ba(Ce,Y)O_{3-\delta}$ (BCY). Data from refs.[1, 24].

Regarding the energy (enthalpy) of hydration, DFT calculations of proton and hydroxide affinity for a large range of oxides showed that materials with a smaller ionization potential and correspondingly larger proton affinity have more negative hydration enthalpies [31]. This relation may appear surprising at first glance because the hydration reaction (**Eq. 2**) has an amphoteric character (protonation of an oxide ion and incorporation of hydroxide into $V_O^{\bullet\bullet}$).

But the DFT calculations in ref. [31] show that the proton affinity is the parameter with a stronger variation from material to material, and outweighs the opposite trend of the

hydroxide affinity. Thus the hydration enthalpy correlates with the proton affinity, which can be regarded as a measure of the basicity in the considered oxides. This corresponds to the phenomenological observation that often oxides with higher basicities have more negative $\Delta H^{o}_{hydr}$.

## 1.3 Materials included in the present thesis

The materials investigated in the present work can be divided in three groups:

(i) $BaFeO_{3-\delta}$ doped with oversized redox-inactive dopants such as Zn and Y. This composition was chosen to clarify the interplay of iron formal oxidation state, oversized dopants and local B-site environment, Fe-O covalency, and charge (de)localization on proton uptake. The fundamental questions related to this composition started with the work of Dr. Daniel Poetzsch [32] and Dr. Reihaneh Zohourian [24]. This group of materials will be discussed in **Section 3.1**.

(ii) $BaZr_{0.88-x}Fe_xY_{0.12}O_{3-\delta}$ solid solution, which ranges from electrolyte-type material for low Fe content to triple conducting cathode material for large x. These materials show interesting protonation behaviour as a function of the iron content. They are particularly suitable for impedance measurements coupled with an oxygen pump, to derive the Brouwer diagrams. The electronic behaviour is of interest with respect to impurity band formation and appearance of $FeO_6$ percolation paths. Changes in the local environment of the B-site and in the oxygen electronic states help to understand the trends regarding proton uptake. The solid solution $BaZr_{0.88-x}Fe_xY_{0.12}O_{3-\delta}$ will be discussed in **Section 3.2**.

(iii) $Ba_{0.95}La_{0.05}Fe_{0.8}TM_{0.2}O_{3-\delta}$ with TM=Fe, Co, Cu and Ni. Since $Ba_{0.95}La_{0.05}FeO_{3-\delta}$ has a comparably low electronic conductivity, doping with 20% of other first-row redox-active transition metals is of interest. The effects of the TMs on proton uptake, electronic conductivity and oxygen non-stoichiometry are systematically discussed in **Section 3.3**.

The overall goal of this thesis is to obtain an improved understanding of the materials parameters that are decisive for proton uptake in triple conducting perovskites, and to identify strategies for optimizing them as PCFC cathode materials.

# 2 Materials and Methods

## 2.1 Sample preparation

### 2.1.1 Nomenclature and abbreviations

In the present thesis, $BaFeO_{3-\delta}$ and related perovskites are denominated as "barium ferrates". Frequently, the ending "-ate" refers to the highest oxidation state of the respective element. For $BaFeO_{3-\delta}$ the situation is complex: the highest Fe oxidation state in oxides is 6+ in compounds such as $K_2FeO_4$ or $BaFeO_4$ [33]. The oxidation state of iron in $BaFeO_{3-\delta}$ ranges between +3 and +4. Traditionally, the term "barium ferrite" is often associated with the compound $BaFe_{12}O_{19}$. In terms of IUPAC nomenclature, $BaFeO_{3-\delta}$ should be referred as "barium iron(III,IV) oxide (*perovskite* type)" which is inconveniently cumbersome. Thus, the term barium ferrate is preferred here, in agreement with literature [34].

This thesis uses a popular abbreviation scheme for the different samples. The abbreviations essentially follow two rules: (i) the elements are indicated by their symbols except for the most commonly used such as Ba, La, Sr, Fe which will be written here as B, L, S, F respectively. (ii) The A and/or B-site dopant is followed by its stoichiometric coefficient. According to this, BL5FZn20 is referring to $BaLa_{0.05}Fe_{0.8}Zn_{0.2}O_{3-\delta}$; BSFZn20 to $Ba_{0.5}Sr_{0.5}Fe_{0.8}Zn_{0.2}O_{3-\delta}$. In the latter case the stoichiometric coefficient of barium and strontium are not reported since they are both occupying the A-site in equal amounts. For samples treated in reducing or oxidizing conditions the endings *red* or *ox* are added.

### 2.1.2 Synthetic routes

Two synthetic routes were used for powder preparation depending on the desired composition: mixed oxides synthesis or wet synthesis.

*Mixed oxides synthesis* was used for preparing powders of Zr-rich samples and SF (first order perovskite or Ruddlesden-Popper). In this approach, the oxides (or carbonates) of the metal precursors were weighted in stoichiometric amount, mixed in a zirconia jar and dry ball milled for 1 hour. The powders were then calcined 3 times at 1100 °C for 8 hours in alumina crucibles, and dry ball milled 1 hour at the end of each calcination.

*Wet synthesis* was used for preparing the rest of the compositions. In this case the nitrates of the metals were stoichiometrically weighted and dissolved in bi-distilled water with citric acid and EDTA following the stoichiometric ratio 1(metals):1(citric

acid):1.5(EDTA). The pH was adjusted to approximately 9 with aqueous ammonia solution. The solution was slowly heated under stirring until an amorphous gel was formed. The temperature was then increased to 500 °C and the gel thermally decomposed. The as-prepared powders were dry ball milled and then calcined in alumina crucibles at 1000 °C for 8 hours in order to allow the perovskite phase formation and the complete decomposition of the remaining organic matrix. The powders are then dry ball milled for 0.5 hour.

In both synthetic routes, the weighting process is one (or the most) crucial step, therefore it is necessary to use high purity reagents (≥99.5%). In the case of nitrates which are usually hydrated the amount of water needs to be well defined (*e.g.,* measured by TGA) to obtain the correct composition. The crystal phase and the stoichiometry of the calcined powders were then checked with XRD and ICP-OES.

### 2.1.3 Pellet preparation

The calcined powders were densified to pellets. Depending on the application two different sintering techniques were used: conventional sintering or Spark Plasma Sintering (SPS).

*Conventional sintering.* About 2 g of calcined powder were compacted inside a rubber mold (∅ 11 mm) and isostatically pressed applying 20 kN of pressure for 1-2 minutes. The resulting pellets were then sintered in air at suitable temperature in the range 1100 °C - 1550 °C in the appropriate crucible material (alumina or magnesia).

With this method, the pellets had usually a density above 92%. A full list of the sintering condition and lattice parameters is included in **Section 2.3**.

*Spark plasma sintering* is a technique which applies uniaxial pressure at a temperature where the plastic deformation becomes possible. Fast heating rates (1000 $Kmin^{-1}$) and short holding times (1-5 min) are combined by flowing electrical current through a graphite die and the conducting sample. This yields densification above 95% [35] even for materials which are difficult to sinter otherwise. Owing to the short time, grain growth hardly occurs. This technique was mainly used for preparing barium ferrate based material in order to achieve very dense (pore free, crack free) pellets. Excessive sample reduction by the graphite die can be prevented by protecting the sample with YSZ felt and/or gold foil. The SPS pellets were then annealed in a tube furnace in $N_2$ at 750 - 1020 °C for 8 hours. A list of the SPS conditions used in the present work are enclosed in **Table 1**.

**Table 1** SPS sintering conditions used for preparing the pellets included in this thesis. The pressure applied is 10 kN for all the samples

| **Sample/** ***sealing*** | **Heating rate K/min** | **Holding time /min** | **Cooling rate K/min** |
|---|---|---|---|
| BL5FZn20/ *YSZ felt-gold foil* | 100 (RT→650 °C)<br>50 (650 °C→750 °C) | 750 °C x 30 min | 30 (750°C→400°C)<br>100 (400°C→RT) |
| BL5F/ *YSZ felt* | 150 (RT→800 °C)<br>100 (800 °C→900 °C) | 900 °C x 30 min | 30 (750°C→400°C)<br>100 (400°C→RT) |
| BFY20/ *YSZ felt* | 150 (RT→900 °C)<br>50 (900 °C→1020 °C) | 1020 °C x 30 min | 30 (750°C→400°C)<br>100 (400°C→RT) |

### 2.1.4 Particle preparation for TG experiments

After grinding off the outer layer of the sintered pellets using silicon carbide polishing paper, they were crushed using a press and a mortar and then sieved. The desired particles size for water uptake TG experiments is 250-100 µm because it prevents water adsorption errors and still allows for reasonable equilibration time with the $pH_2O$ [32]. For oxygen stoichiometry experiments the desired particles size is <100 µm, because the oxygen incorporation surface reaction is more sluggish than the hydration.

### 2.1.5 Powder reduction and oxidation treatments

For some measurements (*e.g.,* EXAFS, XRS and UV-Vis) samples with fixed iron formal oxidation state (and thus oxygen stoichiometry) were prepared. The phase pure powders from the calcination or from crushing pellets after sintering were heated either in reducing environment (→ Fe mainly in 3+ formal oxidation state) or under oxidizing conditions (→ Fe mainly 4+). The success of the treatment is already visible by the colour of the powders that turn brownish after the reduction and black after oxidation (**Figure 10**). The exact stoichiometry of oxidized samples was checked with TGA either by heating to 900 °C in $N_2$ or to 700 °C in 1.5% $H_2$, in both cases a plateau corresponding to the iron being 3+ it could be observed. The choice of the two treatments condition is based on previous experiments within the department (see *e.g.,* [36-37]).

*Reducing treatment.* The reduction of samples was carried out in the TG furnace with 1.5% of $H_2$ at 700°C for 4−5 hours.

*Oxidation treatment.* The oxidation was carried out in an autoclave at 600 bar of pure $O_2$ from 550°C, decreasing to 250°C during 72 h. All oxidized samples reached at least 96% of their nominal oxygen stoichiometry.

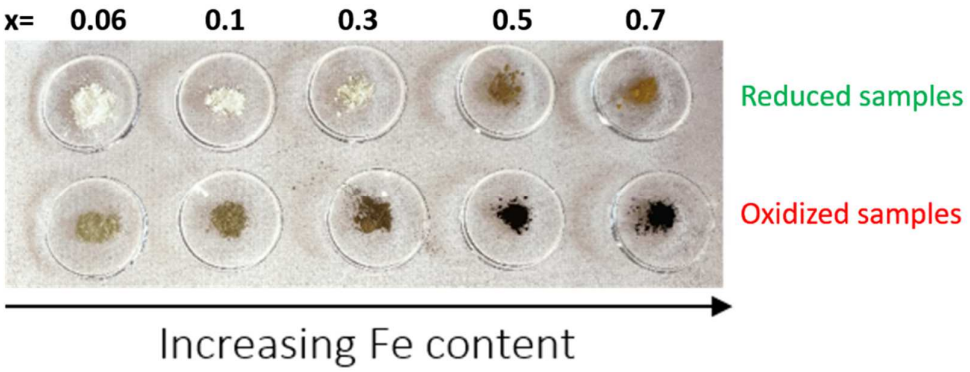


**Figure 10** Reduced and oxidized powders of $BZYF_x$ with ($0.06<x<0.7$). Note that the colour also changes accordingly to the amount of iron.

### 2.1.6 Samples preparation for XAS and XRS

For the XRS measurements, 0.5 g of powder was uniaxially pressed in a die of ∅ 13 mm with about 10 kN for 5 minutes. Alternatively, borosilicate capillaries were filled with the powders, densified with the help of an ultrasonic bath and sealed. More preparation is required for XAS samples. For transmission measurements the amount of powders, required to have an edge jump for the desired element >0.1 absorption length, was calculated using the software XAFSmass [38]. For fluorescence measurements, the amount of powders was calculated in order to have $10^{19-18}$ atoms of the desired element per $cm^2$. The resulting amount is weighted and pre-mixed in a mortar with the minimum amount of cellulose (Cellulose nanocristalline- Sigma Aldrich) to obtain a self-standing pellet (ca. 100 mg in total). The mixture is homogeneously milled in small volume ball miller (Pulverisette 23, Fritsch, Germany) for about 10-15 minutes and pressed into pellets using the uniaxial press with 3kN (∅ 5mm pellets) or 10 kN (∅ 13 mm pellets) for 5 minutes.

## 2.2 Characterization Techniques

### 2.2.1 X-Ray Diffraction

X-ray diffractograms were measured at room temperature in Bragg-Brentano reflection geometry by a PANalytical diffractometer Empyrean Series 2 using Cu $K_\alpha$ radiation ($\lambda$ = 1.54184 Å, 40 kV, 40 mA) and a PIXcel 3D detector in the range of $2\vartheta = 10^\circ - 90^\circ$ with $0.013^\circ$ step size. The data refinement was performed with PANalytical software HighScore Plus (Version 3.0e). The measurements were carried out by Dr. Helga Hoier.

### 2.2.2 Inductively Coupled Plasma Optical Emission Spectroscopy

The cation stoichiometry of the powders was analytically determined using ICP-OES (Spectro Ciros CCD, Spectro Analytical Instruments, Germany) in the chemistry laboratory of Max Planck Institute for Intelligence System, Stuttgart, by Samir Hammoud. For the analysis, the samples were dissolved with a microwave autoclave in a solution of $HCl/HNO_3$ (or HF in the case of zirconates).

### 2.2.3 Thermogravimetric analysis coupled with mass spectroscopy

Proton uptake and oxygen stoichiometry measurements are performed using a thermogravimetric analyzer (STA 449 C Jupiter, Netzsch, Germany). This can operate in isothermal or dynamic modes from RT to 1650 °C with heating/cooling rates of 0.01-50 $Kmin^{-1}$. The setup is gas tight, so different gases and gas mixtures can be flown over the sample. A dry inert gas (protective gas) is always flowing (flow=10 $mLmin^{-1}$) through the balance compartment. The exhaust is monitored with a quadrupole mass spectrometer (QMS 200 F1, Balzers Prisma, Germany) which can detect masses in the range 1-100 amu.

Thermogravimetry was typically carried out with 2 g of sample (particle size 100-250 µm) inside an alumina crucible and total gas flow was 60 $mLmin^{-1}$ (50 $mLmin^{-1}$ of desired gas + 10 $mLmin^{-1}$ of protective gas) adjusted using gas flow controllers. A sketch of the setup is depicted in **Figure 12**.

*Proton uptake (isothermal) measurements.* For proton uptake measurements the two gas conditions used are dry (dry $N_2$) and wet (humid $N_2$). The nitrogen steam is humidified by bubbling the gas through a water evaporator connected to a thermostat running at 5, 12 and 18 °C. During the experiment the sample is typically equilibrated with five $pH_2O$ (1.45, 2.9, 7.3, 11.7 and 16.7 mbar) at a fixed temperature. Before starting the isothermal changes the sample is quenched from high temperature (700 °C for 30 min) in dry nitrogen in order to maximize $[V_O^{\bullet\bullet}]$ (all iron as $Fe^{3+}$) and then to freeze the

oxygenation reaction (**Eq. 1**). In this condition just the hydration reaction (**Eq. 2**) is active, which is kinetically easier than the oxygen incorporation. After the sample is equilibrated in dry $N_2$ at a certain temperature, the $pH_2O$ is increased stepwise. The new equilibrium is reached in ≈30-50 min for each $pH_2O$. The reproducibility of the experiment is checked by stepwise decreasing the $pH_2O$ back to dry condition. This procedure is then repeated for different temperatures, usually from 250°C to 700 °C in 50-100 °C steps. An exemplary TGA thermogram is reported in **Figure 11**.

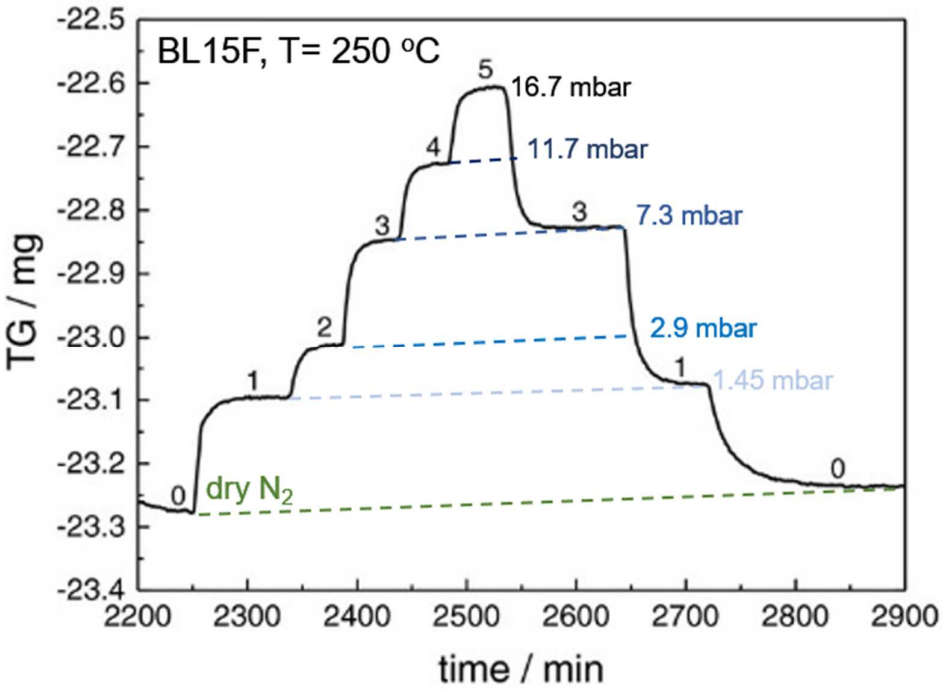


**Figure 11** Exemplary TGA thermogram of BL15F for an isothermal hydration experiment. The values reported in mbar refer to the $pH_2O$. Adapted from ref. [24].

The mass change for each step is proportional to the amount of water the material incorporates, and from the proton concentration at different temperatures it is possible to extract thermodynamic quantities ($\Delta H_{hydr}^{o}$, $\Delta S_{hydr}^{o}$) from a van't Hoff plot of $K_{hydr}$.

*Oxygen stoichiometry (dynamic) measurements.* About 500 mg of sample (particles <100 µm) were measured in dry oxidizing conditions (0.085%, 2.5%, 83.3% $O_2$) while the temperature was decreased, with cooling rates of 0.2 to 2 K/min, from 900 °C to 300 °C. For some samples, reversibility was checked by recording the heating from 300 °C to 900 °C. The absolute oxygen stoichiometry was determined by reducing the sample at 700 °C in 10% $H_2$ (different hydrogen percentages and temperatures for the sample included

in **Section 3.3**). Under these conditions a plateau corresponding to the iron being 3+ appears in the TGA curve, and the oxygen stoichiometry matches the calculated value using the electroneutrality condition. From this mass difference it is then possible to calculate the exact oxygen content for each condition, and also extract thermodynamic information such as $K_{ox}$.

A buoyancy correction is not necessary in the case of the isothermal measurements. For the dynamic measurements, the buoyancy changes were measured with a crucible filled with an appropriate amount of inert alumina ceramics and then subtracted from the sample weight changes.

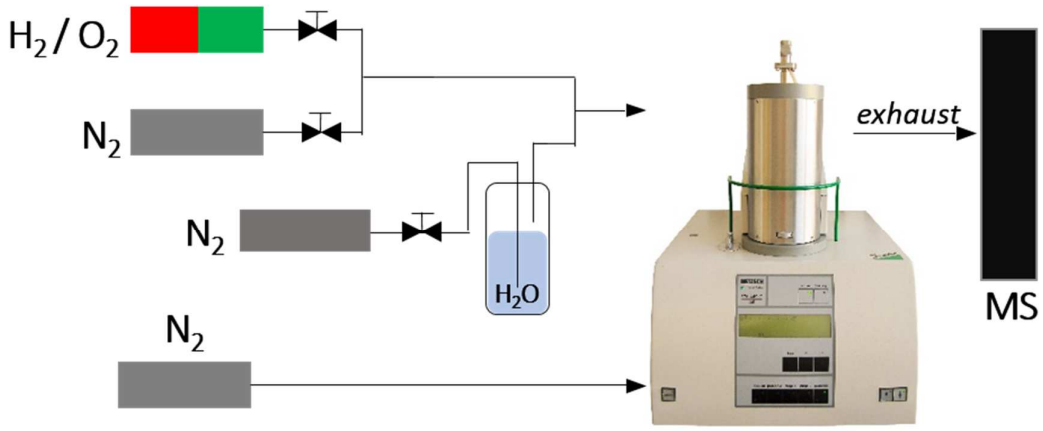


**Figure 12** Sketch of the TG setup: gas mixing system (upper left), protective gas (bottom left), TG analyzer and MS.

### 2.2.4 X-Ray Absorption Spectroscopy

In a XAS experiment a sample is irradiated with X-rays of a defined energy. In this regime, light is absorbed by matter through the photoelectric effect. Once the X-rays are absorbed by the sample, if the binding energy of a core level is less than the energy of the incident light, this causes the excitation or ejection of a core-electron. In **Figure 13** the XAS at the Fe *K*-edge of a measured sample (SFZn2ox) is shown.

When discussing XAS the relevant quantity is the absorption coefficient, which gives the probability of the absorption event according to Beer's Law (**Eq. 7**).

**Eq. 7** $$I = I_0 \, e^{-\mu t}$$

In this equation $I$ and $I_0$ are the incident and transmitted radiation intensities, $\mu$ is the absorption coefficient which characterizes the probability of the absorption event to occur. The absorption is recorded for a given energy; the energy is changed slightly step-by-step to obtain the full spectrum.

In the spectrum in **Figure 13** one can recognize some features: (**a**) the sharp rise in absorption (absorption edge) which occurs when a core electron is promoted to the continuum (this physical process is depicted in **subfigure(a**). (**b,c**) after the edge a gradual oscillation up and down with an amplitude which decreases increasing the energy, which is called EXAFS. The region 50 eV before and after the edge is called XANES (X-ray Absorption Near Edge Structure). The XANES region contains information on the unoccupied electronic states, spin state and ligand field. It is a useful tool for determining oxidation states by simulation, or by comparing the edge (and/or pre-edge) shifts with a standard of a known valence.

The process causing the modulated oscillation (EXAFS) is illustrated in **subfigures(b,c)**. The photoelectron ejected from the atom corresponds to a wave radiating in all directions. This wave can scatter elastically at nearby atoms interfering constructively or destructively when returning to the absorber. This is called scattering path, which in first approximation is the bond length.

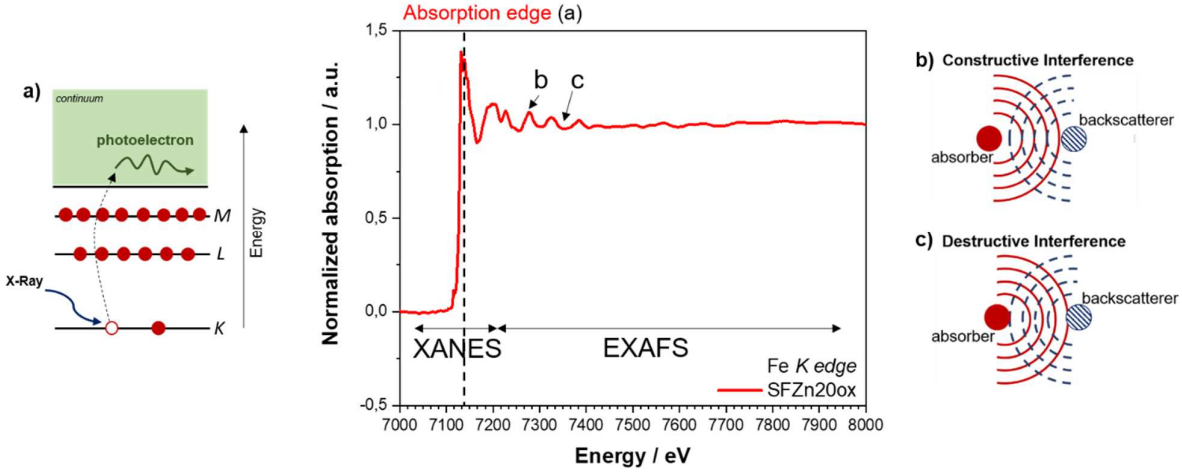


**Figure 13** Exemplary plot showing the normalized absorption (Fe *K*-edge) of SFZn20ox where the XANES and EXAFS regions are highlighted. Inset a) shows the absorption process b-c) the constructive/destructive interference of waves from which the EXAFS modulation originates.

The interference pattern of the electron wave has an absorption probability modulated by a factor $\chi$. By taking into account other events (*e.g.,* inelastic scattering, non-collinear multiple scattering), the presence of different neighbors, thermal and static disorder and geometric factors, we obtain **Eq. 8**, the EXAFS master equation [39]. The figures in bold are fitting parameters which can be free or constrained according to the applied structural model.

**Eq. 8**

$$\chi(k) = S_0^2 \sum_i \boldsymbol{N_i} \frac{f_i(k)}{k\boldsymbol{R_i}2} e^{\frac{-2\boldsymbol{R_i}}{\lambda(k)}} e^{-2k^2\boldsymbol{\sigma_i^2}} \sin(2k\boldsymbol{R_i} + \varphi i(k))$$

In **Eq. 8**, $k$ is the wave vector modulus of the photoelectron, $S_0^2$ is an amplitude reduction factor, $N_i$ is the number of atoms of type i at distance $R$ from the absorber (the coordination number), $^{-2R_i}/_{\lambda(k)}$ accounts for the finite elastic mean free path of the photoelectron, $\sigma_i^2$ is a factor which contains information about the disorder (thermal and static), $f_i(k)$ is a scattering amplitude function characteristic of the i$^{th}$ atom, $\varphi i(k)$ is a phase function that takes into account the varying potential field along which the photoelectron moves.

When fitting the $R$ parameter, two possible scattering events have to be considered which create two types of scattering paths (**Figure 14**): Single Scattering Path (SP, **a**) and Multiple Scattering Paths (MSP, **b**).

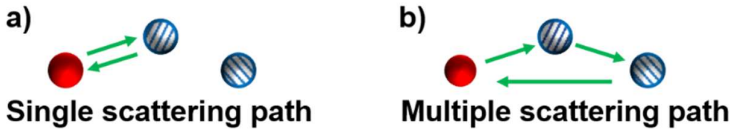


**Figure 14** Sketch depicting single (a) and multiple (b) scattering paths examples.

EXAFS contains information about the interatomic distances, disorder levels and coordination numbers. Extracting these quantities is possible owing to the fact that the signal can be Fourier transformed (from $k$-space to $R$-space) allowing us then to fit the desired parameters using a user-defined model. An example is reported in **Figure 15** showing the Fourier transform and the corresponding signal of the different coordination shells for SFZn20ox at the Zn $K$-edge.

It is important to note that the peak positions of the modulus do not directly match the experimental atomic distances, but are modified by the phase function.

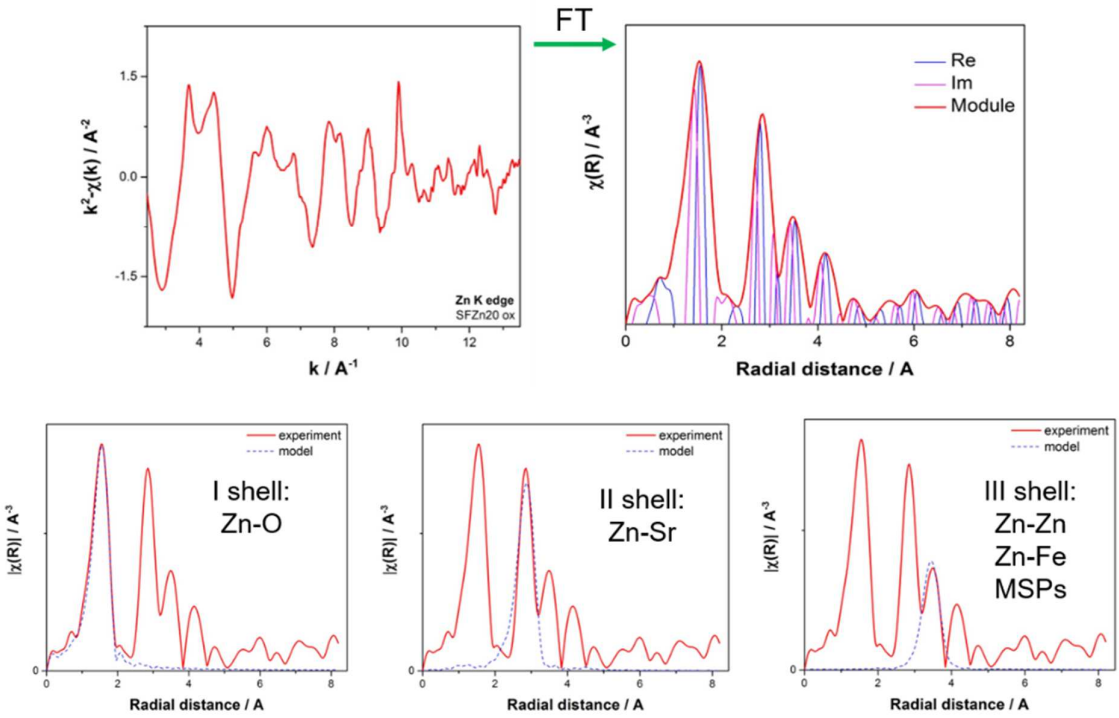


**Figure 15** (top) FT of the EXAFS signal of SFZn20ox at the Zn *K*-edge from *k* to *R*-space. (bottom) Exemplary fitting of I, II and III shells. In the III shell is necessary to take also the MSPs into account since their contribution is not negligible.

*Experimental details used in the present thesis.* The XAS measurements were collected at beamlines BM26 (for the samples included in **Section 3.1**) and BM23 (for the ones in **Section 3.2**) at ESRF (European Synchrotron Radiation Facility, Grenoble, France) in multi-bunch mode using a double-crystal monochromator equipped with Si(111) crystals with the sample holder in a cryostat at 80 K (or 10 K). The data were collected at the energies of Fe *K*-edge (7.1 keV), Zn *K*-edge (9.7 keV), Y *K*-edge (17.0 keV) and Zr *K*-edge (17.9 keV) depending on the elemental composition of the sample. Most of the measurements were done in transmission mode; exceptions were the samples BZYF06 and BZYF10 for which the Fe *K*-edge was measured in fluorescence.

For the extraction of the $k^2$-weighted data a Bayesian algorithm in the software Athena was used, the fitting was performed using the software VIPER [40]. The scattering amplitudes and phases used were calculated with the FEFF9.1 code [41] employing the complex exchange-correlation Hedin-Lundqvist potential. The calculations were performed for a cluster with a radius of 8 Å of which the coordinate file is created by changing the central atom using WEBATOMS [42] starting from the Crystallographic

Information File (CIF) of a cubic parent perovskite (such as SF or BF for the compositions in **Section 3.1**). Calculations of the cluster potentials were done in the muffin-tin self-consistent field approximation using the default parameter of the FEFF code. The normalized data were fitted in real space with an $r^2$ minimization algorithm. The model used for the fitting is based on a cubic perovskite structure. The following geometrical and physical constraints derived from previous knowledge of the samples (*e.g.,* XRD structure, oxygen stoichiometry) were applied: (i) defined number of neighbours accounting for the oxygen deficiency, (ii) random distribution of oxygen vacancies since no superstructure by vacancy ordering was found in XRD, (iii) equal constraints on $E^0$ for the same atomic pairs in the case of MSPs, (iv) defined ranges for the disorder (by qualitatively comparing the FTs of various set of samples), defined ranges for the distances according to the geometry of the structure.

### 2.2.5 X-Ray Raman Scattering

In XRS (also referred to as Nonresonant Inelastic X-ray Raman Scattering), an X-ray photon with energy $\omega_1$ interacts with an electron of the sample and is scattered inelastically, emerging with a reduced energy $\omega_2$. The energy $\omega = \omega_1-\omega_2$ and the momentum $q = k_1-k_2$ are transferred to the sample. $k_1$ and $k_2$ are the momenta of the incident and scattered photons, respectively, with a scattering angle $2\Theta$ (see sketch in **Figure 16**). In XRS, the energy loss $\omega$ is tuned in the vicinity of soft X-ray absorption edges by varying $\omega_1$, while observing the intensity of photons that emerge from the sample with a fixed $\omega_2$ into the finite solid angle element $\Theta$. Most commonly, both incoming and scattered photon energies are of the order of 10 keV (hard X-rays). The fact that hard X-rays are employed gives the advantage of studying light elements (such as oxygen) by a bulk sensitive technique. This yields similar information as XAS. However, employing soft X-rays for XAS of light elements would lead to low penetration depths (large surface effects) which are not desired here where the bulk properties are under investigation.

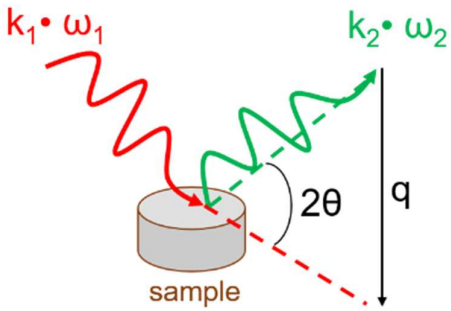


**Figure 16** Sketch of the scattering geometry for XRS. $k_1$ and $k_2$ are the momenta of the incident and scattered photons, respectively, and $\omega$ corresponds to their energy.

*Experimental details used in the present thesis.* XRS at the O *K*-edge was performed at ID20 at ESRF, measuring the samples in **Sections 3.1** and **3.2**. The beam was monochromatized using a double-crystal Si(111) monochromator and focussed to a spot size of ≈ 10 x 20 µm² with Kirkpatrick-Baez mirrors. The large solid angle spectrometer (see **Figure 17**) was used to collect data with 36 spherically bent Si(660) analyzer crystals.

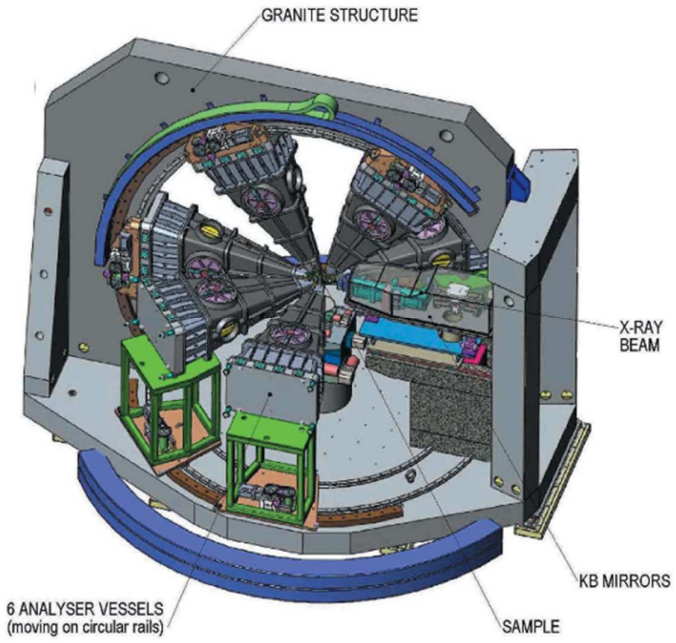


**Figure 17** Schematic view of the spectrometer at ID20 for XRS experiments. Image taken from [43].

The overall energy resolution was 1 eV. To extract the O *K*-edge spectra from broader scans (0-900 eV) the XRStools package [44] was used to merge data at medium and high momentum transfer (6.2 ± 0.4 $Å^{-1}$). O *K*-edge spectra (520-590 eV) were collected with 0.2-0.7 eV energy step at room temperature, until the signal-to-noise ratio was good and comparable data quality for all samples achieved. To elucidate the electronic structure of the materials, O *K*-edge ab initio simulations were performed using the Finite Difference Method Near Edge Structure (FDMNES) software package [45,46]. These simulations were performed by Dr. Alessandro Longo (ESRF). The atomic positions were generated from a cubic *Pm-3m* space group using the experimental lattice constants. The simulations have been performed by using the multiple scattering theory based on the muffin-tin (MT) approximation using non-relativistic calculations and the Hedin-Lundqvist exchange potential. The MT radii were tuned to have a good overlap between the different spherical potentials. The approximation of non-excited scatterers was used. Finally an arc-tangent convolution to account for the core-hole lifetime and photoelectron state width is performed, followed by a Gaussian convolution accounting for the experimental resolution. The obtained spectra are then normalized to the same integrated intensity of the experimental data in the suitable energy loss range. In order to extract the structural and electronic information, the calculations are compared with the experimental signals. In the simulation, two semi-empirical parameters are used: *screening* and *dilatorb*. The *dilatorb* parameter is the expansion coefficient applied to the valence atomic orbital (changing its radial extension). Accordingly, *dilatorb* = 0.1 expands the respective orbital by 10%. A higher *dilatorb* value is equivalent to higher covalency because of more effective overlap of the absorber and first neighbour orbitals. It also addresses the actual charge of the oxygen species. In fact, this parameter, which in principle can be defined for all the ionic species in the material, has been applied mainly to simulate the oxide ion $O^{2-}$ whose atomic basis is generally taken from the neutral atom. The *screening* parameter modifies the electronic charge in a partially occupied valence orbital of the absorber, placing additional electron density in the first non-occupied state, while keeping the absorbing atom (relatively) neutral. In a self-consistent calculation, the neighbouring atoms can participate in the core-hole screening by increasing or decreasing the extent of the electron transfer. Hence, this parameter, applied to the scatterer, helps to simulate its interaction with its neighbours. In the case of the O *K*-edge, *screening* describes the interaction of oxygen and the transition metal (TM). When a photoelectron is completely promoted to unoccupied states and the core

hole not further stabilized, it formally corresponds to a *screening* value of 0. Physically, the core hole can be better screened when the scatterer atom has a higher electron density. In FDMNES this can be reproduced by increasing the *screening* parameter up to 1 (which corresponds to adding one electron in the lowest non-occupied state). Hence, *screening* = 0.6 means that an electron density that corresponds to 0.6 fraction of electron charge, is added to the lowest empty state. Intuitively, a higher *screening* value applied on the oxygen atoms corresponds to a more negative charge on oxygen, and a lower interaction and electron transfer to the transition metal ion. The effect of *screening* and *dilatorb* parameters on the simulation is illustrated for an exemplary sample (BL5Fox) in **Figure 18**. This procedure can also be used for simulating the XANES (from XAS) of other elements, in the present thesis it was also applied to Zn and Y *K*-edges. [47]

It is worth mentioning, that the use of the two semi-empirical parameters does not suffice when important structural organization (*i.e.,* very disordered local environments) is present. In this case, it is more efficient to simulate the experimental XANES using a weighted sum of two (or more) structural configurations with different coordination environments of the scatterer (or absorber). More details are provided in **Section 3.1.3**.

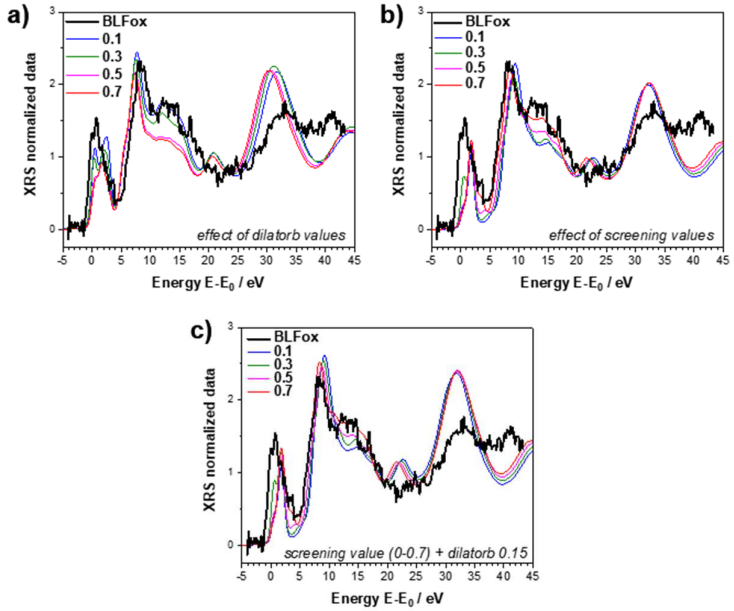


**Figure 18** O *K*-edge of BL5Fox. Effects of different values of *dilatorb* (a) and *screening* (b) on the simulations. (c) Effect of *screening* values matched with the best *dilatorb* value of 0.15. The simulated spectra with the semi-empirical parameters are not convoluted.

### 2.2.6 UV-Vis Diffuse Reflectance Measurements

Diffuse reflectance UV–Vis spectra were collected, for the compositions in **Section 3.2**, with a Cary 5000 (Agilent Technologies, USA) spectrometer. The samples were diluted in the molar ration 1:4 with $ZrO_2$ (which has no absorption in the relevant range), and the spectra were acquired in the 200-800 nm range with 1 nm step.

### 2.2.7 Electrochemical Impedance Spectroscopy

An Alpha-A high resolution impedance analyzer (Novocontrol, Germany) was used to record the impedance spectra of samples in the frequency range of typically $10^6$-$10^{-2}$ Hz with 0.02 V amplitude.

*Conductivity measurements of* $Ba_{0.95}La_{0.05}Fe_{0.8}TM_{0.2}O_{3-\delta}$. Electrochemical impedance spectroscopy was performed for a series of barium ferrate undoped or doped on the B-site with 20% of a transition metal (Mn, Ni, Cu, Co, Zn). The measurements were done on bars cut from sintered dense pellets (by the Crystal Preparation, Max Planck Institute, Stuttgart). The contact (Ag-paste) was applied on the short edges together with Pt wires (see **Figure 19**) and mechanically fixed to the measurement cell wires. Samples were equilibrated in different $pO_2$ (100%, 10%, 1%, 1000 ppm) and different temperature (range: 250-700°C).

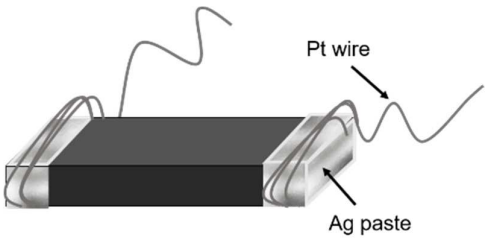


**Figure 19** EIS sample geometry and contact arrangement. The Ag paste was also applied on top of the Pt wires for a better contact.

In this condition the predominant charge carriers are electron holes, therefore the conductivity extracted from the data is purely the p-type electronic conductivity ($\sigma_{eon}$) and the impedance signal can be fitted using a single resistance in the equivalent circuit. For samples with low resistance, the separately measured Pt-wire resistance in the range of 2 Ω was subtracted. No signs of blocking grain boundaries were visible.

*Conductivity measurements of* $BaZr_{0.88-x}Fe_xY_{0.12}O_{3-\delta}$. Impedance measurements were performed on slices cut from dense pellets sputtered with ≈400 nm Pt (EdwardAuto 306, UK), they were mounted between two Pt-foils and kept in place by spring force.

The compositions with x=0.01, 0.03, 0.06, 0.1, 0.2, 0.3, 0.5, 0.7 were measured in the temperature range RT-700 °C and in three different gas atmospheres: equilibrated in wet $N_2$ ($pH_2O$=18 mbar), quenched in dry $N_2$, and quenched in dry 100% $O_2$, to elucidate the contributions for protons, oxygen vacancies and holes.

For low iron doping (x<0.1 the Impedance spectrum is composed of two semicircles corresponding to blocking grain boundaries and bulk as shown in **Figure 20**). It can be modeled by two R-CPE pairs connected in series. For higher iron content, the spectra showed just a semicircle, or part of it, at high frequency (bulk).

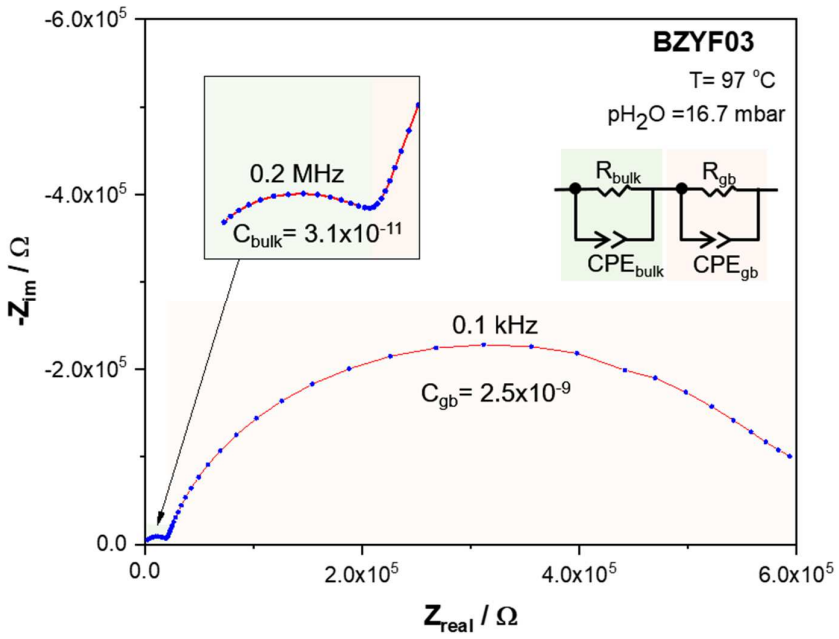


**Figure 20** Exemplary Nyquist plot of BZYF03 showing two semicircles assigned to bulk (high frequency) and grain boundaries (middle frequency). Inset: a magnification of the bulk semicircle, and a scheme of the equivalent circuit used for the fitting.

It is not trivial to separate the contribution of electronic carriers, proton and oxygen vacancies in these mixed conductors since $\sigma_{eon} >> \sigma_{ion}$ and, depending on the composition studied, even choosing the appropriate atmosphere is not enough to measure just one type of charge carrier. A direct measurement of protons, oxygen vacancies and holes can be done using an impedance cell coupled with an oxygen pump that allows better adjustment of $pO_2$ over a very wide range.

#### 2.2.7.1 Oxygen pump measurements

Using an impedance setup with an integrated oxygen pump offers the possibility of separating the individual carrier contributions of mixed conductors. In fact, it is possible to pump out oxygen under cathodic voltage up to a $pO_2$ of about $10^{-10}$ where the contribution of the holes becomes negligible or is even replaced by the *n*-type carriers' contribution at very low $pO_2$. This allows a direct measurement of the protonic conductivity, on which there are no data reported in literature so far for triple conducting oxides.

The cell setup with the integrated oxygen pump was built by Dr. Tobias Huber (Huber Scientific, Austria). The setup consists of two parts: pump and sample side. The pump side consists of: (i) a YSZ based oxygen pump connected to the voltage source (controlled by a EUROTHERM 3508, France) and to a multimeter for monitoring the current (Keithley Instrument, Mod. 2000, USA), (ii) a lambda sensor and (iii) a type S thermocouple. The sample side is composed of: (i) the EIS measurement cell, (ii) a lambda sensor and (iii) a type S thermocouple. The setup is inside a quartz tube, inserted in a homemade tubular oven with two heating zones. Zone A is kept at 700 °C (temperature controlled by a EUROTHERM 9028, France) which is the most convenient for the pump functioning whilst avoiding too much silica transport from the quartz. The temperature of zone B (controlled by a EUROTHERM 2416, France) is varied according to the experiment requirements. There is some cross heating, thus the lowest achievable temperature in zone B is ≈ 240 °C. The setup is schematised in **Figure 21.**

It is important to note that when the pump and sample temperature differ, also the effective $pO_2$ differs. A $pO_2$ is established in the pump at 700 °C which is determined by the $CO/CO_2$ or $H_2/H_2O$ ratios and the respective mass action constant. The $CO/CO_2$ and $H_2/H_2O$ concentrations are transferred unchanged to the sample which is at lower T. There, these concentrations lead to different $pO_2$ according to the T-dependence of $K_{CO/CO_2}$ and $K_{H_2/H_2O}$.

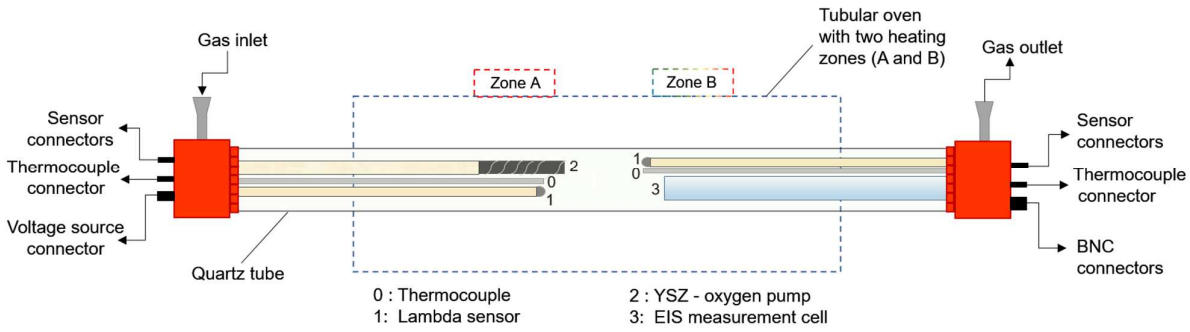


**Figure 21** Scheme of the impedance setup with integrated oxygen pump.

The impedance spectra are recorded using an impedance analyzer (Novocontrol Alpha A, Germany). The impedance spectra are acquired in the frequency range $10^6$–10 Hz with a voltage amplitude of 0.02 V (increased up to 0.6 V when the resistances are very high, to decrease scatter). The spectra can be fitted with a single resistance or an R-CPE circuit depending on the temperature and gas atmosphere. Different $pO_2$ are flowed by mixing different ratios of oxygen and nitrogen. The mixed gases can be humidified with a thermostated water evaporator (**Figure 22**). Gas flows are set by flow controllers (VACOM FCU-4, Germany). 0.5% of $CO_2$ is used as buffer gas for pumping experiments (in dry and humid conditions, added after the evaporator). This is necessary, otherwise in dry conditions only $H_2O$,$CO_2$ trace impurities could be reduced to $H_2$,CO and the stabilization of a low $pO_2$ would be very difficult.

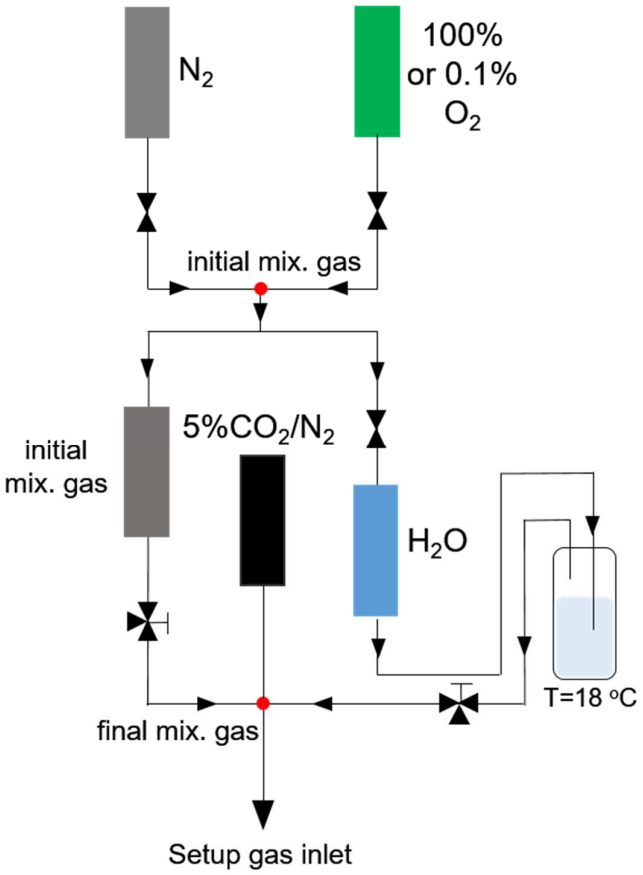


**Figure 22** Gas mixing setup connected to the cell inlet.

## 2.3 Exemplary Diffractograms and lattice parameters

Phase purity of the prepared samples powders was checked by XRD, Rietveld refinement was performed using the software HighScore Plus in order to extract the lattice parameters. Exemplary XRD pattern for the cubic and hexagonal perovskites, and orthorhombic structure are reported in **Figure 23**. While the orthorhombic perovskites also have corner-sharing $BO_6$ octahedra similar to the cubic perovskite, the hexagonal structure is based on face-sharing octahedra. The lattice parameters of the untreated and treated samples included in the present thesis are divided into four tables (**Table 2, Table 3, Table 4, Table 5**) referring to respective sections of the experimental chapter.

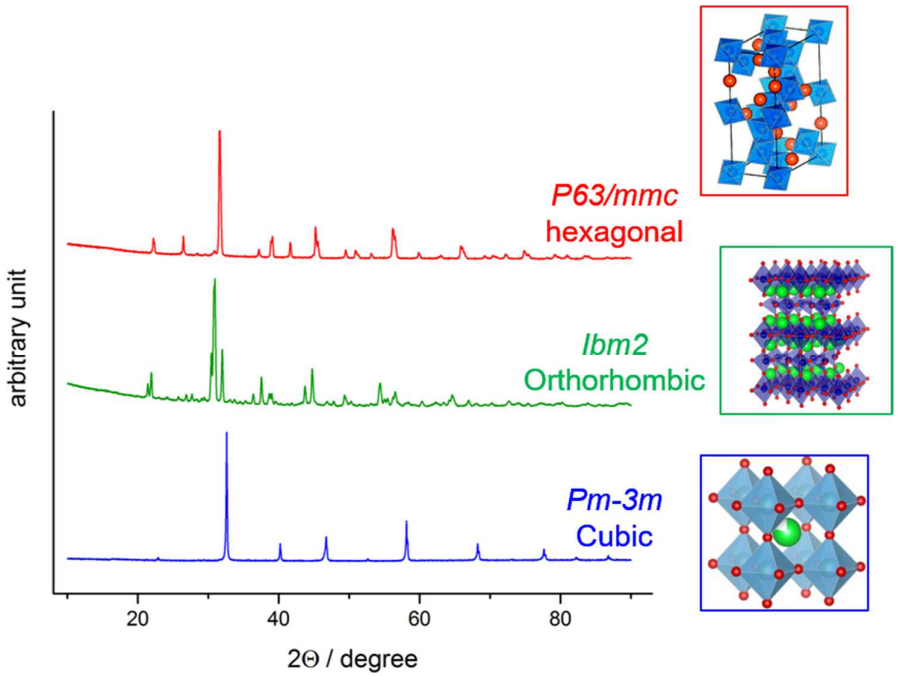


**Figure 23** Experimental XRD pattern of cubic B15SF (blue), orthorhombic BF (o-BF, green) and hexagonal BF (h-BF, red).

**Table 2** Lattice parameters from XRD for the deliberately oxidized and reduced samples included in **Section 3.1**. Also the oxygen stoichiometries of the samples are reported. The lattice parameters and sintering condition of the untreated samples are included in ref. [24].

| Sample | Stoichiometry | Lattice parameters / Å |
|---|---|---|
| SFox | $SrFeO_{3.00}$ | 3.85 |
| SFred | $SrFeO_{2.50}$ | 5.52; 5.67; 15.60<br>pseudocubic: 3.94 |
| BL25Fox | $Ba_{0.75}La_{0.25}FeO_{3.00}$ | 3.95 |
| BL25Fred | $Ba_{0.75}La_{0.25}FeO_{2.625}$ | 4.02 |
| BL5Fox | $Ba_{0.95}La_{0.05}FeO_{3.00}$ | 3.99 |
| BL5Fred | $Ba_{0.95}La_{0.05}FeO_{2.525}$ | 4.08 |
| BL5FZn20ox | $Ba_{0.95}La_{0.05}Fe_{0.8}Zn_{0.2}O_{2.825}$ | 4.06 |
| BL5FZn20red | $Ba_{0.95}La_{0.05}Fe_{0.8}Zn_{0.2}O_{2.425}$ | 4.08 |
| BFY20ox | $BaFe_{0.8}Y_{0.2}O_{2.90}$ | 4.14 |
| BFY20red | $BaFe_{0.8}Y_{0.2}O_{2.50}$ | 4.14 |
| BSFox | $Ba_{0.5}Sr_{0.5}FeO_{3.00}$ | 3.92 |
| BSFred | $Ba_{0.5}Sr_{0.5}FeO_{2.50}$ | 4.00 |
| BSFZn20ox | $Ba_{0.5}Sr_{0.5}Fe_{0.8}Zn_{0.2}O_{2.80}$ | 3.95 |
| BSFZn20red | $Ba_{0.5}Sr_{0.5}Fe_{0.8}Zn_{0.2}O_{2.40}$ | 4.01 |
| SFZn20ox | $SrFe_{0.8}Zn_{0.2}O_{2.80}$ | 3.86 |
| SFZn20red | $SrFe_{0.8}Zn_{0.2}O_{2.40}$ | 3.91 |

**Table 3** Lattice parameters from XRD, stoichiometries and sintering condition of the pellets for the samples included in **Section 3.2**.

| Sample | Stoichiometry | Sintering condition | Lattice parameters / Å |
|---|---|---|---|
| **BZYF0** | $BaZr_{0.88}Y_{0.12}O_{2.94}$ | 1600 °C x 6h | 4.22 |
| **BZYF01** | $BaZr_{0.82}Y_{0.12}Fe_{0.01}O_{3-\delta}$ | 1600 °C x 6h | 4.21 |
| **BZYF03** | $BaZr_{0.82}Y_{0.12}Fe_{0.03}O_{3-\delta}$ | 1600 °C x 6h | 4.21 |
| **BZYF06** | $BaZr_{0.82}Y_{0.12}Fe_{0.06}O_{3-\delta}$ | 1600 °C x 6h | 4.21 |
| **BZYF06ox** | $BaZr_{0.82}Y_{0.12}Fe_{0.06}O_{2.94}$ | | 4.21 |
| **BZYF06red** | $BaZr_{0.82}Y_{0.12}Fe_{0.06}O_{2.91}$ | | 4.21 |
| **BZYF10** | $BaZr_{0.82}Y_{0.12}Fe_{0.10}O_{3-\delta}$ | 1500 °C x 16h | 4.21 |
| **BZYF10ox** | $BaZr_{0.78}Y_{0.12}Fe_{0.10}O_{2.94}$ | | 4.21 |
| **BZYF10red** | $BaZr_{0.78}Y_{0.12}Fe_{0.10}O_{2.89}$ | | 4.21 |
| **BZYF20** | $BaZr_{0.82}Y_{0.12}Fe_{0.20}O_{3-\delta}$ | 1500 °C x 16h | 4.19 |
| **BZYF30** | $BaZr_{0.82}Y_{0.12}Fe_{0.30}O_{3-\delta}$ | 1500 °C x 16h | 4.19 |
| **BZYF30ox** | $BaZr_{0.58}Y_{0.12}Fe_{0.30}O_{2.94}$ | | 4.19 |
| **BZYF30red** | $BaZr_{0.58}Y_{0.12}Fe_{0.30}O_{2.79}$ | | 4.22 |
| **BZYF50** | $BaZr_{0.82}Y_{0.12}Fe_{0.50}O_{3-\delta}$ | 1450 °C x 16h | 4.16 |
| **BZYF70** | $BaZr_{0.82}Y_{0.12}Fe_{0.70}O_{3-\delta}$ | 1450 °C x 16h | 4.14 |
| **BZYF70ox** | $BaZr_{0.18}Y_{0.12}Fe_{0.70}O_{2.94}$ | | 4.23 |
| **BZYF70red** | $BaZr_{0.18}Y_{0.12}Fe_{0.70}O_{2.59}$ | | 4.21 |
| **BZYF80** | $BaZr_{0.82}Y_{0.12}Fe_{0.80}O_{3-\delta}$ | 1450 °C x 8h | 4.12 |

**Table 4** Lattice parameters from XRD, stoichiometries and sintering condition of the pellets for the samples included in **Section 3.3**.

| Sample | Stoichiometry | Sintering condition | Lattice parameters / Å |
|---|---|---|---|
| **BL5F** | $Ba_{0.95}La_{0.05}FeO_{3-\delta}$ | 1200 °C x 8h | 4.00 |
| **BL5FCo20** | $Ba_{0.95}La_{0.05}Fe_{0.8}Co_{0.2}O_{3-\delta}$ | 1200 °C x 8h | 4.04 |
| **BL5FNi20** | $Ba_{0.95}La_{0.05}Fe_{0.8}Ni_{0.2}O_{3-\delta}$ | 1100 °C x 8h | 4.02 |
| **BL5FCu20** | $Ba_{0.95}La_{0.05}Fe_{0.8}Cu_{0.2}O_{3-\delta}$ | 1100 °C x 8h | 4.02 |
| **BL5FCu10** | $Ba_{0.95}La_{0.05}Fe_{0.9}Cu_{0.1}O_{3-\delta}$ | 1100 °C x 8h | 4.01 |
| **BL5FZn20** | $Ba_{0.95}La_{0.05}Fe_{0.8}Zn_{0.2}O_{3-\delta}$ | 1200 °C x 8h | 4.05 |
| **BL5FZn10** | $Ba_{0.95}La_{0.05}Fe_{0.9}Zn_{0.1}O_{3-\delta}$ | 1200 °C x 8h | 4.05 |
| **BL5FCu10Zn10** | $Ba_{0.95}La_{0.05}Fe_{0.8}Cu_{0.1}Zn_{0.1}O_{3-\delta}$ | 1100 °C x 8h | 4.04 |

**Table 5** Lattice parameters from XRD, stoichiometries and sintering condition of the pellets for the samples included in **Section 3.4**.

| Sample | Stoichiometry | Sintering condition | Lattice parameters / Å |
|---|---|---|---|
| **o-BF** | $BaFeO_{2.5}$ | 1100 °C x 10h in 100% $N_2$ | 5.88; 16.52; 11.11 pseudocubic: 4.07 |
| **h-BF** | $BaFeO_{3-\delta}$ | 1100 °C x 10h in 100% $O_2$ | 5.67; 5.67; 13.94. |
| **BFMg10Ca10** | $BaFe_{0.8}Mg_{0.1}Ca_{0.1}O_{3-\delta}$ | 1100 °C x 8h | 4.08 |
| **h-BFMg10Ca10** | $BaFe_{0.8}Mg_{0.1}Ca_{0.1}O_{3-\delta}$ | 1300 °C x 8h | 5.73; 5.73; 14.13 |
| **BFMg10Y10** | $BaFe_{0.8}Mg_{0.1}Y_{0.1}O_{3-\delta}$ | 1300 °C x 8h | 4.11 |
| **BFZn10Zr10** | $BaFe_{0.8}Zn_{0.1}Zr_{.1}O_{3-\delta}$ | 1200 °C x 8h | 4.10 |
| **BFZn10Mg10** | $BaFe_{0.8}Zn_{0.1}Mg_{0.1}O_{3-\delta}$ | 1300 °C x 8h | 4.09 |
| **BFZr20** | $BaFe_{0.8}Zr_{0.2}O_{3-\delta}$ | 1350 °C x 8h | 4.18 |
| **BFZr10Ca10** | $BaFe_{0.8}Zr_{0.1}Ca_{0.1}O_{3-\delta}$ | 1200 °C x 8h | 4.09 |
| **BFCa10** | $BaFe_{0.9}Ca_{0.1}O_{3-\delta}$ | 1100 °C x 8h | 4.08 |
| **h-BFMg20** | $BaFe_{0.8}Mg_{0.2}O_{3-\delta}$ | 1200 °C x 8h | 5.69; 5.69; 13.99 |

# 3 Results and Discussion

## 3.1 Barium ferrate with redox-inactive dopants

In this section, the results of a series of doped barium ferrates with Sr or La in the A-site and Zn or Y in the B-site are reported and discussed. They all show the simple cubic perovskite structure. The composition discussed in this section are: BL5F, BL25F, BL5FZn20, BFY20, BSF, BSFZn20, SF, and SFZn20 all in their reduced and oxidized form. These compositions are studied to obtain a comprehensive answer to the remaining open questions from previous studies [24, 32, 48-49] such as the interplay of iron formal oxidation state, oversized dopants, Fe-O covalency and charge (de)localization on the proton uptake of triple conducting perovskites.

### 3.1.1 Effects of the dopants on proton uptake

The dependence of proton uptake on the cation compositions included in this section are published in ref. [24] and refer to the proton concentration measured for $N_2$-quenched samples (iron mainly 3+) at 250 °C in 16.7 mbar $pH_2O$ (**Eq. 2**). These data are summarized in **Figure 24**. 5% of La is added to the pure barium ferrate for retaining the cubic perovskite structure. Several interesting trends can be recognized. An increased amount of Sr at expense of Ba is detrimental for proton uptake. For the B15SF which is the most Ba-depleted, the sample is still keeping the cubic perovskite structure, the proton uptake decreases to only 0.14%. Since the $V_O^{\bullet\bullet}$ concentration is approximately constant, this trend can qualitatively be related to the increased overall basicity of Ba-rich compositions. $SrFeO_{2.5}$ represents a specific case as it adopts the Brownmillerite structure with ordered $V_O^{\bullet\bullet}$ arrangement, which decreases their propensity for hydration, *cf.,* **Section 3.4**. Adding 20% of Zn in the B-site increases the proton concentration by roughly 3 times, 20% of Y instead doubles it. The increased proton uptake of compositions doped with the oversized Zn and Y not only depends on the moderate increase of the oxygen vacancy concentration. This becomes particularly clear by comparing the $V_O^{\bullet\bullet}$ concentration in BL5F and BFY20 where the difference is just 0.03, *i.e.,* a relative increase by 5%. In fact, the oversized dopants have several beneficial effects on proton uptake: (i) replacing some Fe with larger and/or less charged cations increases the overage basicity of the cations, (ii) local lattice distortions (Fe-O-Fe buckling) [37] lead to decreased Fe-O covalency [37, 47] which increases the basicity of the oxide ions. It is clear that these phenomena are not mutually independent and they will be discussed in detail in the following sections.

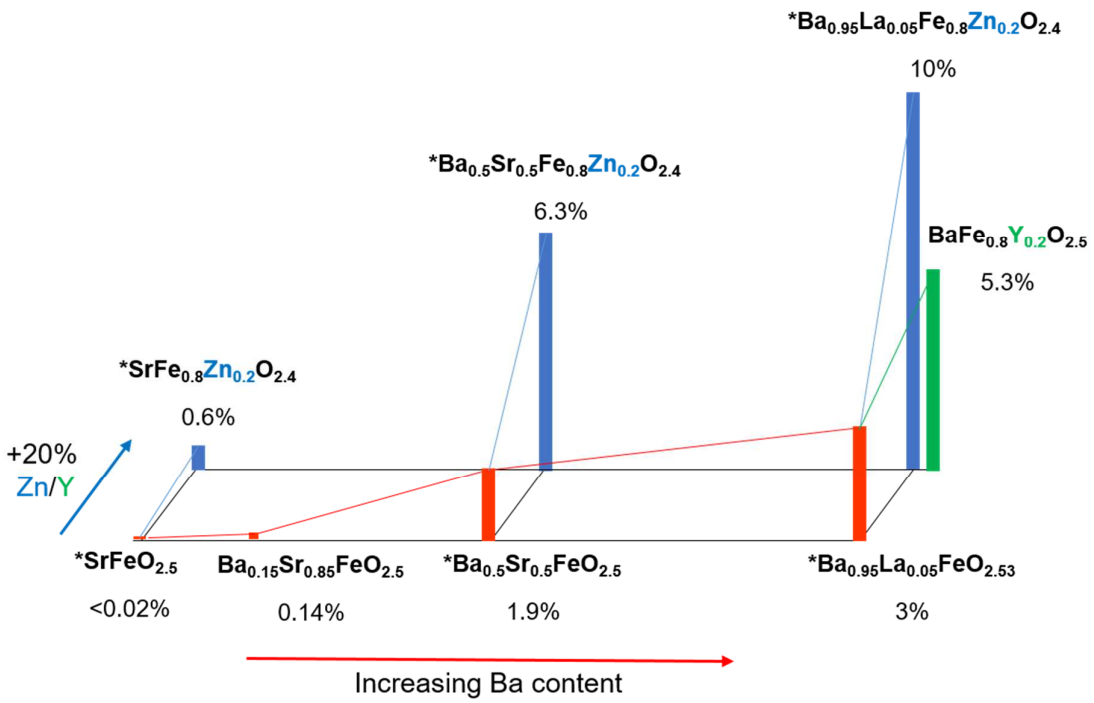


**Figure 24** Proton uptake of (Ba, Sr, La)(Fe, Zn, Y)$O_{3-\delta}$ at 250 °C in 16.7 mbar $pH_2O$. The samples were quenched from $N_2$ at 900 °C. The red lines emphasize the effect of Ba vs Sr content; the blue and green lines refer to the effect of the oversized dopants Zn (blue) and Y (green). Data taken from ref. [24]. *Data measured by Dr. Reihaneh Zohourian. The hydration plots of B15SF and BFY20 are included in **Appendix A**.

### 3.1.2 Effects of the dopants on the local structure

As anticipated in **Section 2.2.4**, EXAFS spectra contain quantitative information about the local atomic arrangements. This information is complementary to the XRD analysis for which just the long-range order can be extracted, losing the information on the different B-A, B-B distances arising from the different elements residing on the perovskite A- and B-sites. A fitting of the EXAFS signal yields a distribution of B-A, B-B distances owing to the different ionic radii of the cations in the material.

Oxidized and reduced samples were measured at the Fe, Zn, Y *K*-edges. Already by a visual inspection of the exemplary FTs in **Figure 25**, it is clear that reduced samples generally exhibit more local disorder than oxidized samples. Zn/Y doped samples are significantly disordered even in their oxidized form. Moreover, the Zn local environment is more disordered than that of yttrium. The results of this section are published in ref. [37].

The fitting results (obtained applying the model discussed in **Section 2.2.4**) for all compositions are reported in **Table 6**. In the perovskite structure the local environment of the B-cation is composed by: (i) First shell B-O with six oxygen atoms (or less when taking into account the oxygen non–stoichiometry). (ii) Second shell with eight A –site cations (since the A site is composed by Ba, Sr, or La they are fitted as separate subshells considering their different ionic radii [50]). (iii) Third shell B-B with six B site atoms, for doped sample the third shell also contains the Fe-M distances with the coordination number fixed according to the cation stoichiometry. The MSPs like B-O-B and B-O-B-O being linear or buckled have a strong effect on the signal of the third shell.

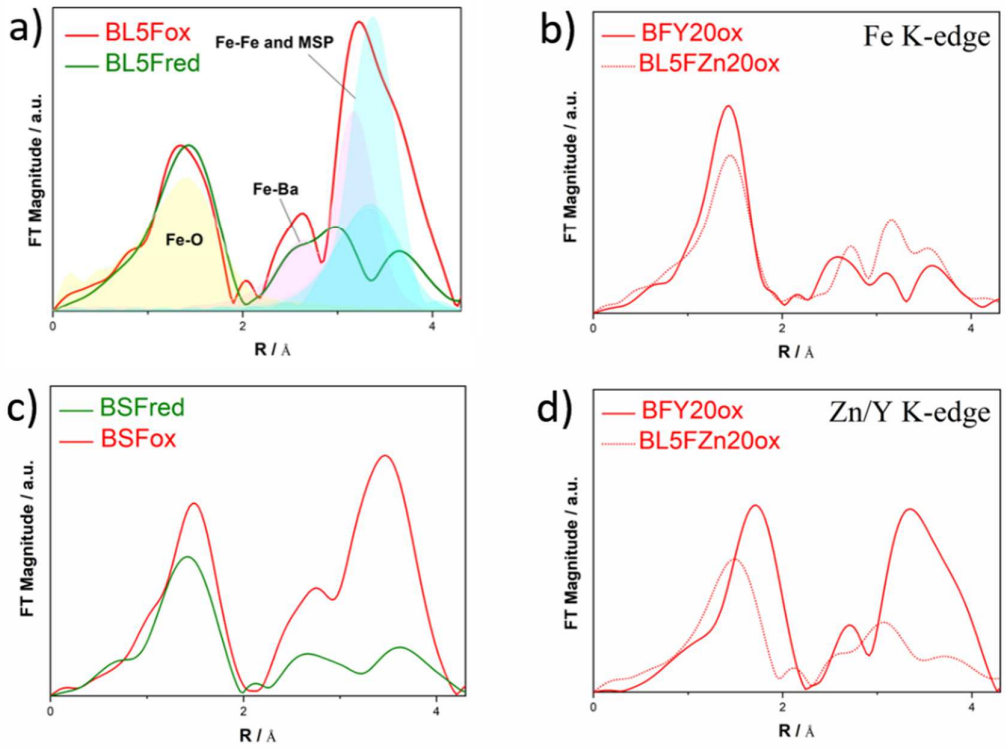


**Figure 25** Fourier transforms of the EXAFS function of representative samples. (a) Fe *K*-edge of BL5Fox/red. In BL5Fox, the colour shading highlights the shell contributions (yellow: first shell, pink: second shell, cyan: third shell). (b) Fe *K*-edge of BL5FZn20ox and BFY20ox. (c) Fe *K*-edge of BSFox/red (d) Zn *K*-edge of BL5FZn20ox, and Y *K*-edge of BFY20ox. Note that owing to the phase shift the position of the maxima does not directly match the respective atomic distances.

**Table 6** Fitting results, top number: path length $R$ in Å, bottom: Debye-Waller factor $\sigma^2$ in $10^{-3}$ Å$^2$. M=Zn or Y.

| | **BL25F** | | **BL5F** | | **BL5FZn20** | | **BFY20** | |
|---|---|---|---|---|---|---|---|---|
| | *ox* | *red* | *ox* | *red* | *ox* | *red* | *ox* | *red* |
| **Fe–O** | 1.98 | 1.99 | 1.95 | 1.95 | 1.92 | 1.92 | 1.89 | 1.91 |
| | 9 | 18 | 11 | 9 | 10 | 8 | 7 | 7 |
| **M–O** | | | | | 1.97 | 1.97 | 2.27 | 2.28 |
| | | | | | 16 | 11 | 4 | 4 |
| **Fe–Ba** | 3.40 | 3.47 | 3.42 | 3.40 | 3.40 | 3.41 | 3.46 | 3.41 |
| | 2 | 8 | 4 | 13 | 11 | 10 | 10 | 11 |
| **M–Ba** | | | | | 3.42 | 3.41 | 3.56 | 3.57 |
| | | | | | 16 | 28 | 8 | 9 |
| **Fe–La** | 3.40 | 3.31 | | | | | | |
| | 2 | 4 | | | | | | |
| **Fe–Fe** | 3.96 | 3.93 | 3.90 | 3.85 | 3.72 | 3.78 | 3.71 | 3.78 |
| | 8 | 10 | 9 | 11 | 18 | 25 | 30 | 30 |
| **Fe–M** | | | | | 3.89 | 3.83 | 4.14 | 4.17 |
| | | | | | 3 | 24 | 7 | 7 |
| **Fe–Fe–O** | 3.96 | 3.96 | 3.90 | 3.88 | 3.78 | 3.81 | 3.74 | 3.79 |
| | 3 | 8 | 10 | 11 | 11 | 10 | 26 | 13 |
| **Fe–M–O** | | | | | 3.89 | 3.86 | 4.15 | 4.18 |
| | | | | | 5 | 15 | 5 | 7 |
| **Fe–O–Fe–O** | 3.96 | 3.99 | 3.90 | 3.90 | 3.83 | 3.85 | 3.77 | 3.81 |
| | 11 | 18 | 7 | 9 | 9 | 8 | 9 | 13 |
| **Fe–O–M–O** | | | | | 3.89 | 3.89 | 4.17 | 4.19 |
| | | | | | 2 | 15 | 9 | 9 |

| | **BSF** | | **BSFZn20** | | **SFZn20** | | **SF** |
|---|---|---|---|---|---|---|---|
| | *ox* | *red* | *ox* | *red* | *ox* | *red* | *ox* |
| **Fe–O** | 1.97 | 1.93 | 1.91 | 1.92 | 1.92 | 1.95 | 1.95 |
| | 8 | 8 | 11 | 6 | 9 | 6 | 14 |
| **M–O** | | | 2.01 | 1.96 | 1.98 | 1.99 | |
| | | | 9 | 7 | 8 | 10 | |
| **Fe–Ba** | 3.38 | 3.39 | 3.35 | 3.32 | | | |
| | 2 | 3 | 2 | 4 | | | |
| **M–Ba** | | | 3.37 | 3.37 | | | |
| | | | 12 | 23 | | | |
| **Fe–Sr** | 3.38 | 3.39 | 3.36 | 3.33 | 3.35 | 3.31 | 3.31 |
| | 3 | 7 | 2 | 10 | 4 | 13 | 6 |
| **M–Sr** | | | 3.34 | 3.32 | 3.10 | 3.09 | |
| | | | 15 | 25 | 10 | 10 | |
| **Fe–Fe** | 3.94 | 3.83 | 3.74 | 3.76 | 3.84 | 3.91 | 3.88 |
| | 3 | 6 | 5 | 2 | 10 | 5 | 2 |
| **Fe–M** | | | 3.89 | 3.81 | 3.92 | 3.94 | |
| | | | 3 | 2 | 13 | 11 | |
| **Fe–Fe–O** | 3.94 | 3.84 | 3.78 | 3.80 | 3.84 | 3.91 | 3.89 |
| | 4 | 12 | 13 | 5 | 2 | 9 | 4 |
| **Fe–M–O** | | | 3.90 | 3.84 | 3.93 | 3.94 | |
| | | | 3 | 2 | 12 | 9 | |
| **Fe–O–Fe–O** | 3.94 | 3.85 | 3.83 | 3.84 | 3.84 | 3.91 | 3.91 |
| | 12 | 8 | 4 | 2 | 2 | 10 | 2 |
| **Fe–O–M–O** | | | 3.91 | 3.88 | 3.93 | 3.94 | |
| | | | 4 | 2 | 15 | 2 | |

*Discussion of first and second shells.* All samples show fairly similar first shell coordination distances (see **Figure 26(a)**). Fe-O are in the range 1.89-1.98 Å for oxidized and 1.91-1.99 Å for the reduced samples. The increased distance for reduced samples is in agreement with the "chemical expansion" of the lattice parameter upon reduction. This is observed also for other iron perovskites [36, 51]. The M-O distances are longer than Fe-O and less sensitive to the oxidation/reduction treatment. In reduced samples, the disorder in the first shell is generally higher because of the increased static disorder arising from the high number of oxygen vacancies. The second shell distances do not show systematic variation between oxidized and reduced samples (**Figure 26(b)**).

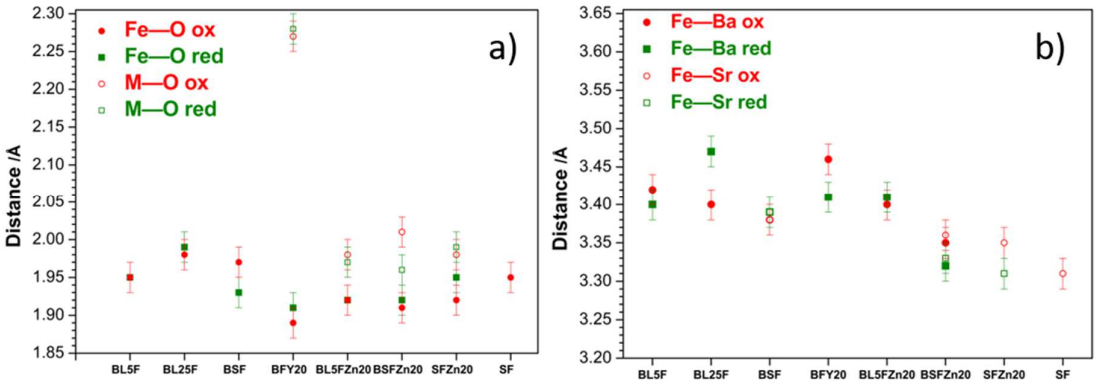


**Figure 26** (a) First shell Fe/M-O distances in oxidized (red) and reduced (green) samples (M= Zn or Y). (b) Second shell Fe-Ba, Fe-Sr distances in oxidized (red) and reduced (green) samples.

*Discussion of the third shell.* The third shell shows more pronounced differences among these samples. The B-site undoped oxidized samples (BL5F, BL25F and BSF) show pronounced third shell peaks indicating ordered atoms arrangements. A strong decrease of these peaks occurs either via reduction (green curves in **Figure 25(a-c)**), by increasing oxygen vacancy concentration and related distortion, or via doping of the B-site with Zn or Y (**Figure 25(b-d)**). The third shell includes the contribution from the MSPs, and in particular the B-O-B MSPs can give information regarding a nonlinear arrangement of the $BO_6$ octahedra. This is typically observed for reduced and/or oversized cation doped samples.

The disorder in the third shell is higher in the reduced samples compared to the oxidized. It increases drastically with the partial substitution of iron with oversized zinc or

yttrium. At such high level of static disorder, the third shell features in the FTs are almost completely washed out. This correlates with the deviations of the B-O-B connections from linearity. From **Table 6** it can be noticed that the majority of B-B distances are shorter than twice the B-O distance (in a perfectly linear geometry then they should be equal), and B-O-B paths are longer than B-B distances, which is a clear evidence of B-O-B buckling.

These deviations from the collinear arrangements are well visible in **Figure 27** where the effect of the buckling of Fe-O-Fe(M) is summarized for the different samples.

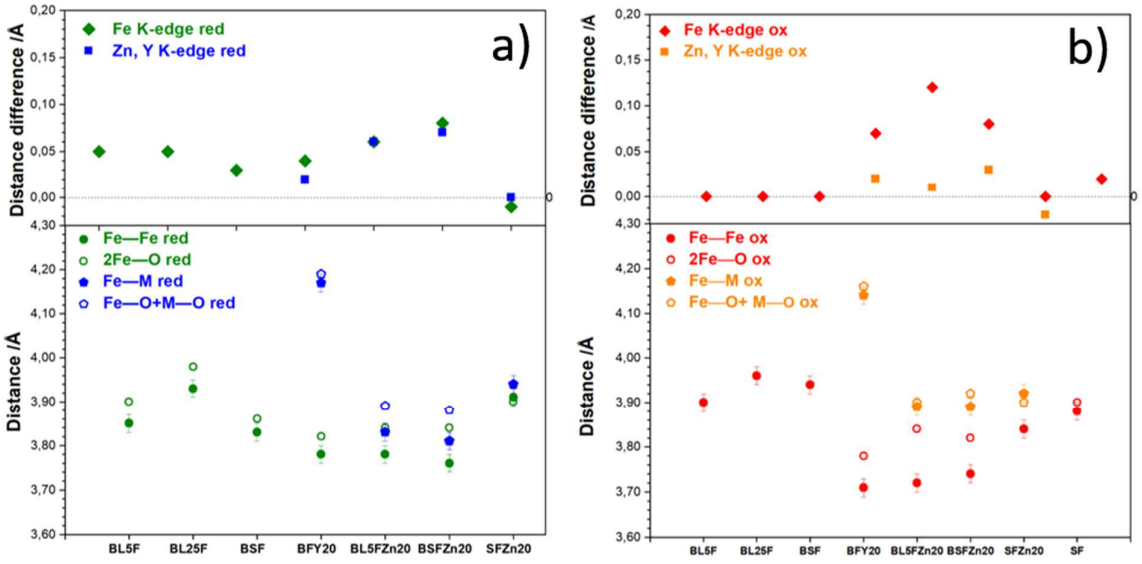


**Figure 27** (Bottom) Fe-Fe and Fe-M direct distances (solid symbols, M= Zn or Y) compared to 2 • Fe-O and Fe-O+M-O (open symbols). (Top) Difference between Fe-Fe and 2 • Fe-O (diamonds) and Fe-M and Fe-O+M-O (squares). A difference of 0.1 Å corresponds to a buckling angle of ≈154°.

Reduced samples show Fe-O-Fe buckling even without B-site dopants, and this can be related to the presence of the high oxygen vacancy concentration (0.37-0.6 $V_O^{\bullet\bullet}$ per formula unit). This agrees well with DFT calculations of $BaFeO_{3-\delta}$ carried out by Hoedl et al. [52]. The buckling of the reduced BFY20 is comparable with the reduced BL5F and BSF, while Zn-doped samples show larger buckling angles.

For the oxidized samples without Zn/Y the data indicate collinear Fe-O-Fe arrangements reflecting the ideal cubic perovskite structure. Instead, oxidized doped

samples show bent Fe-O-Fe configurations. Oxidized Zn/Y doped samples still contain 0.1-0.2 $V_O^{\bullet\bullet}$ per formula unit, and compared to the reduced undoped ones (0.38-0.5 $V_O^{\bullet\bullet}$) the first show a much larger Fe-O-Fe buckling. This argument indicates that the strong buckling in Zn/Y doped samples cannot be explained just in terms of vacancy concentration alone, but it is largely caused by the presence of the oversized dopant. Interestingly, among the doped samples SFZn20 does not show any distortion. This may have two reasons: (i) SF has a stiffer lattice than BF [53], which disfavours distortion. (ii) The outward displacement of a B-cation close to a vacancy is smaller when the B-site dopant is strongly oversized because of the lack of available space ($Zn^{2+}$ is more oversized in respect to Fe and the lattice parameter in SF than in BF).

The Fe-O-M arrangements are less distorted than the Fe-O-Fe configurations. Furthermore, the Fe-O-Zn configuration is more distorted than Fe-O-Y. This is once again in agreement with DFT calculations (supplementary information of ref. [37]).

Summarizing, the combination of $V_O^{\bullet\bullet}$ with oversized B-site dopants appears most effective to bend Fe-O-Fe and Fe-O-M arrangements. This has important implications for the electronic structure of the material. It is well known for perovskite that the width of the band formed by the hybridization of cation *3d* and oxygen *2p* orbitals decreases strongly when bent B-O-B connections are present [54-56]. This topic will be expanded in the following **Section 3.1.3**.

### 3.1.3 Effect of the dopants on the electronic structure

The oxygen, iron and dopants XANES spectra contain important information regarding the oxidation states, the average coordination numbers and other electronic features such as the degree of covalency of TM-O bonds. The iron, zinc and yttrium XANES can be measured using standard XAS. However, this is not the preferred technique for oxygen, since it would require soft X-rays, which makes the experiment surface sensitive while here bulk sensitivity is desired. Therefore, XRS employing hard X-rays was used for recording the oxygen XANES. The results of this section are submitted for publication [47].

*Discussion of the oxygen XANES.* O *K*-edge excitations before photoelectron ejection to the continuum correspond to electronic transitions from the O *1s* core level to *2p* states hybridized with the TM*3d* states. These reflect the extent of the covalency between O*2p* and TM*3d* orbitals (TM=Fe, Zn, Y) [57]. **Figure 28** reports the O *K*-edge of the measured samples in their oxidized and reduced forms. The first double feature in the pre-edge region between 525 and 530 eV (peak a in **Figure 28**) is attributed to

bands of mixed O *2p* and TM *3d* character. The second peak (b) corresponds to bands deriving from Ba/La *5d* electronic states. The broad, intense peak at 540 eV (c) is attributed to bands of mixed O *2p* and TM *4s* and *4p* character [58]. The reduced samples show a significant variation in the peak positions: (i) a strong shift of the pre-edge peak(a) at 528 eV to higher energy by ~ 2 eV; (ii) peak(b) at 536 eV appears broadened and less resolved and shifted to lower energy by 1.5 eV, which is stronger in the case of BFYred; (iii) peak(c) is largely suppressed. Interestingly, even in the case of the oxidized samples peak(a) is broader in the Zn,Y doped compositions.

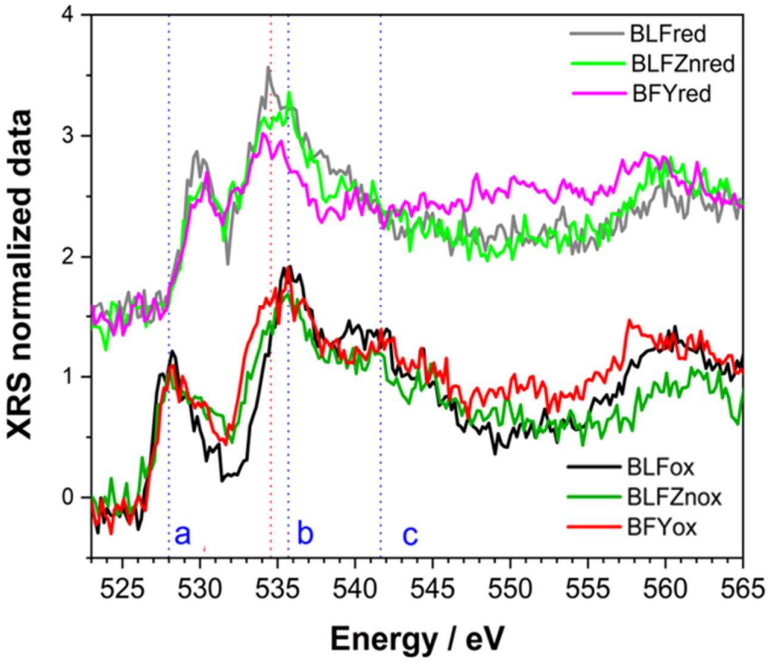


**Figure 28** O *K*-edge spectra of all samples from XRS. The reduced samples are shifted vertically for clarity. The blue vertical lines represent the position of the characteristic electronic features (a,b,c) for the oxidized samples. The red vertical line shows the shift of BFY20 in respect to the other compositions.

The changes in the shape of the O *K*-edge for the reduced samples reflect the rearrangement of oxygen orbitals and the redistribution of charge by the reduction process. In fact, the pre-edge features (peak(a)) are associated to the σ* (π*) molecular orbitals in barium ferrate perovskites, which originate from the anti-bonding mixture of TM (mainly Fe) *3d* $e_g$ and $t_{2g}$ and O *2p* states [59]. The variation in the oxygen stoichiometry, and thus effective TM oxidation state, can modify the pre-edge features.

In order to extract quantitative information, simulations of the spectra are performed according to the methodology described in **Section 2.5.5**. The results are displayed in **Figure 29**.

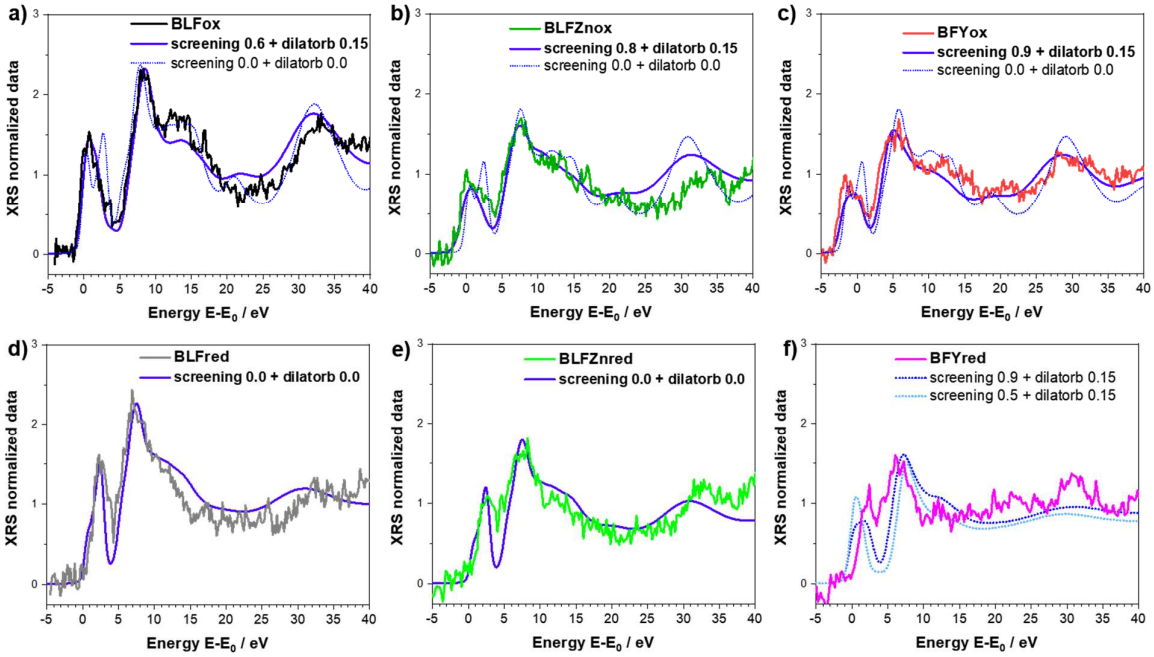


**Figure 29** Best simulation (blue solid lines, convoluted) obtained for (a) BL5Fox, (b) BL5Fred, (c) BL5FZn20ox, (d) BL5FZn20red, (e) BFY20ox, (f) BFY20red. The necessity of using the *screening* and *dilatorb* parameters for oxidized samples is emphasized in the top panels where the simulations with *screening* 0 and *dilatorb* 0 are reported as dashed lines.

The spectra of the oxidized samples (**Figure 29(a,b,c)**) can be simulated well by applying a *dilatorb* value of 0.15 and *screening* values of 0.6 (BL5F), 0.8 (BL5FZn20) and 0.9 (BFY20). The *screening* value in the oxidized undoped sample is smaller than for Zn,Y-doped oxidized samples. This indicates an electron transfer to the TM*3d* orbitals, so the formal charge of the oxygen ion is less negative in the undoped sample compared to the doped. In other words, the doping helps to minimize the hybridization of the O*2p*-Fe*3d* orbitals. As already mentioned in **Sections 3.1.1** and **3.1.2**, the local distortion (Fe-O-Fe buckling) can cause this decreased hybridization. Moreover, this observation agrees with the proton uptake measurements reported in ref. [24] and in **Figure 24**, where Y and Zn doped samples exhibit a significantly higher proton concentration than undoped BL5F. A more negatively charged oxide ion is more basic and therefore more favourable for proton attachment. The screening value for simulating

BFY20ox is slightly higher than BL5FZn20. This is not necessarily a contradiction to the larger proton uptake of BL5FZn20. The presence of too strong structural rearrangements ($Y^{3+}$ is more oversized than $Zn^{2+}$) may be detrimental for the proton uptake because of energetically non-equivalent oxygen sites (this is well known *e.g.,* for $BaCe_{1-x}Y_xO_{3-\delta}$ [1]), and also the different charge may have a perceptible effect.

For the reduced samples, both *screening* and *dilatorb* are equal to 0. This means that for the reduced samples the core hole charge is completely screened (no electron charge is missing) and thus no additional screening influence needs to be added by the *screening* parameter. This situation corresponds to comparably small interaction with the *3d* states of the TMs. In addition, a zero *dilatorb* indicates a reduced overlap of the oxygen hybridized orbital with the TM, which might be related to the larger Fe-O distance as well as to the decreased effective Fe charge. As anticipated in **Section 2.5.5**, the use of the semi-empirical parameter *screening* and *dilatorb* in the simulation works well when only small structural rearrangements are present. Considering that (i) the Fe-$V_O^{\bullet\bullet}$-Fe atomic arrangement is energetically more favored than Y-$V_O^{\bullet\bullet}$-Fe (see refs. [37, 47]), and (ii) the high concentration of oxygen vacancies, it is not surprising that this methodology fails for BFY20red (**Figure 29(f)**). In fact, in BFY20red the iron has mainly a 5-fold and to some degree even 4-fold coordination. Therefore, after exploring different configurations with $FeO_5$ coordination, the best agreement with the experimental data is achieved by averaging several simulated spectra starting from a strongly distorted perovskite with penta-coordinated iron (configuration B in **Figure 30**) and slightly modifying the B-cations coordinates. This is summarized in **Figure 30**.

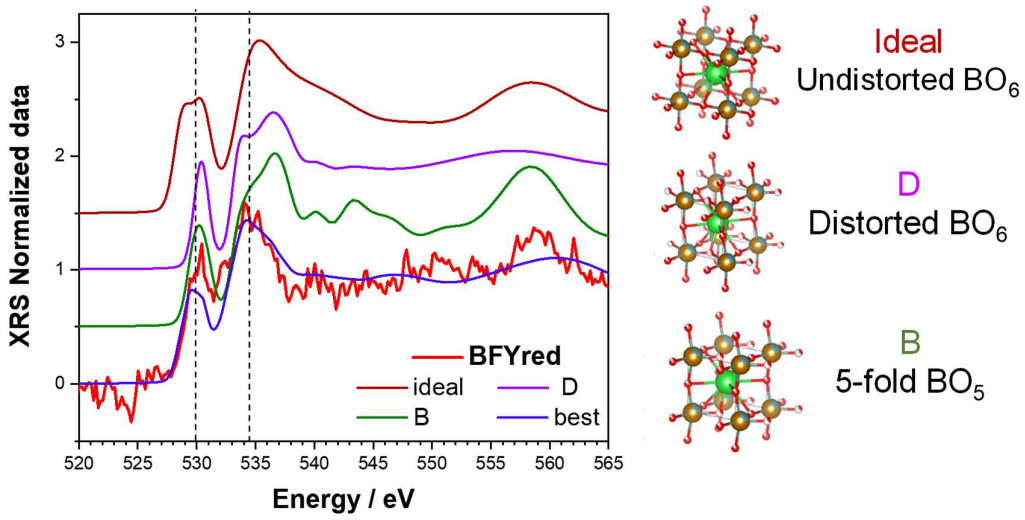


**Figure 30** Calculated O *K*-edge for different reasonable perovskite structures: ideal (undistorted $BO_6$), D (distorted $BO_6$), B (distorted $BO_5$) and best (average of possible configurations with 5-fold B-site). Atoms in the ball-and-stick sketches: red=O (with partial occupancy), gold/grey=Fe/Y, green=Ba.

*Discussion of the iron XANES.* **Figure 31** shows the XANES of the iron *K*-edge of all samples. SFox ($SrFeO_3$) and SFred ($SrFeO_{2.5}$) are highlighted since used as standards for $Fe^{4+}$ and $Fe^{3+}$. The position of the edge and pre-edge peak both depend on the effective charge of the transition metal [36, 60-63].

In all samples, one can recognize four characteristic features: (i) pre-edge peak (≈7115 keV), (ii) narrow white line (≈7132 keV), (iii) two shallow peaks (≈7138 and 7145 keV). The pre-edge is rather sharp for reduced samples, broader and shifted to higher energies for the oxidized ones. Interestingly, the pre-edge position and shape for BFY20 is unchanged between ox and red (highlighted in **Figure 31(a)**). The edge position of oxidized samples shifts to higher energy (**Figure 31(b)**) and is more pronounced for SFox and SFred with a difference of ≈2 eV. The peaks positions and the shift to higher energy for oxidized samples are consistent with the one observed for $Sr(Ti,Fe)O_{3-\delta}$ in ref [36]. It is important to notice that the edge positions for BFY20ox and BL5FZn20ox are shifted to lower energies (*e.g.,* closer to the $Fe^{3+}$ standard) than for the other samples. A list of the pre-edge and half-edge positions for all samples and their shift from ox to red are summarized in **Table 7**. While the absorption edges and pre-edge features for

the reduced samples are rather similar, stronger variations can be detected for the oxidized samples.

It is widely accepted that the effective oxidation state of a transition metal cation, which is reflected in the edge position, is significantly lower than its formal oxidation state, especially for 4+ cations. The decreased effective oxidation state can be attributed to the partial transfer of electron holes from $Fe^{4+}$ to the adjacent oxygen ions [60, 64-65]. The variation in the pre-edge peak and edge position in **Table 7**, **Figure 31** and **Figure 32** clearly demonstrate that the degree of this hole transfer strongly depends on the perovskite's composition. BL5FZn20 and BFY20 are the samples showing a smaller shift upon oxidation, indicating the iron effective charge is closer to 3+ than 4+. This may be explained by the fact that the partial substitution of iron with Zn and Y increases the overall basicity of the perovskite, which allows for more electron transfer from oxygen to iron, thus decreasing the effective iron oxidation state. This effect is weaker in barium ferrate based materials (higher basicity because of the larger A-site) than in strontium ferrate based one (lower basicity).

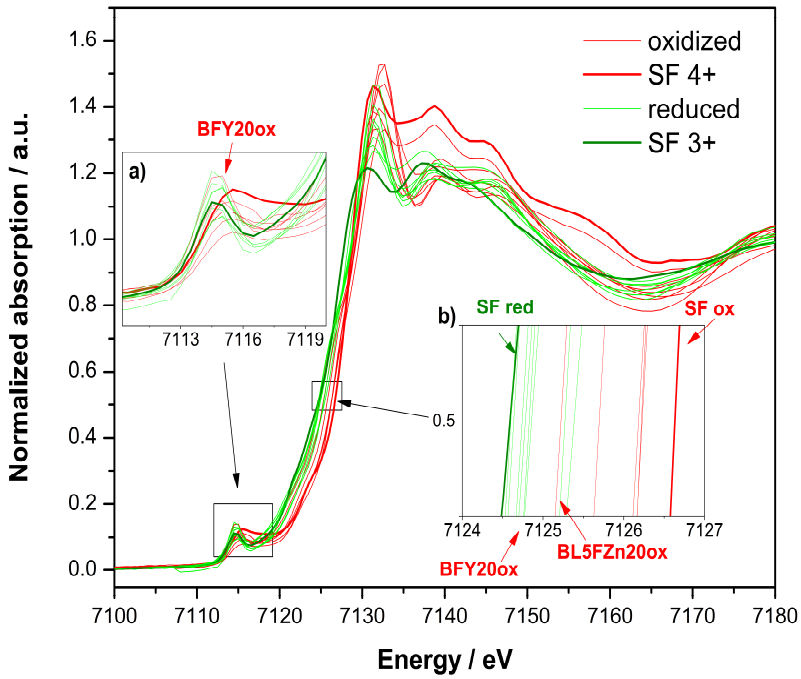


**Figure 31** XANES of the Fe *K*-edge of the reduced samples (light green), oxidized samples (red). SFred and SFox are emphasized by bold lines. Inset (a) is a magnification of the pre-edge region; inset (b) shows the half-height of the main edge region.

**Table 7** (a) Energy of main Fe *K*-edge (energy at half height), (b) energy of the pre-edge peak of oxidized and reduced samples and energy difference of oxidized and reduced samples.

| a) | Energy of main edge / eV | | Energy |
|---|---|---|---|
| | ox | red | difference / eV |
| **SF** | 7126.6 | 7124.6 | 2.0 |
| **SFZn20** | 7126.6 | 7125.4 | 1.2 |
| **BSF** | 7126.2 | 7124.9 | 1.3 |
| **BSFZn20** | 7126.2 | 7124.8 | 1.4 |
| **BL25F** | 7126.2 | 7125.3 | 0.9 |
| **BL5F** | 7125.7 | 7124.8 | 0.9 |
| **BL5FZn20** | 7125.2 | 7124.6 | 0.6 |
| **BFY20** | 7124.7 | 7124.7 | < 0.1 |

| b) | Energy of pre-edge peak/ eV | | Energy |
|---|---|---|---|
| | ox | red | difference / eV |
| **SF** | 7115.5 | 7114.5 | 1.0 |
| **SFZn20** | 7115.6 | 7114.7 | 0.9 |
| **BSF** | 7115.4 | 7114.7 | 0.7 |
| **BSFZn20** | 7115.2 | 7114.7 | 0.5 |
| **BL25F** | 7115.4 | 7114.8 | 0.6 |
| **BL5F** | 7115.0 | 7114.6 | 0.6 |
| **BL5FZn20** | 7115.0 | 7114.8 | 0.2 |
| **BFY20** | 7114.8 | 7114.6 | 0.2 |

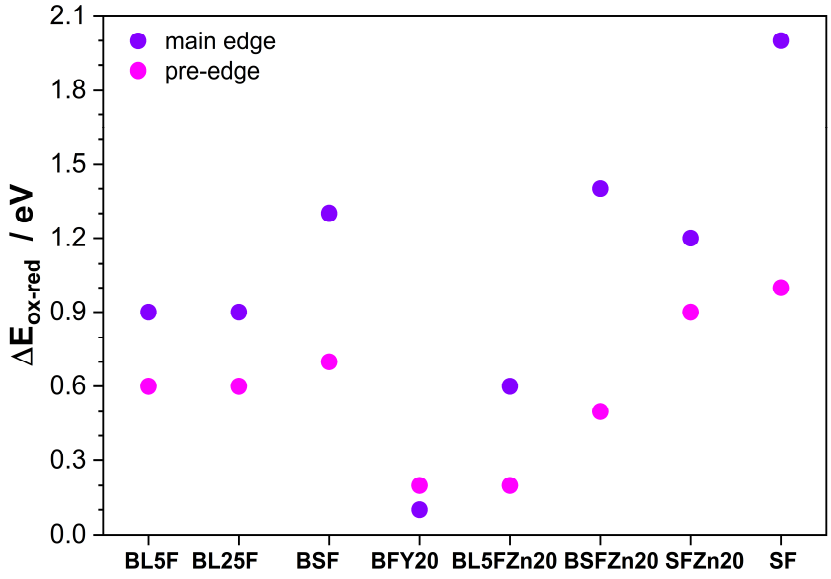


**Figure 32** $\Delta E_{ox\text{-}red}$ of the main Fe *K*-edge (at half-height of the main edge) and pre-edge for all compositions.

For selected compositions (BL5F, BL5FZn20 and BFY20 in their oxidized and reduced forms), the iron XANES spectra were analysed more thoroughly using FDMNES. Having a very disordered local environment, it is clear that just using the *screening* and *dilatorb* parameters for simulating the Fe *K*-edge will not yield a satisfactory set of simulations. Therefore, assuming that the geometrical modifications identified for the oxygen *K*-edge are also valid for the iron environment, the spectrum of the iron in 5-fold arrangement was calculated (without *dilatorb* or *screening*). It was then added with a suitable weighting to the simulated signal of an ideal (6-fold) structure, initially used for simulating BL5Fox (*dilatorb* 0.1 and *screening* 0.7, *cf.*, [47]). Iron in doped and reduced samples can exhibit both six-fold and five-fold coordination. The latter represents the strongest distortion detected for the local iron environment (however, minor contributions from other arrangements such 4-fold cannot fully be excluded). By suitably summing up these two extreme configurations, the average local iron arrangement in the different samples can be simulated. This procedure assumes that the oxygen vacancies formed upon reduction and/or by Zn or Y doping, are mainly located in the vicinity of iron. This procedure is demonstrated for BL5Fox, BL5Fred, BL5FZn20red and BFY20red in **Figure 33**.

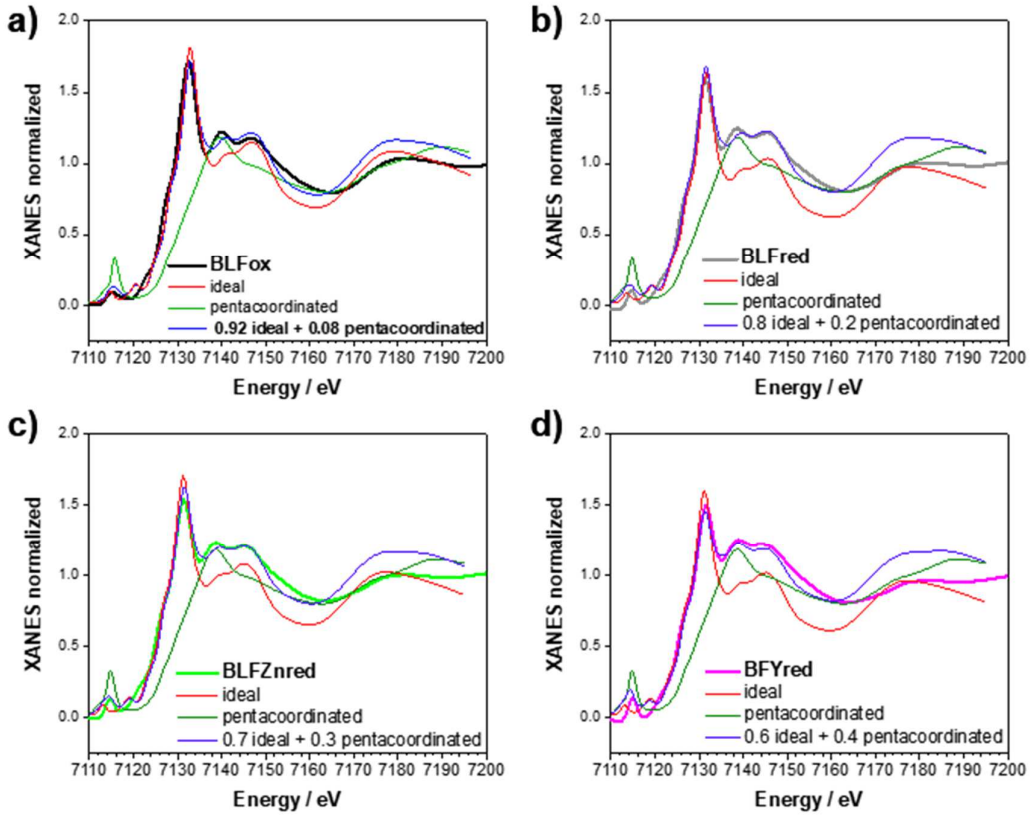


**Figure 33** Fe *K*-edge XANES simulation of (a) BL5Fox, (b) BL5Fred, (c) BL5FZn20red and (d) BFY20red. The best simulations are obtained combining 5-fold (green) and 6-fold (red) contributions. The best-weighted sum of the two components is reported in blue.

For BL5Fox, it is possible to reproduce the experimental data by summing 92% of the ideal structure (*screening* 0.7, *dilatorb* 0.1) and 8% of the penta-coordinated one (no *dilatorb* or *screening*). Here, the amount of distorted structure needed to achieve a satisfactory simulation is sensibly lower than for the other samples, suggesting that just very small modification of the iron local environment is occurring, as already expected from **Section 3.1.2** and ref. [37].

The experimental BL5Fred spectrum is best simulated combining 80% of ideal structure and 20% of the penta-coordinated arrangement. Interestingly, the observed white line intensity decrease correlates with the increased contribution of the distorted component, which amounts to 30 and 40 % for the Zn, and Y doped samples (**Figure 33(c-d)**). This result agrees with the probability of having the iron in 5-fold coordination in this structure considering the high vacancy concentration of the samples. The fact that

BFY20 shows a higher percentage of the distorted component compared to BL5FZn20 is ascribed to the different energies calculated for different atomic arrangements. As already mentioned, the Fe-$V_O^{\bullet\bullet}$-Fe configuration is energetically more favoured than Y-$V_O^{\bullet\bullet}$-Fe; instead, Zn-$V_O^{\bullet\bullet}$-Fe prevails for BL5FZn20. This is also supported by the observation at the dopant's *K*-edges.

*Discussion of the zinc and yttrium XANES.* At the Zn *K*-edge (**Figure 34(a)**) small but significant changes are evidenced in the white line intensity between the oxidized and reduced samples. No variations are detected, instead, at the Y *K*-edge (**Figure 34(b)**). This confirms the argument from the previous subsection. In both compositions (BL5FZn20 and BFY20) some oxygen vacancies are present even after the oxidation treatment owing to the aliovalent doping. While the increased oxygen vacancy concentration by reduction does not affect the yttrium environment, this does not hold in the case of zinc. This agrees well with the DFT results [37]. The atomic arrangement Y-$V_O^{\bullet\bullet}$-Fe is energetically disfavoured therefore increasing the oxygen vacancies concentration by reduction does not result in any changes in the local yttrium environment, instead the additional vacancies "cluster" around the iron atoms. For zinc, some differences in the white line are evidenced, since the Zn-$V_O^{\bullet\bullet}$-Fe configuration is more favourable.

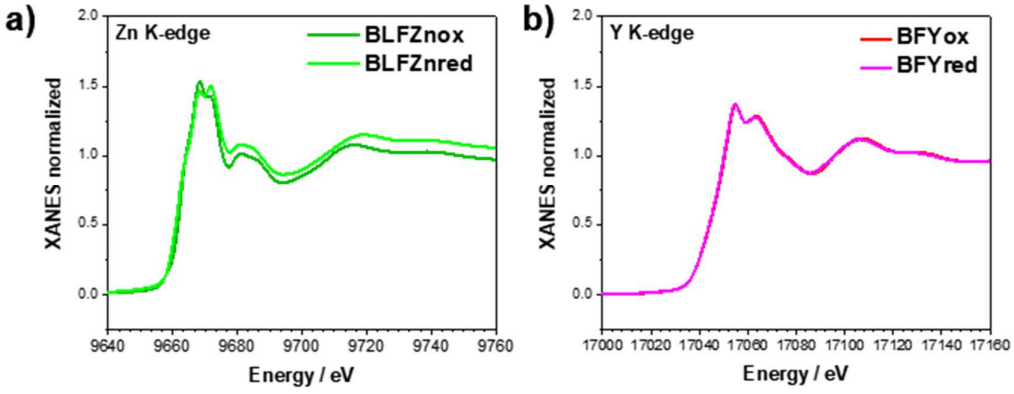


**Figure 34** Zinc *K*-edge of (a) BL5FZn20ox and BL5FZn20red. (b) Yttrium *K*-edge of BFY20ox and BFY20red.

The data measured at the Zn and Y *K*-edge were analyzed as described for the oxygen *K*-edge. In the case of Zn, a *screening* value of 0 and *dilatorb* values of 0.1 and 0.2 were applied for simulating the oxidized and reduced samples. This suggests a slight increase of the orbital overlap. No variations are evident at the Y *K*-edge, where the same values for *screening* and *dilatorb* parameters were used for both oxidized and reduced samples. The value of *screening* 0.1 suggests a retained electronic density on the Y atom, meaning that the yttrium atoms are not strongly participating in the charge transfer with the oxide ions. The simulations are reported in **Figure 35**.

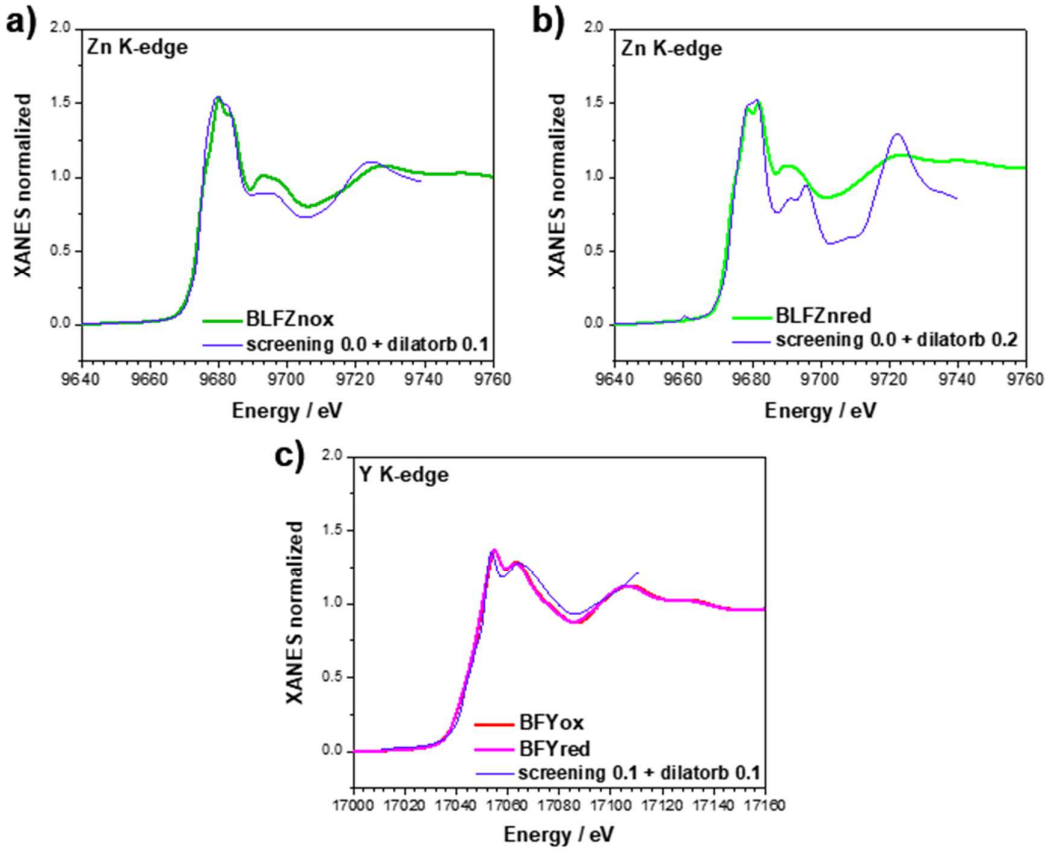


**Figure 35** XANES simulation of (a-b) Zn *K*-edge of BL5FZn20 and (c) Y *K*-edge of BFY20.

### 3.1.4 Relation between proton uptake and electronic structure

The results reported in **Sections 3.1.1-3.1.3** reveal a complex interplay of cation composition, structural distortion and electronic features affecting the proton uptake in (Ba,Sr,La)(Fe,Zn,Y)$O_{3-\delta}$ perovskites. The EXAFS analysis demonstrates that in reduced samples with high oxygen vacancy concentration as well as in samples doped with oversized Zn,Y there is a high degree of disorder in the third coordination shell corresponding to B-O-B buckling. This correlates well with the Fe *K*-edge XANES data, where doped and reduced samples are simulated using a higher amount of "distorted" component (iron in strongly distorted 5-fold coordination), compared to BL5Fox. Moreover, the simulations at the O *K*-edge, show that in reduced and Zn,Y-doped samples the TM*3d*-O*2p* hybridization is less favoured than in BL5Fox. This is reflected in the *screening* and *dilatorb* values used for simulating the experimental spectra.

The B-O-B buckling directly decreases the Fe-O bond covalency because of a less effective *3d-2p* orbitals overlap. This also decreases the hole transfer from the iron to the oxygen, leaving more negative oxide ions with a more basic character. They are more favourable for protons attachment. This helps to understand the proton uptake data reported in **Section 3.1.1**. Zn-doped compositions show a high degree of distortion and the highest proton uptake. An exception is SFZn20, which, as mentioned in **Section 3.1.2**, has a stiffer lattice than its barium rich equivalent, disfavouring the local distortions.

BFY20 differs slightly. The environment of Fe is even more disordered than in BL5FZn20 but BFY20 shows a slightly lower proton uptake than the latter. The DFT calculations [37] show that for this sample Fe-$V_O^{\bullet\bullet}$-Fe atomic arrangement is energetically more favored than Y-$V_O^{\bullet\bullet}$-Fe, and this "clustering" behavior of the vacancies can influence the proton uptake, for example by indirectly creating energetically inequivalent protonation sites as in $BaCe_{1-x}Y_xO_{3-\boldsymbol{\delta}}$ [1].

**Figure 36** summarizes the trends in electronic and geometrical structure found for (Ba,La,Sr)(Fe,Zn,Y)$O_{3-\delta}$ perovskites. The degree of hole delocalization is concluded from EXAFS results (large Fe-O-Fe/M buckling leads to low delocalization) as well as electronic conductivity ($\sigma_{eon}$ in $O_2$ at 600 °C, decreasing from 100 $Scm^{-1}$ for SF [66] to 10 $Scm^{-1}$ for BL5F and ≈1 $Scm^{-1}$ for BFY20 [24].

These consideration on the interplay of chemical, geometrical, and electronic structure features and their effect on the proton uptake are exemplified here for the (Ba,La,Sr)(Fe,Zn,Y)$O_{3-\delta}$ system. It is expected that they can be extended to a larger

group of perovskite compositions, and therefore serve as guidelines for further PCFC cathode material optimization.

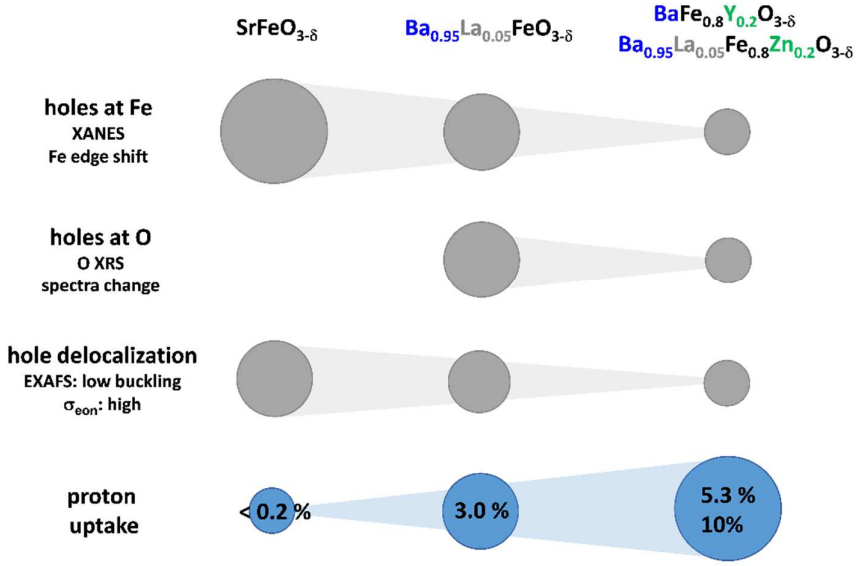


**Figure 36** Schematic summary of the trends in electronic and geometrical structure of (Ba,Sr,La)(Fe,Zn,Y)$O_{3-\delta}$ perovskites, the size of the circles indicates the strength of the effect.

### 3.1.5 Proton diffusivity in selected barium ferrates

The previous **Sections 3.1.1-3.1.4** dealt with the equilibrium proton concentration in barium ferrate perovskites and the effects of dopants on this thermodynamic quantity. In the present section, the proton mobility of selected samples will be explored.

Direct measurements of the proton conductivity in cathode materials with three charge carriers are challenging because of the relatively high concentrations of $h^{\bullet}$ and $V_O^{\bullet\bullet}$. Also Wagner-Hebb measurements are not easy to perform since it is difficult to find a highly proton-selective contact material that can be applied as dense layer. A deposition of *e.g.,* a Ba(Zr,Y)$O_{3-z}$ layer by Pulsed Laser Deposition is not favorable as the required heating of the sample in the vacuum chamber is expected to lead to severe cracking. One possibility explored here for three compositions (BL5F, BL5FZn20 and BFY20) is to measure the transient behavior of the mass relaxation after a $pH_2O$ change under conditions where the process is diffusion limited, *i.e.,* measuring thick and dense samples. The criterion for a process to be diffusion-limited is that the product of surface rate constant $k$ and sample thickness $l$ is larger than the diffusion coefficient [67]. This is fulfilled here because the water surface reaction is fast (it does not require the splitting of a double bond as for $O_2$ incorporation) and mm-thick dense samples can be prepared.

For cathode materials, such sample preparation is not trivial, because of their high and variable oxygen vacancy content, which easily leads to crack formation. Nevertheless, satisfactory samples were obtained using SPS with the parameters included in **Table 1**. This type of measurement has been carried out in ref. [68] for BSFZn20 in the hydrogenation regime (hydrogen uptake from $H_2O$ in high $pO_2$, **Eq. 3**) where the process is determined by the hydrogen chemical diffusion coefficient $D_H^\delta \approx D_{OH_O^\bullet}$. In contrast, here the water uptake ($pH_2O$ is increased from 7.3 mbar to 16.7 mbar) is investigated for samples equilibrated in low $pO_2$ (100 ppm). In this regime the hydration according to **Eq. 2** dominates. Since "dry" is not a well-defined condition ($pH_2O$ is never exactly zero), $pH_2O$ is changed from a lower (7.3 mbar, evaporator at 5 °C) to a higher value (16.7 mbar, evaporator at 18 °C). In this regime of low degree of hydration, the relation $D_{H2O}^\delta \approx D_{OH_O^\bullet}$ is valid [69].

By fitting the normalized mass relaxation using **Eq. 9**, where *f(D, t)* is defined as **Eq. 10**, it is possible to obtain $D_{OH_O^\bullet}$. An example of the fitting procedure is reported in **Figure 37** for BL5F.

**Eq. 9**
$$\frac{\Delta m}{\Delta m_\infty} = 1 - f(D,t)$$

**Eq. 10**
$$f(D,t) = \frac{8}{\pi^2} + \sum_{n=1}^{\infty} (2n+1)^2 \, e^{\frac{-(2n+1)^2 \pi^2 Dt}{4l^2}}$$

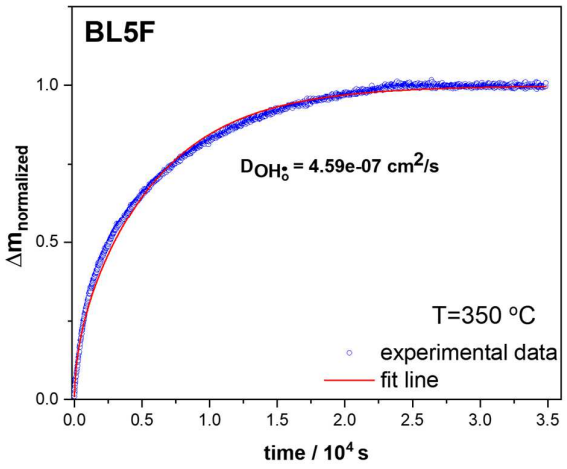


**Figure 37** Example of diffusion coefficient fitting using **Eq. 9** for BL5F at 350 °C, for $pH_2O$ changes from 7.3 mbar to 16.7 mbar in 100 ppm $O_2$. Sample thickness ≈ 1.5 mm.

The fitting for experiments at different temperatures, yields the diffusion coefficients vs inverse of temperature (**Figure 38**), and activation energies for the proton diffusion in BL5F, BL5FZn20, and BFY20 can be extracted.

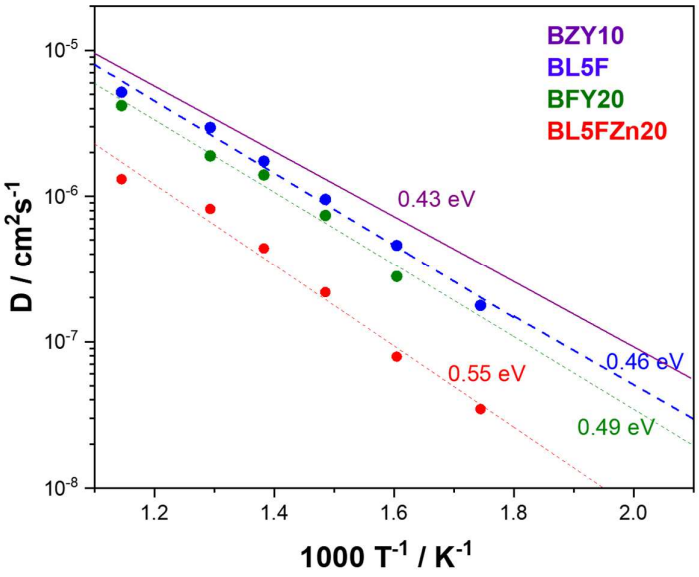


**Figure 38** Proton diffusion coefficients for the cathode materials (BL5F, BL5FZn20, and BFY20) compared to the BZY10 electrolyte material (solid line). The data of the latter are taken from ref. [1]. Activation energies are indicated.

Overall cathode materials show slightly lower proton diffusion coefficients and slightly higher activation energies than the electrolyte BZY10. Nevertheless, they are in the same order of magnitude and the activation energies are reasonable for proton diffusion in a perovskite structure.

The lower values for $D_{OH_O^{\bullet}}$ in the case of BL5FZn20 and BFY20 compared to BL5F can be explained by the fact that the local distortions in the doped sample lead to less favorable angles for the transient O-H bonds, and/or that Zn/Y acceptor behave as proton traps, as it has been found for BZY10 [70]. Also, the lower lattice parameter of barium ferrates compared to BZY10 means stronger repulsion of protons in the transition state to $B^{3+/4+}$.

From these proton diffusivities and the proton concentrations in **Section 3.1.1** and ref. [71], proton conductivities can be calculated. They are shown in **Figure 39**. While the proton diffusivities in **Figure 38** follow a simple Arrhenius behavior, the conductivities show a maximum in the range 400 - 500 °C and then decrease at higher T because of decreasing hydration. The values exceeding ≈ $10^{-4}$ $Scm^{-1}$ would suffice to activate the bulk path of the ORR. It should be considered that these values are obtained from a combination with a separate experiment, so they might carry more uncertainty than the direct measurements as reported for $Ba(Zr,Y,Fe)O_{3-\delta}$ in **Section 3.2.5**.

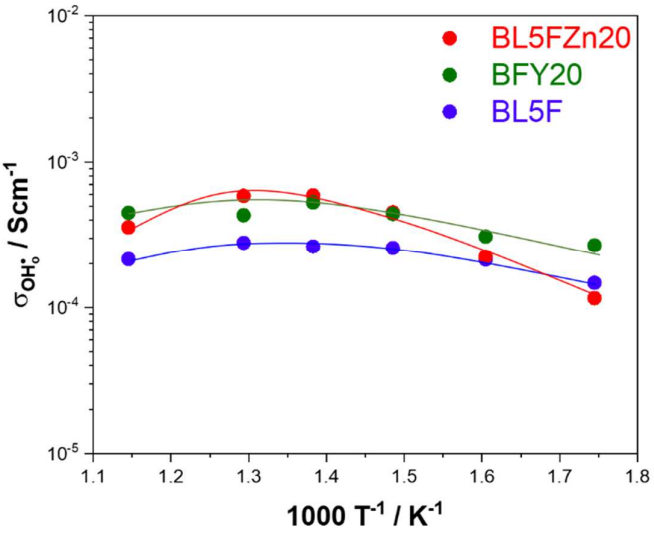


**Figure 39** Proton conductivities of BL5F, BL5FZn20 and BFY20 calculated from the proton diffusion coefficient and concentration. The lines serve as a guide to the eye.

## 3.2 Barium zirconate ferrate solid solution series

In this section, the experimental results on the solid solution $BaZr_{0.88-x}Fe_xY_{0.12}O_{3-\delta}$ are discussed. These systems show the transition from a typical electrolyte material to a typical cathode material. In fact, it was initially hoped that they allow one to combine advantages of the material families [27] (**Figure 40**), but this hypothesis remains to be confirmed. BZYF is a very suitable model system to systematically follow the changes of relevant properties. In order to ensure the possibility for dissociative hydration of $V_O^{\bullet\bullet}$, all samples contain a Y-doping of 12%. The solid solution is analysed here from a thermodynamic, structural and electronic point of view. Moreover, a first direct measurement of proton conductivities for triple conducting oxide is reported.

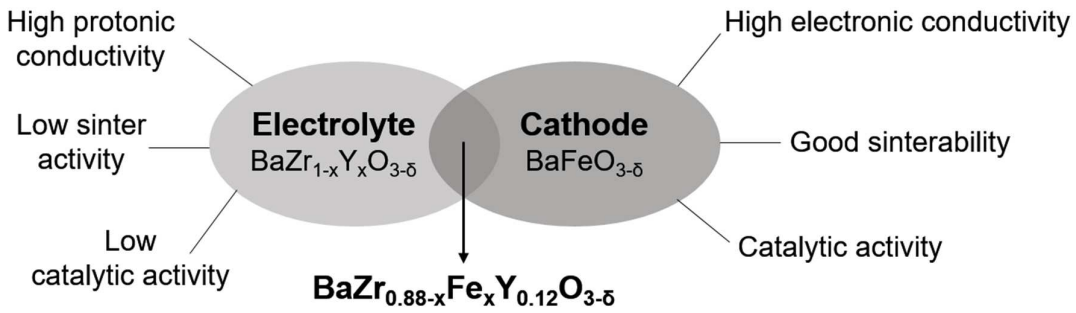


**Figure 40** Advantageous properties brought to the BZYF solid solution from typical cathode and electrolyte compositions.

### 3.2.1 Proton uptake and oxygen stoichiometry

TGA isothermal and dynamic measurements were performed for $BaZr_{0.88-x}Fe_xY_{0.12}O_{3-\delta}$ (x=0, 0.03, 0.06, 0.1, 0.2, 0.3, 0.5, 0.7, 0.8). The full series of van't Hoff plots and proton concentrations is reported in **Appendix A**.

*TGA hydration measurements.* **Figure 41** summarizes the results obtained in the hydration experiments performed according to **Section 2.2.3**. The samples with x = 0 and 0.03 are measured in dynamic mode (cooling from 750°C with 1.5-0.5 $Kmin^{-1}$) in wet $N_2$ ($pH_2O$ = 16.7 mbar) given their high hygroscopicity, which makes it difficult to return to the comparably dehydrated state at lower temperatures.

From **Figure 41(a)** it is clear that the proton concentration decreases steeply by increasing the iron content in the solid solution up to an iron concentration of 20% (with respect to the B-site). By further increasing the iron content (x>0.3), the proton concentration slowly increases again and reaches a plateau for very high Fe (x>0.5). A

similar trend is recognizable for the degree of hydration (**Figure 41(b)**), where already 10% of Fe causes a decrease by an order of magnitude. This proves again the strongly different hydration behavior of cathode and electrolyte materials. Going back to **Figure 41(a)**, it is worth mentioning that the proton concentration of BZYF80 is essentially the same as for BFY20, both compositions have, in fact, 80% of iron in the B-site. BL5F is not following the trend (its proton uptake is much lower with respect to the BZYF's and BFY20) for the reasons provided in **Section 3.1** (strong covalency of Fe-O bonds in absence of distortion). **Figure 42** reports exemplary graphs of the proton concentration and the van't Hoff plot, the compositions not included here can be found in **Appendix A**. **Table 8** compiles the standard enthalpy and entropy of hydration extracted from the van't Hoff's plots of the solid solution series.

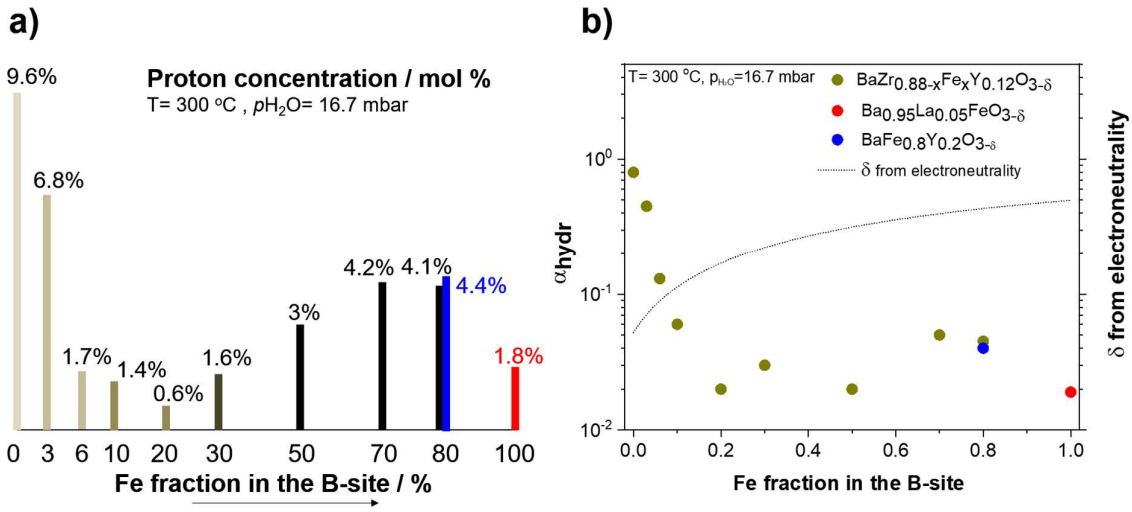


**Figure 41** (a) Proton concentration of $BaZr_{0.88-x}Fe_xY_{0.12}O_{3-\delta}$, (b) degree of hydration α as a function of the iron content in the B-site, at 300 °C in 16.7 mbar of $pH_2O$. The degree of hydration is calculated using **Eq. 6** with δ from the electroneutrality condition (**Eq. 5**). BFY20 (80% of Fe and no Zr, blue) and BL5F (just iron in the B-site, red) are included for comparison.

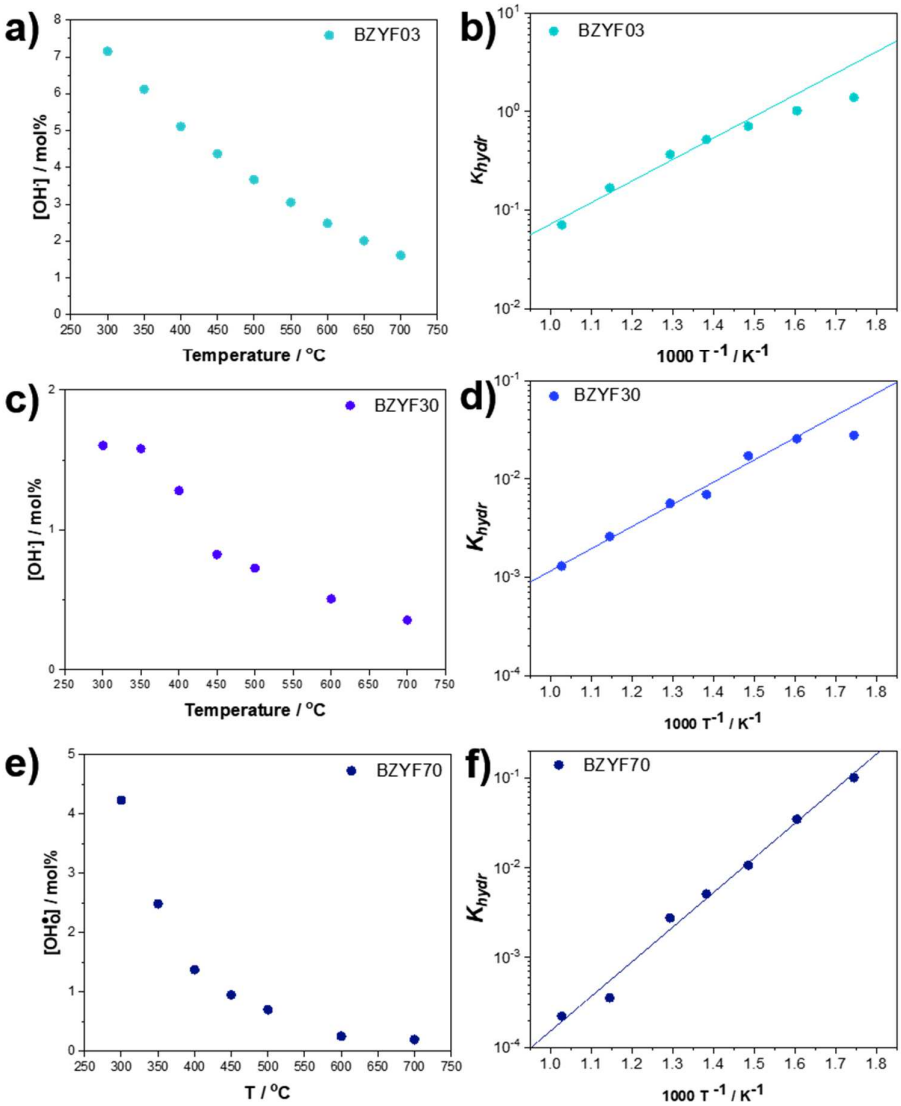


**Figure 42** Proton concentration vs temperature and van't Hoff plots of BZYF03 (a-b), BZYF30 (c-d) and BZYF70 (e-f). Regression lines are indicated.

**Figure 43** includes the BZYF solid solution thermodynamic data in the set of data for the related perovskites already shown in **Figure 9**. It is clearly visible how the low-iron compositions fill the gap between the electrolyte and cathode regimes. The transition behaviour of the hydration thermodynamics by varying the amount of iron is highlighted by the blue shade. For these samples $\Delta S^o_{hydr}$ remains in the range of -80 to -100 Jmol$^{-1}$K$^{-1}$ which is typical for Ba(Zr,Y)O$_{3-z}$ electrolytes, and the less negative $\Delta G^o_{hydr}$ is caused mainly by the $\Delta H^o_{hydr}$ decreasing from -80 kJmol$^{-1}$ to -31 kJmol$^{-1}$. When more iron is introduced, the materials start to behave similar to other cathode materials. From F20

to F70 the hydration enthalpy becomes more negative again (more and more $Zr^{4+}$ is replaced by the less charged $Fe^{3+}$) but in parallel also $\Delta S^o_{hydr}$ becomes more negative, such that the overall $\Delta G^o_{hydr}$ remains positive at about +30 kJmol$^{-1}$. The reasons for the more negative $\Delta S^o_{hydr}$ are being investigated by P. Rosander (University of Goeteborg) using DFT phonon calculations (to be published).

**Table 8** Summary of the hydration thermodynamic parameters for the BZYF solid solution series, calculated from the respective van't Hoff plots (samples with frozen-in oxygenation reaction; all iron in 3+ state). BZY10 data are from Ref. [1].

| samples | $\Delta H^o_{hydr}$ / kJmol$^{-1}$ | $\Delta S^o_{hydr}$ / JK$^{-1}$mol$^{-1}$ | $\Delta G^o_{hydr}$ / kJmol$^{-1}$ (700 K) |
|---|---|---|---|
| **BZY10** | -80 | -89 | -18 |
| **BZYF0** | -78 ± 4 | -94 ± 5 | -12 ± 2 |
| **BZYF03** | -66 ± 3 | -90 ± 4 | -3 ± 1 |
| **BZYF06** | -49 ± 11 | -83 ± 13 | 10 ± 1 |
| **BZYF10** | -31 ± 6 | -74 ± 7 | 21 ± 2 |
| **BZYF20** | -32 ± 8 | -84 ± 10 | 27 ± 2 |
| **BZYF30** | -38 ± 3 | -93 ± 5 | 27 ± 2 |
| **BZYF50** | -59 ± 2 | -126 ± 3 | 30 ± 1 |
| **BZYF70** | -74 ± 4 | -147 ± 5 | 29 ± 2 |
| **BZYF80** | -71 ± 4 | -144 ± 6 | 30 ± 4 |

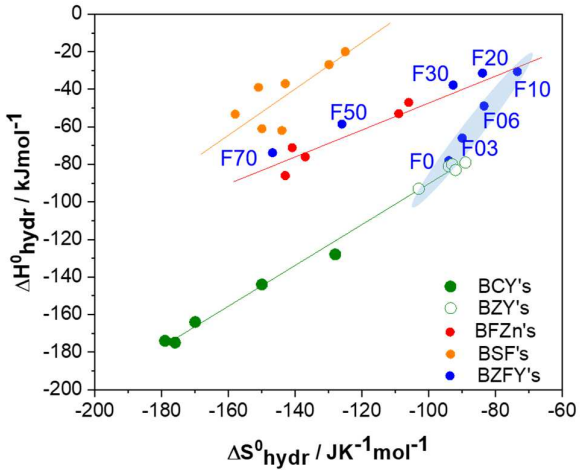


**Figure 43** Plot of $\Delta H^o_{hydr}$ vs $\Delta S^o_{hydr}$ of materials: $SrFeO_{3-\delta}$, $(Ba,Sr)FeO_{3-\delta}$ (BSF), $Ba(Fe,Y,Zn)O_{3-\delta}$ (BFZn), $Ba(Zr,Y)O_{3-\delta}$ (BZY), $Ba(Ce,Y)O_{3-\delta}$ (BCY) and $Ba(Zr,Y,Fe)O_{3-\delta}$ (BZFY). The data in blue refer to the BZFY solid solution where the amount of iron is indicated by the number. BCY and BZY data from Ref. [1].

*TGA oxygen non-stoichiometry measurements.* **Figure 44** and **Figure 45** summarize the results obtained in the oxygen non-stoichiometry experiments performed according to **Section 2.2.3** (dynamic mode).

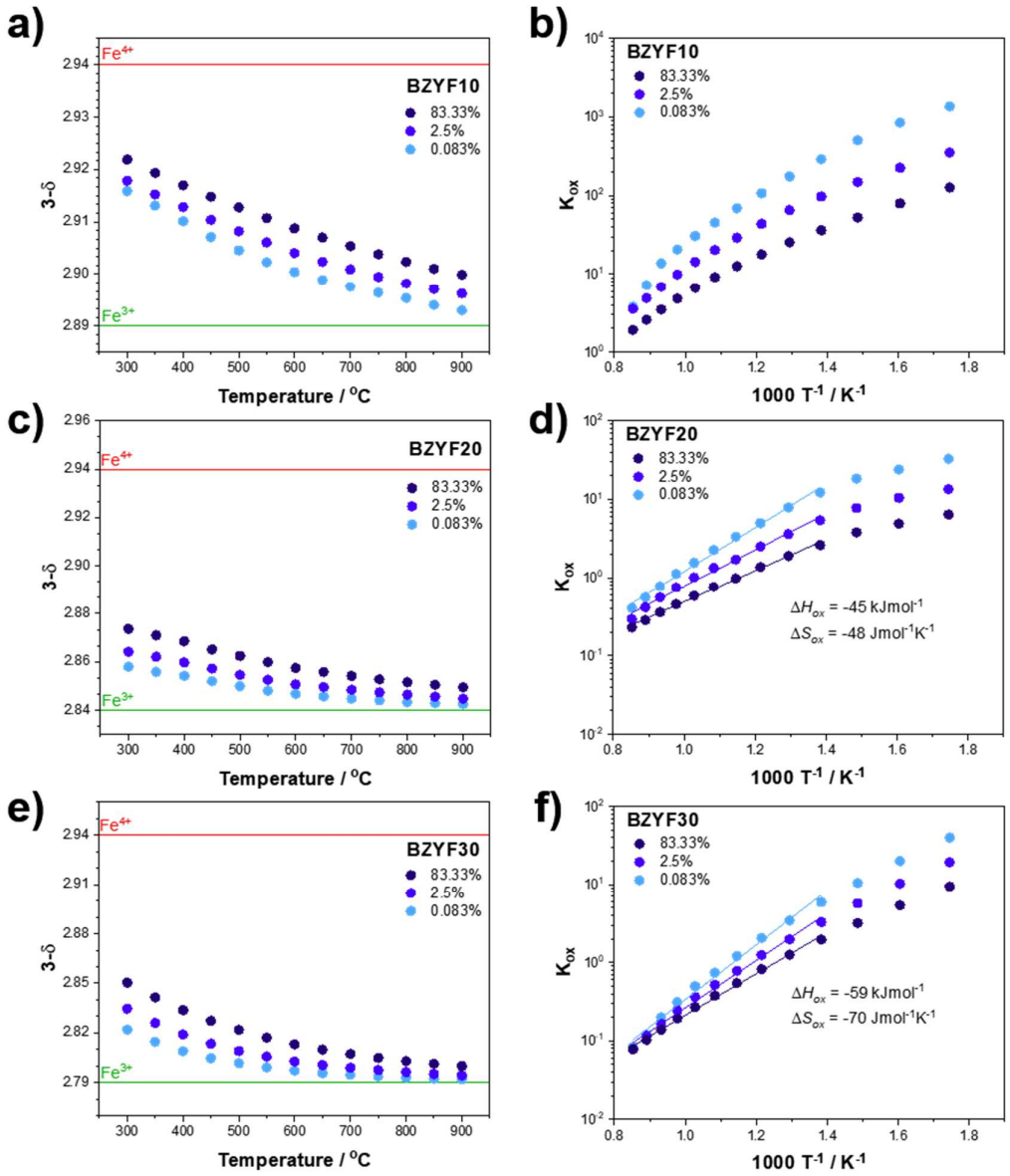


**Figure 44** Oxygen stoichiometry 3-δ and Van't Hoff plots for $K_{ox}$ of BZYF10 (a-b), BZYF20 (c-d) and BZYF30 (e-f). The reported values of $\Delta H^{o}_{ox}$ and $\Delta S^{o}_{ox}$ are calculated by averaging the obtained values for each $pO_2$.

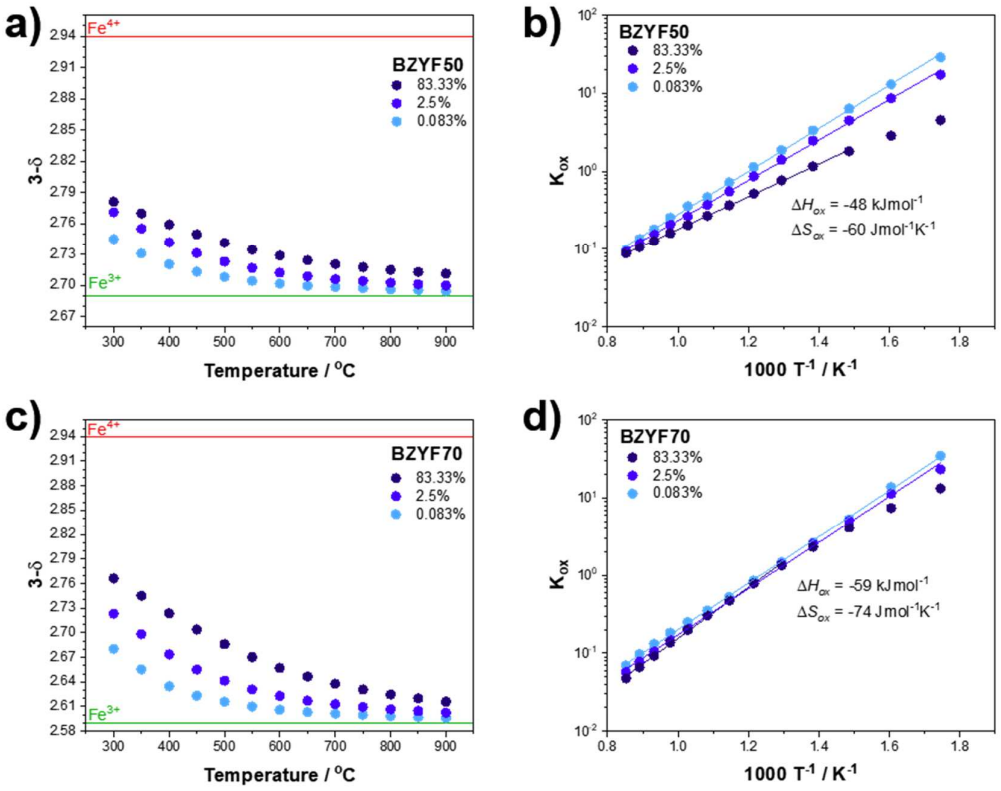


**Figure 45** Oxygen non-stoichiometry 3-δ and Van't Hoff plots for the $K_{ox}$ of BZYF50 (a-b), BZYF70 (c-d). The reported value of $\Delta H^{o}_{ox}$ and $\Delta S^{o}_{ox}$ are calculated by averaging the obtained values for each $pO_2$.

The more or less pronounced non-linearity in the van't Hoff plots of **Figure 44**, and the different values of $K_{ox}$ at different $pO_2$ indicate that for intermediate Fe-content these systems are not following an ideally dilute behaviour. It is already known for redox-active perovskites that at low T (where the hole concentration increases) a non-negligible hole-hole interaction gives rise to the bending in the van't Hoff plots [72-73]. Interestingly, the loss of linearity is more pronounced for intermediate-iron content (20-50%). The oxygen non-stoichiometry measurements are performed on nominally dry samples, but for intrinsically highly hygroscopic compositions this is may lead to spurious weight increase due to water incorporation caused by $H_2O$ traces in nominally dry gas. For F10, the δ values are thus overestimated (*i.e.,* the weight change can be ascribed to the uptake of $O_2$ and $H_2O$), and this effect predominates in low T where the hydration is more favourable. At high temperatures the major uncertainty comes instead from the

absolute stoichiometry determination (only small weight changes upon $pO_2$ change). For the aforementioned reasons no value of $\Delta H_{ox}^{o}$ *and* $\Delta S_{ox}^{o}$ are reported for F10.

When effects of hole delocalization are observed in the oxygen stoichiometry measurements, they are expected to affect also the hydration behaviour. Thus the observation of hole-hole interactions here for Fe-doped samples is in good agreement with the steep decrease of proton uptake in **Section 3.2.1**.

### 3.2.2 Impurity band formation

UV-Vis measurements in diffuse reflectance mode are performed for the solid solution series as described in **Section 2.2.6**. In **Figure 46(a)** the spectra of an oxidized sample (F06ox) and reduced (F10red) are plotted together: in F06ox a peak caused by $Fe^{4+}$ states is visible at ≈ 3.3 eV, while in F10red the $Fe^{3+}$ states are indicated by the vertical line at ≈ 3.9 eV. **Figure 46(b)** reports the spectra of selected oxidized samples. It demonstrates that for high iron content an impurity band of partially occupied Fe*3d* states forms below ≈3 eV. A similar behavior was observed for $SrTi_{1-x}Fe_xO_{3-\delta}$ in ref. [74]. The presence of the impurity band will influence the electronic conductivity in the material, leading to the percolation phenomena discussed in the following **Section 3.2.3**.

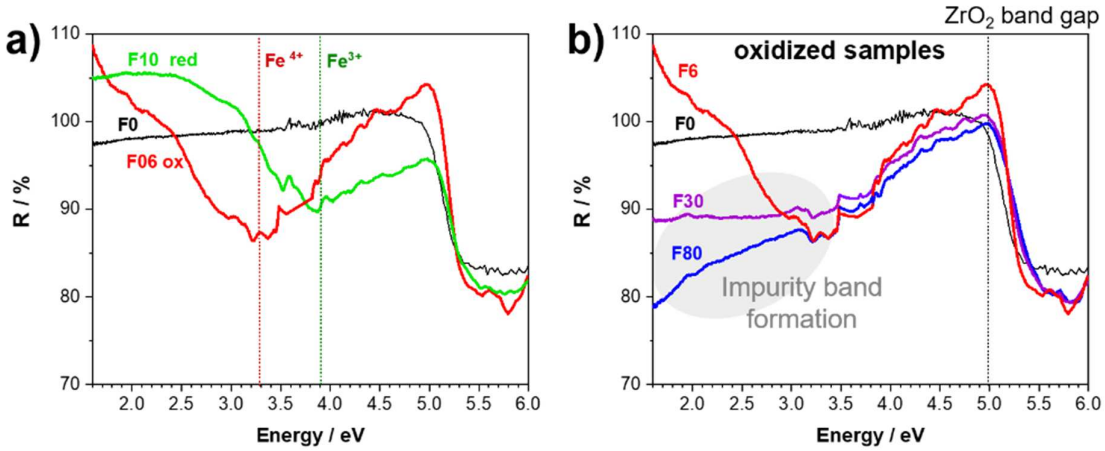


**Figure 46** UV-Vis reflectance spectra. (a) in the oxidized sample (F06ox) the $Fe^{4+}$ states are highlighted by the vertical red line, in the reduced sample (F10red) the $Fe^{3+}$ states are visible. The iron-free sample (F0) is also reported. (b) Exemplary spectra of oxidized samples with low iron (F06) and high-iron (F30, F80) content. The impurity band formation is indicated by the grey shade.

### 3.2.3 Percolation effect on $\sigma_{eon}$

Percolation phenomena and its effects on conductivity are well known and exploited in different applications such as resistors, sensors, etc. [75-78]. The majority of studies pertaining to electronic percolation focus on composite materials [75, 78], while percolation in single-phase materials is less studied. In this context, solid solutions are the perfect model systems for showing the percolation occurrence in single-phase materials. Regarding cubic perovskites, one can find studies of electronic percolation in $BaZr_{1-x}Fe_xO_{3-\delta}$ [79], $BaZr_{1-x}Co_xO_{3-\delta}$ [80], $SrTi_{1-x}Fe_xO_{3-\delta}$ [74, 81], $SrTi_{1-x}Co_xO_{3-\delta}$ [82]. Also solid solutions with other structures can exhibit a percolation behavior, as reported for fluorites [83], inverse spinel [84] and oxides with rock-salt structure [85-86]. The electronic percolation is evidenced by a sharp rise in conductivity when the percolation threshold, which corresponds to a certain critical concentration, is surpassed. The critical threshold is usually indicated as $p_c$. In a simple cubic random percolation model, which can to a first approximation be applied to our cubic perovskites, its value is 0.2488 [76]. Anyhow, this discrete number should be regarded with caution, and it will be more correct to describe it as a "critical region" since slight variation from this value can be caused by the local and electronic structure of the materials.

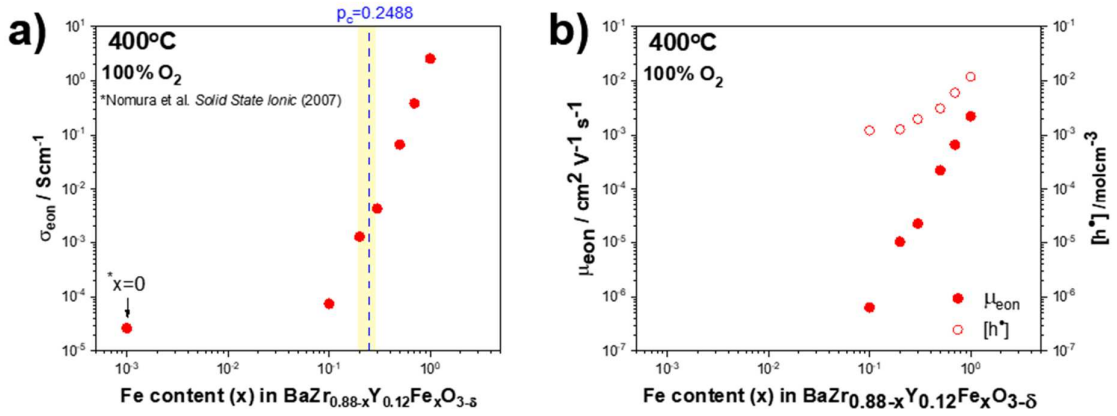


**Figure 47** (a) $\sigma_{eon}$ (b) $\mu_{eon}$ and $[h^{\bullet}]$ as a function of the iron content in BZYF the solid solution. In panel(a) the yellow shade indicates the critical percolation region.

The electronic percolation effect in the solid solution $BaZr_{0.88-x}Y_{0.12}Fe_xO_{3-\delta}$ is presented in **Figure 47**.

The EIS data are collected in 100% $O_2$ with the experimental setup described in **Section 2.2.7.1**. The data point at x=0 (**Figure 47(a)**) refers to $BaZr_{0.8}Y_{0.2}O_{3-\delta}$ extrapolated to 400 °C from Ref. [87]. No data are reported for x = 0.01, 0.03 and 0.06, in fact these compositions are essentially proton conductors, and it was not possible to identify the minor electronic conductivity beneath the dominating protonic contribution. Depending on the iron concentration the hole polaron hopping occurs via different paths. In the simplest model one could say that for low iron content the hole hopping is mainly occurring via $ZrO_6$ octahedra, but the holes have to be de-trapped from the Fe centers. For the $BaZr_{1-x}Fe_xO_{3-\delta}$ series, this detrapping energy was estimated to be 1.2 eV [79]. For intermediate iron content there will be a path with mixed $ZrO_6$ and some $FeO_6$; for the iron concentration exceeding the critical percolation region the $FeO_6$ path will dominate, which is free of de-trapping events, and correspondingly the average mobility and activation energy change. This model does not take into account the presence of oxygen vacancies (increasing by increasing the iron content), which in reality will act as an additional obstacle in the conduction path. **Figure 47(b)** shows that while the hole mobility steeply increases by increasing the amount of iron, the variation of the hole concentration is much smaller. This is a further indirect evidence of the percolation phenomena. In fact, the migration barrier for hole hopping in a $FeO_6$ matrix (≈0-0.3 eV) is smaller than the one observed for a $ZrO_6$ matrix (≈0.4-0.6) [79], which for the first case results in an increased mobility.

### 3.2.4 Effects of iron content on local and electronic structure

Similarly as for the samples reported in **Section 3.1**, XAS and XRS spectra were acquired for selected compositions of the BZYF solid solution series. For these samples the results are included here on a qualitative level. As for $(Ba,La)(Fe,Zn,Y)O_{3-\delta}$, the Fe *K*-edge XANES in **Figure 48** demonstrates that the iron is closer to a formal 3+ oxidation state even for oxidized samples (that formally have $Fe^{4+}$). This is ascribed to the same explanation discussed in **Section 3.1.3**: a partial hole transfer from $Fe^{4+}$ to the adjacent $O^{2-}$. Also here this hypothesis is supported by the O *K*-edge spectra in **Figure 49**, where for the iron-rich samples an additional feature appears at ≈528 eV, which represents the hybridization of Fe*3d*-O*2p* orbitals. It is expected to be more intense when the charge transfer is larger, and also depends on the average number of iron atoms around each oxygen. Therefore, the absence of this feature for F06ox does not necessarily means that there is no charge transfer, but rather that the Fe-content is too low to be

detected in the O *K*-edge. However, it suffices to notice that even for F06ox the iron is closer to the 3+ reference in the Fe *K*-edge XANES.

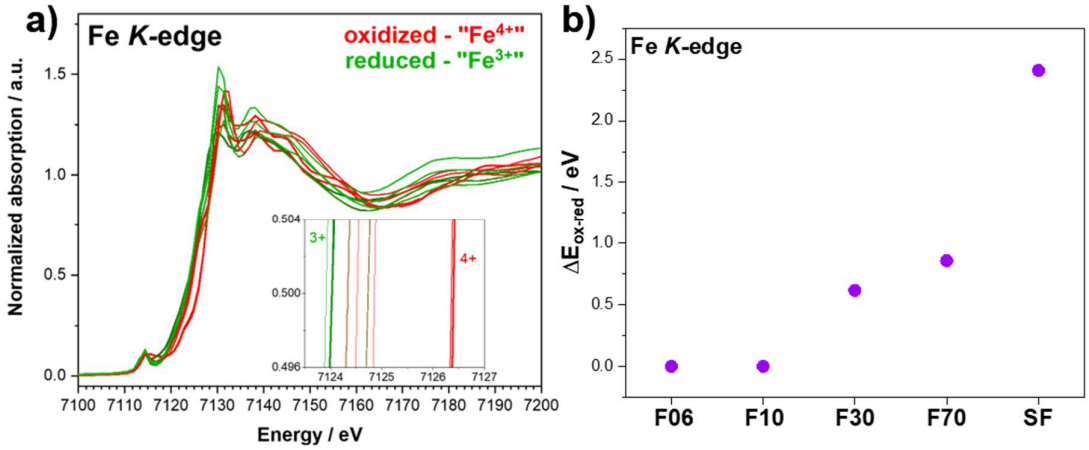


**Figure 48** (a) Fe *K*-edge XANES of all BZYF samples. Oxidized samples are indicated in red, reduced in green. The inset is a magnification of the half-height of the edge, where the references for $Fe^{4+}$ ($SrFeO_3$) and $Fe^{3+}$ ($SrFeO_{2.5}$) are given as bold lines. (b) Difference of edge position $\Delta E_{ox\text{-}red}$ (at half-height of the main Fe *K*-edge).

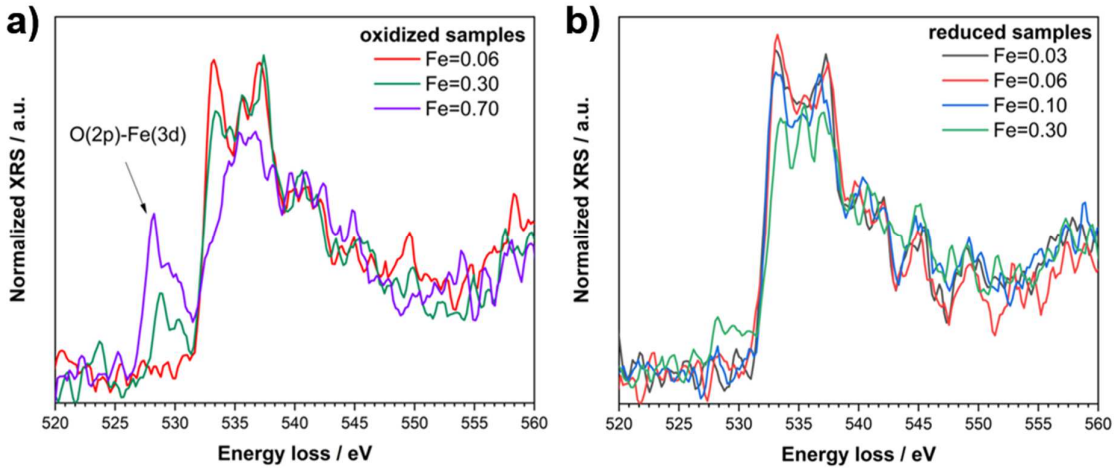


**Figure 49** O *K*-edge from XRS of oxidized samples (a) and reduced samples (b). The Fe*3d*-O*2p* orbital hybridization is indicated by an arrow.

Also for this series of samples, the local structure was resolved using the EXAFS part of the XAS. **Figure 50** reports the Fourier Transforms for all investigated samples at three different edges: Fe, Y, Zr *K*-edges.

Up to 10% of iron no significant modification of the B-site cation local environment is detected. For F30, the iron (and, to less degree the yttrium) local environment starts to become disordered upon reduction. This is evidenced by the signal suppression and broadening in the third shell (3-4.5 Å), suggesting a Fe-O-Fe buckling induced by the combination of B-site cation mismatch ($Fe^{3+}$ is smaller than $Zr^{4+}$ and $Y^{3+}$) and the increased oxygen vacancy concentration. This effect is even more severe for the sample with 70% of iron, where also the zirconium and yttrium third shells are impacted, which probably leads also to additional buckling of the Y(Zr)-O-Y(Zr) and Y(Zr)-O-Fe arrangements.

There is another interesting observation regarding the first shells. The area of Y-O and Zr-O peak in F30 and F70 do not change upon reduction, meaning that by introducing oxygen vacancies the yttrium and zirconium coordination number does not decrease as it would be expected from a random vacancy distribution model. This is different for Fe-O, where the first shell systematically decreases upon reduction, indicating a change of the iron coordination number. This effect is stronger for higher oxygen vacancy concentration, meaning that it is more visible in F70 than F30. This behaviour resembles the situation reported for BFY20 in **Section 3.1** where DFT calculations and XRS simulations indicate that the Fe-$V_O^{\bullet\bullet}$-Fe arrangement is energetically more favoured than the Y-$V_O^{\bullet\bullet}$-Fe one.

Summarizing, below 10% of iron doping the cations local environments are not impacted while for heavily iron-doped samples the buckling of the B-O-B connections starts to appear. It has been extensively described in **Section 3.1.3** how the buckling affects directly the electronic structure, and how this modifies the proton uptake avoiding the decreased oxygen ion basicity.

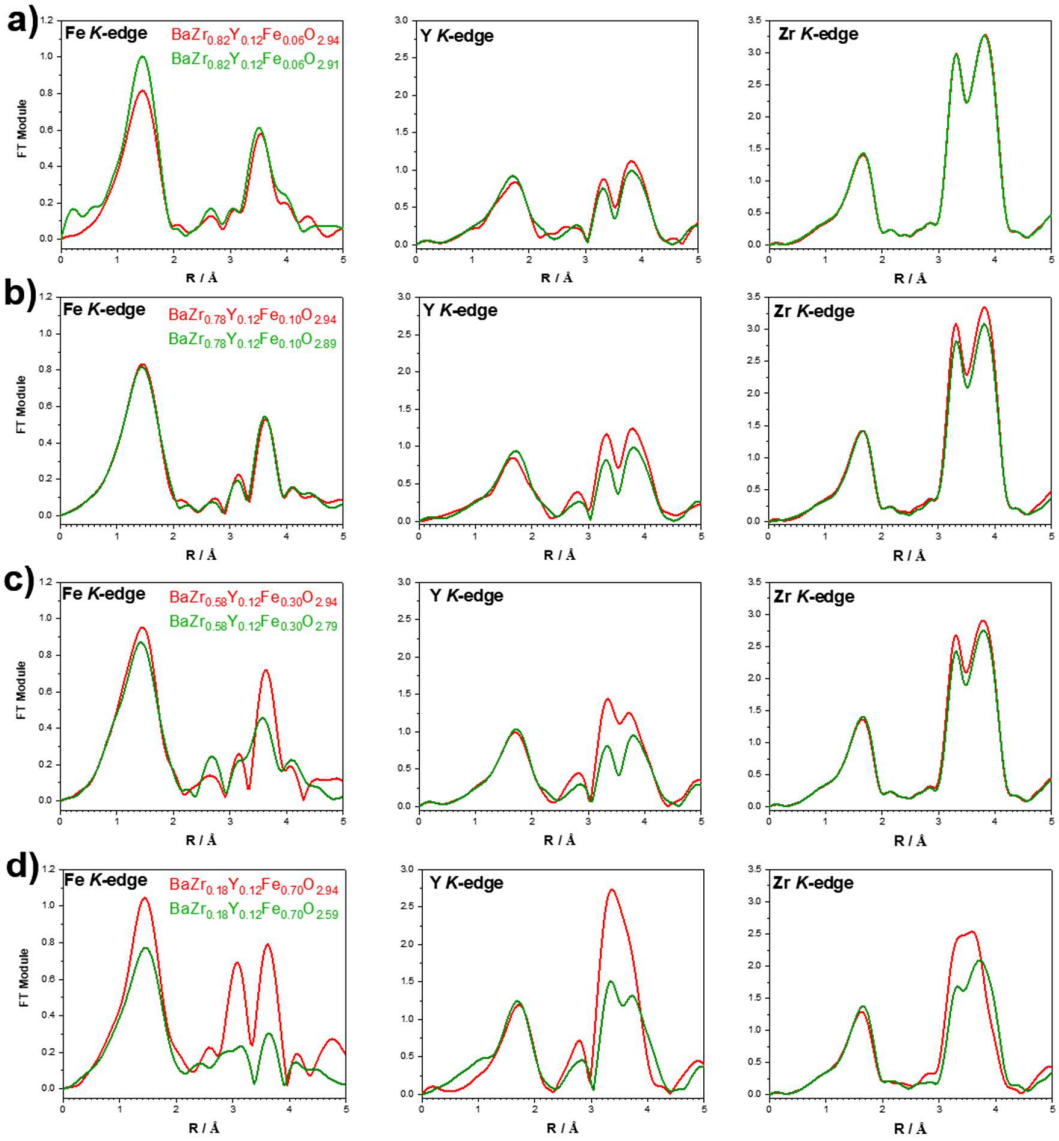


**Figure 50** Fourier transforms at Fe, Y and Zr *K*-edges of (a) F06, (b) F10, (c) F30 and (d) F70. red=oxidized samples ("$Fe^{4+}$"), green= reduced samples ("$Fe^{3+}$"). The mismatch between ox and red in the first shell of F06 is due to the difficult data extraction (data collected in fluorescence, relatively noisy signal).

### 3.2.5 Effects of iron content on partial conductivities

As anticipated in **Section 3.1.5**, it is not trivial to separate the partial contributions of protons, oxygen vacancies, and holes to the total conductivity in triple conducting oxides. This is essentially due to the high concentration and mobility of electron hole in these materials and the difficulty in suppressing the electronic conduction. Under oxidizing conditions, the electronic conductivity is several orders of magnitude higher than the proton and oxygen vacancy conductivities.

A possible way for overcoming the problem is to perform EIS over an extended and controlled $pO_2$ range such that the ionic regime expected between $10^{-10}$-$10^{-20}$ bar of oxygen can be probed. This can be done by coupling the measurement cell with an oxygen pump as described in **Section 2.2.7.1**. The equilibrium partial conductivities of the charge carriers show a different dependence on $pO_2$, in accordance with the Brouwer diagrams [88]. For the mixed conductors subject of this thesis, the partial conductivities dependence with $pO_2$ will be approximately ¼ for electron hole ($Fe^{3+}$ oxidizes to $Fe^{4+}$), -¼ for excess electrons ($Fe^{3+}$ reduces to $Fe^{2+}$). Iron acquires the 3+ oxidation state over an extended $pO_2$ range [89], and within this plateau the protonic and $V_O^{\bullet\bullet}$ conductivity is expected to be $pO_2$ independent. In the ideal case, the electron holes are the dominant charge carriers for $1 < pO_2 < 10^{-5}$ bar, the electrons for *ca.* $pO_2 < 10^{-18}$ bar, and the protons and the oxygen vacancies in the intermediate $pO_2$ range. Regarding the latter, the oxygen vacancies will dominate the conductivity in dry gas, the protons under humid conditions. Therefore, in the Brouwer diagrams of the investigated compositions it is possible to recognize four different regions dominated by a specific charge carrier. Here, each sample will be treated separately, and the last paragraph will give a summarizing discussion.

Given the non-linear response of the oxygen pump in the high intermediate $pO_2$ (even if a buffer gas is fed into the cell) some data are slightly shifted on the $pO_2$ axis by interpolating the estimated correct value of oxygen partial pressure from the previous stable data point at 350 °C (where the pump signal is more reliable). While generally the data are acquired under equilibrated condition, this is not so in the case of 100 ppm $O_2$ where the very slow oxygen kinetics does not allow one to reach the equilibration in a reasonable time (it would take weeks).

*Electrical conductivity of F10.* **Figure 51** shows the Brouwer diagram and the Arrhenius plot of electrical conductivity. **Figure 51(a)** confirms that it was possible to separate the contribution of the holes and protons in the materials. A significant variation of $\sigma_{eon}$ at high $pO_2$, and a very broad protonic plateau from *ca.* $pO_2 < 10^{-7}$ bar can clearly be

recognized. The latter is confirmed also by the activation energy (0.39 eV) which is very similar to the one reported by Kreuer [1] for BZY10 (0.43 eV) in absence of iron. One would tend to assign the plateau under dry condition (full circles, from *ca.* $pO_2 < 10^{-7}$ bar) to oxygen vacancy conduction, but the activation energy in that region (0.46 eV) is very close to the one of protons, suggesting that the vacancies could still be partially hydrated. This would not be surprising considering the high degree of hydration of F10. Moreover, if one calculates the activation energy for the dry data point at $pO_2 \approx 10^{-23}$ bar, the value will be 0.7 eV, which is much closer to the one reported by Schober et al. [90]. Therefore, it is reasonable to hypothesize that the true oxygen vacancy plateau is starting at lower $pO_2$, where larger pumping currents are more and more eliminating even traces of water from the gas flow. For F10 it was not possible to reach the region in which the *n*-type charge carrier predominate. The reason is the low *n*-type carrier concentration and their low mobility, since similarly as in the electron hole case, one could expect a percolation phenomenon only from [Fe]>0.1. Indeed an *n*-branch is present for higher iron content.

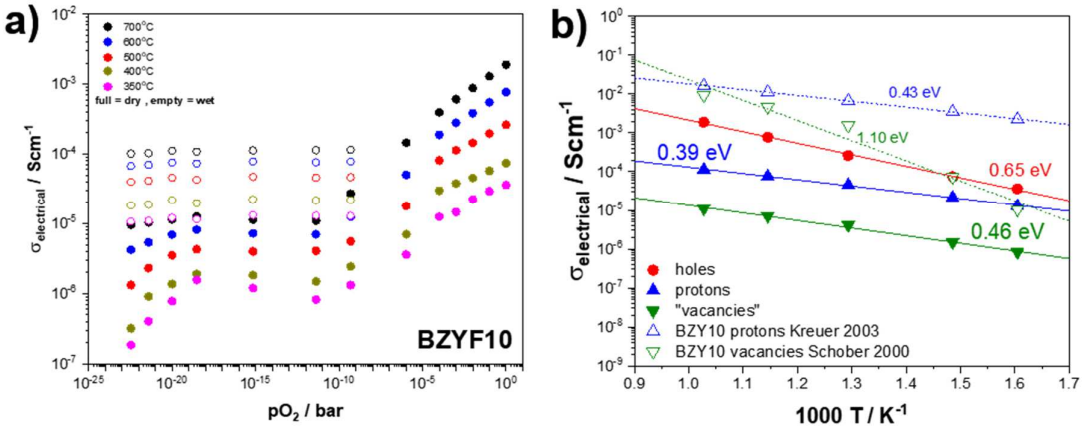


**Figure 51 (a)** Brouwer diagram, (b) Arrhenius plot of conductivities of F10. In panel(b) the activation energies calculated from the Arrhenius plots are given. Data for the proton and oxygen vacancy conductivities of BZY10 from Refs. [1, 90] are also included.

*Electrical conductivity of F20.* **Figure 52** shows the Brouwer diagram and the Arrhenius plot of F20. For the protonic plateau, the same considerations as for F10 hold. In contrast to F10, it is possible for F20 to identify also the ionic plateau for the oxygen vacancies (the hygroscopicity of F20 is lower than for F10, *cf.,* **Figure 41**). This is confirmed by the activation energies in **Figure 52(b)** where the oxygen vacancy conductivity has a

value of 0.77 eV. The activation energy calculated for protons is 0.46 eV, close to the one reported for BZY10. Moreover, the activation energy for the electron hole conductivity is smaller than in F10, as expected from the electronic percolation behavior explained in **Section 3.2.3**. Interestingly in the case of F20 it is also possible to start to see the *n*-branch at very low $pO_2$.

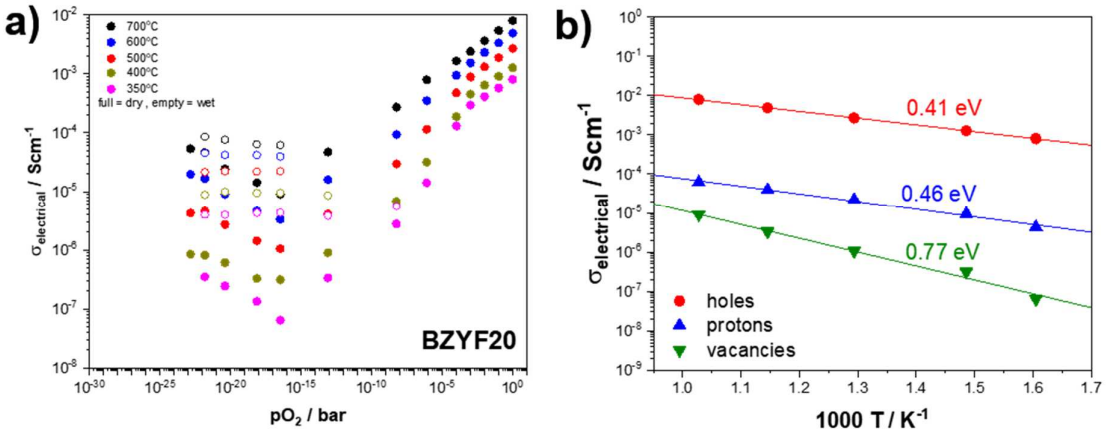


**Figure 52** (a) Brouwer diagram, (b) Arrhenius plot of F20. In panel(b) the activation energies are also reported.

*Electrical conductivity of F30.* With increasing amount of iron in the solid solution, it becomes more complicated to separate the contributions of the different charge carriers, especially for the protons. Therefore, for Fe-content ≥ 0.3 the conductivity is measured also at lower temperatures (250-350 °C) in the intermediate $pO_2$ region in wet and dry conditions. At lower T the hydration becomes more favored, which can allow discriminating the contribution from protons to the total conductivity, calculating it as the difference between wet and dry. The Brouwer diagram in **Figure 53(a)** again displays the *p*-branch, two ionic plateaus and the beginning of the *n*-branch. While the calculated activation energies (**Figure 53(b)**) for the electron holes and the oxygen vacancies are close to their expected values, the one calculated for protons is higher than expected. The calculated activation energy in the temperature range 250-300 °C (solid regression line) is 0.69 eV. Considering that the data at lower temperatures carry higher uncertainties (given the noise of the signal coming from the very high resistances ≈100 MΩ this is not too surprising), and the activation energy for protons has to be regarded with a certain caution. A comparable behavior is also observed for F50, this is in line with their similar degrees of hydration. A possible explanation for the relatively high

activation energy for protons could also be the proton trapping exerted by the iron centers (that in the case of F50 could be compensated by other effects). These effects are considered in more detail in **Figure 57**.

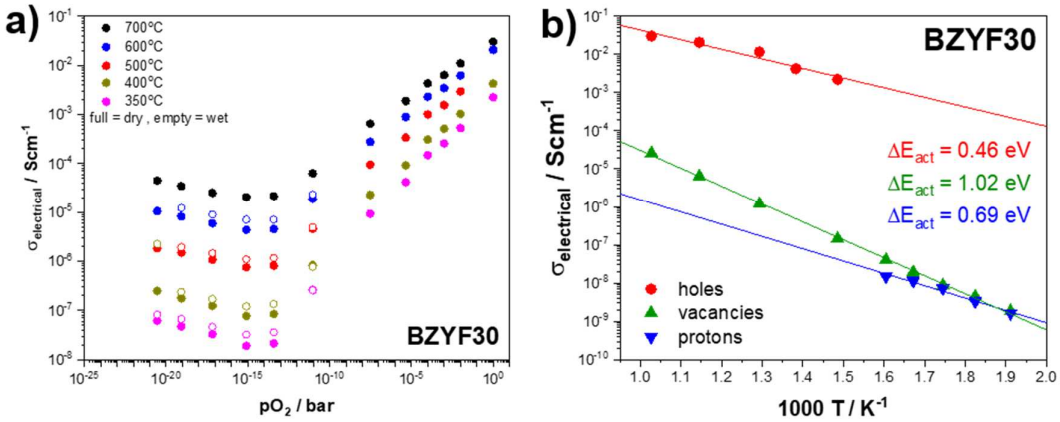


**Figure 53** (a) Brouwer diagram, (b) Arrhenius plot F30. In panel(a), the measured lower temperatures are not displayed for the sake of simplicity. In panel(b) the activation energies are given.

*Electrical conductivity of F50.* **Figure 54** shows the Brouwer diagram and Arrhenius plot. The Brouwer diagram yields the electronic branches (here the *n*-branch becomes more visible) and the ionic plateaus. The protonic and oxygen vacancy conductivities differ less than in F30, and the activation energy for protons it is higher than expected (0.75 eV). The electronic conductivity shows a smaller activation energy, in accordance to the percolation behavior described in **Section 3.2.3**.

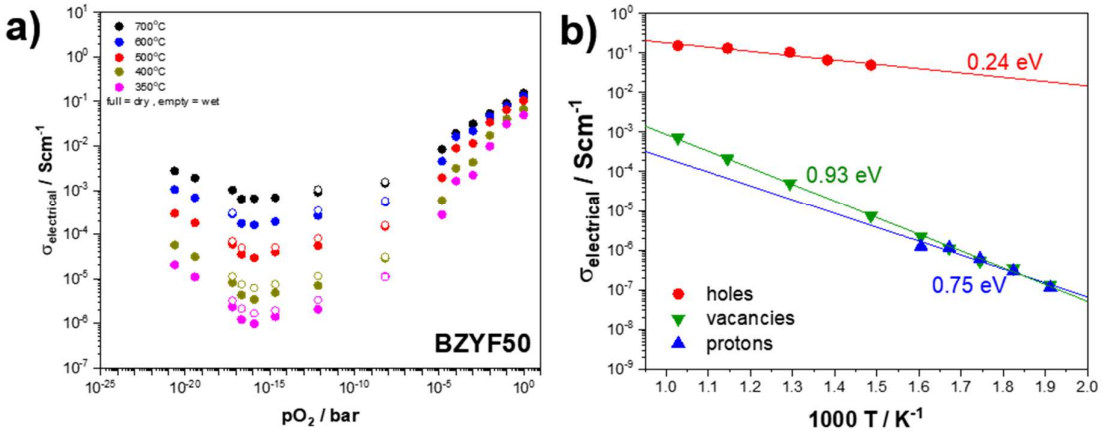


**Figure 54** (a) Brouwer diagram, (b) Arrhenius plot of F50. In panel(a) the measured lower temperatures are not given for the sake of simplicity. In panel(b) the activation energies are indicated.

*Electrical conductivity of F70.* The Brouwer diagram in **Figure 55(a)** shows that the conductivities in dry and wet in the ionic plateaus differ less than in F50, as expected from increasing the iron content. The activation energy of proton conductivity is lower (0.5 eV). This could be related to its higher degree of hydration (rather closer to F10 than F30 or F50) which favors protons conduction. The activation energy for the oxygen vacancies is significantly higher than the one reported for the protons (this was not the case for F10), suggesting that in dry atmosphere the oxygen vacancies are not hydrated.

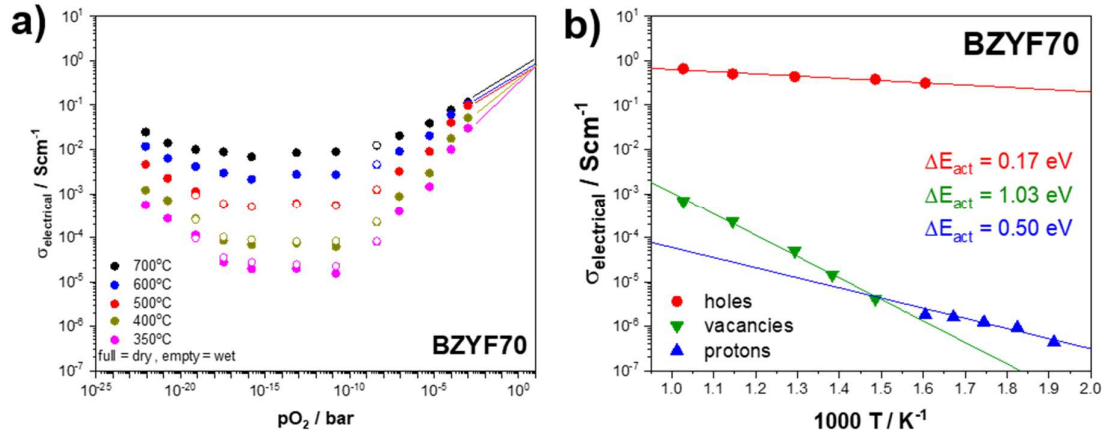


**Figure 55** (a) Brouwer diagram, (b) Arrhenius plot of F70. In panel(a) the measured lower temperatures are not reported for the sake of simplicity. In panel(b) the activation energies are indicated.

*Electrical conductivity of BL5F.* **Figure 56** shows the diagram for BL5F, here taken to represent the end member of the solid solution series. It was not possible to distinguish anymore between oxygen vacancies and protons (the conductivity in dry and wet is almost the same even at 350 °C). The calculated activation energy for oxygen vacancies is relatively low, and its value is closer to the one expected for protons rather than for oxygen vacancies. Therefore, given the relatively high proton uptake of this sample, it is not possible to completely rule out that the oxygen vacancies could be partially hydrated. On the other hand, a similar value (≈0.5 eV) was reported for oxygen vacancies in $Ba_{0.5}Sr_{0.5}Co_{0.8}Fe_{0.2}O_{3-\delta}$ [91]. The electronic conductivity of BL5F is much higher than the one of the other investigated samples in this subchapter, and this can be related to the fact that the $FeO_6$ octahedra network is not interrupted by $Zr^{4+}/Y^{3+}$ ions.

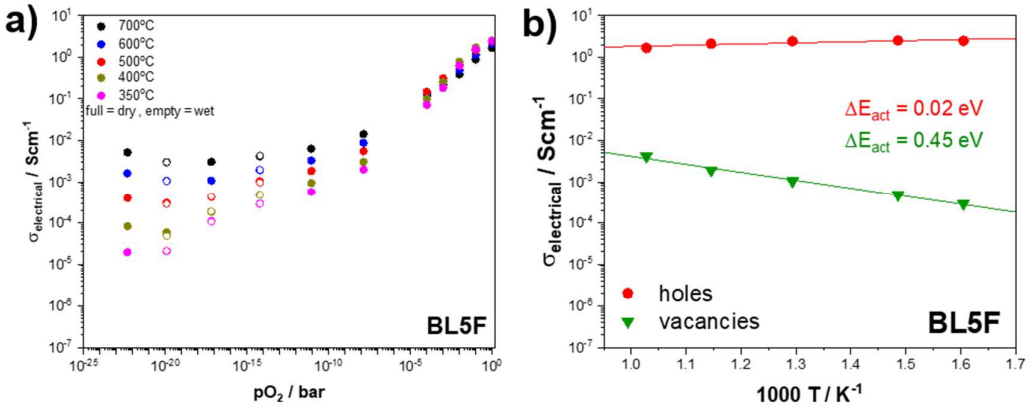


**Figure 56** (a) Brouwer diagram, (b) Arrhenius plot of BL5F. In panel(b) the activation energies are given.

*Summary plots of the electrical conductivity of Ba(Zr,Y,Fe)$O_{3-\delta}$.* **Figure 57(a)** summarizes the partial conductivities of holes, oxygen vacancies, and protons. The data for the electronic conductivity are measured in $pO_2 = 1$ bar at 400 °C. Protons and vacancy data are taken in the ionic plateaus ($pO_2 \approx 10^{-15}$ bar) at 350 °C. The mobilities in **Figure 57(b)** are calculated from the conductivities shown in **Figure 57(a)** and the carrier concentrations are from the TG hydration experiments (for protons) and calculated from the electroneutrality condition (for the oxygen vacancies). The data for x=0.01, 0.03 and 0.06 are measured with the setup described in **Section 2.2.7** since they are mainly proton conductors, and in view of their low electronic conductivities it is not necessary to use the setup coupled with the oxygen pump.

The electronic conductivities were already been discussed in **Section 3.2.3**, thus this subsection will focus on the trends concerning protons and oxygen vacancies. The proton conductivity shows a "V-shaped behavior" similar to the one observed for the degree of hydration **Figure 41**, but with a deeper minimum. The same trend is recognizable in the mobility, and to a smaller degree also in the carrier concentration. While for low iron content ($x< 0.2$) the variation in the conductivities is caused by the variation of both the carrier concentrations and proton mobility, for $x>0.2$ the differences in conductivity has to be ascribed mainly to a decrease in mobility. One hypothesis for the decreased mobility could be related to the difference in the coordination numbers of the B-cations (*cf.,* **Section 3.2.4**). For high iron content the coordination number of iron is lower than 6 because of the clustering of the oxygen vacancies, while this does not hold for Zr and Y, which remain largely six-fold coordinated. This could affect the hopping path of the protons by increasing the activation energy of the proton diffusion. If this were the only effect present, it would lead to much different proton diffusion activation energies for BZY10 compared to BF-based compositions. But the values obtained (*cf.,* **Figure 38**) are 0.43 eV for BZY10 and 0.46-0.55 eV for the BZYFs, this small difference can hardly justify the large decrease in mobility for iron-rich compositions, suggesting that other effects are also in place. Also the fact that F70 and F50 (with more iron 5-fold coordination) show higher proton mobilities than F30 would suggest that a compensation effect has to be present for iron-rich compositions. A possibility could be that also for protons a kind of percolation effect occurs, similarly to the electronic conductivity. This could apply also for the oxygen vacancies given the similar trend in **Figure 57**. A percolation effect for protons was in fact computationally predicted in ref. [70] for different yttrium concentrations in BZY. The argument was that while the dopant concentration is increased more protons will be trapped around Y cations (decreasing the proton mobility). But once the trapping zones start to overlap, a percolation path starts to form giving rise to an increase in mobility because the protons can perform long-range transport without the need for de-trapping. A similar behavior could explain the results in **Figure 57** with the iron atoms playing a similar role as Y dopants in BZY. On top of that, also a columbic effect can facilitate the mobility of protons in iron rich environments: the electrostatic repulsion of a proton in the transition state close to $Zr^{4+}$ ion will be higher than the one around a $Fe^{3+}$ environment.

Therefore, one may conclude that for iron below 30% the "isolated" trapping effect exerted by the iron centers will be predominant, leading to a strong decrease in the

proton mobility, while by increasing the amount of iron above 30% the overlap between the trapping zones will generate a percolation path, which, together with the decreased electrostatic repulsion, contributes to the increase of the proton mobility.

A very similar argument could be used to explain the trend for the oxygen vacancies. While for low iron content the decrease in mobility could be attributed to a trapping effect by iron cations, for high iron content the explanation could be slightly more complex. In fact, apart from the expected percolation effect and the decrease of electrostatic repulsion with increasing iron content, here also Fe-O bond covalency plays a role. As discussed in **Section 3.2.4**, the more iron is introduced in the sample, the more Fe*3d*-O*2p* orbital hybridization will be present, leading to a shrinking of the effective oxygen ionic radius (*i.e.,* less negative charge density because of the partial hole transfer). This shrinking facilitates oxygen migration. One might argue that this increase in available volume for the diffusion could be counteracted by the decrease of the lattice parameter with increasing iron content (which follows Vegard's law). But the diffusion coefficients of the oxygen vacancies reported in ref. [92] for BZY10 and $Ba_{0.5}Sr_{0.5}Co_{0.8}Fe_{0.2}O_{3-\delta}$ indicate that the effect of the TM-O bond covalency is much stronger than the one arising from the decrease of unit cell volume.

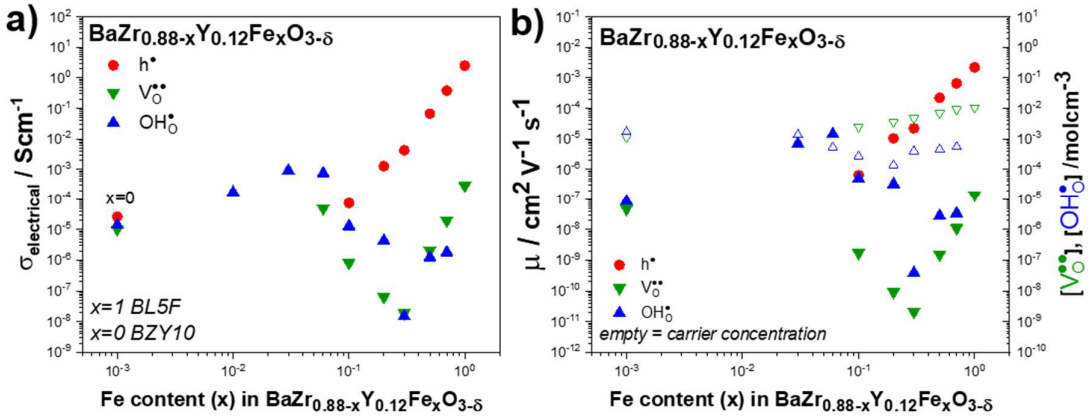


**Figure 57** (a) Summary plot of electrical conductivity, (b) calculated mobilities and charge carrier (protons and oxygen vacancies) concentrations as a function of the iron content in the BZYF solid solution series. The data for BZY10 [1, 87, 90] and BL5F are included as reference for x=0 and x=1.

The last point of this section pertains to the difference in the mobility of protons and oxygen vacancies observed in **Figure 57(b)**. The general trend is that the mobility of protons is higher than the one calculated for the oxygen vacancies. In general, protons have a lower migration barrier than oxygen vacancies since they are less charged and they can also create hydrogen bonds facilitating the migration. This effect is well visible for low-iron content samples where there is no percolation and other additional effect may be negligible. For high-iron content, the difference between proton and vacancies mobilities is smaller because of the combination of positive effects arising from percolation paths, columbic interaction and TM-O covalency.

### 3.2.6 Combined considerations

From the thermodynamic measurements of the $BaZr_{0.88-x}Fe_xY_{0.12}O_{3-\delta}$ solid solution series it is clear that increasing the amount of iron to more than 10% leads to a worsening of the hydration properties. The proton concentration decreases steeply, and the degree of hydration goes down by an order of magnitude. For low iron content this is caused mainly by an enthalpic effect ($\Delta H^o_{hydr}$ becomes less negative by increasing the amount of iron up to 10%). Instead, for high iron content this leads to both less favourable enthalpy and entropy of hydration. The protonic conductivity decreases by one order of magnitude or more with values ranging between $\approx 10^{-5}$-$10^{-6}$ $Scm^{-1}$. This would still allow the activation of the bulk path in a PCFC. The decreased proton conductivities in iron rich samples is to a larger share caused by a decrease in the proton mobilities. The worsening of the hydration properties in these compositions does not affect strongly the proton diffusion activation energies, whose values remain in the range of 0.39-0.55 eV, still relatively close to the one reported for BZY10 (0.43 eV).

From the oxygen non-stoichiometry measurements it is clear that in iron rich samples there is a non-negligible hole-hole interaction as evidenced from the bending in the van't Hoff plots. For iron-content $> 0.1$ a partially occupied impurity band of Fe*3d* states forms, as evidenced from UV-Vis measurements. In addition, the O *K*-edge (XRS) shows an increase of Fe*3d*-O*2p* hybridization with increasing amount of iron. This will influence positively the electronic conductivity of the material, leading to percolation phenomena: adding more than 10% of iron steeply increases the electronic conductivity as well as the hole mobility (the migration barrier for hole hopping in a $FeO_6$ sub-lattice is smaller than in a pure $ZrO_6$ matrix or for Fe centers embedded in a $ZrO_6$ matrix).

Regarding the structural analysis, below 10% of iron doping the cations' local environments are not impacted. For heavily iron-doped samples the buckling of the B-

O-B connections starts to appear. Moreover, for very high iron content (>0.3) the oxygen vacancies tend to cluster around iron (no changes in the first shell of Zr and Y from oxidized to reduced samples).

From the EIS measurements in the oxygen pump, it was possible for almost all the samples to separate the contribution in the conductivity arising from the three different charge carriers in these triple conducting oxides. It is clear that percolation phenomena concern also the diffusion of protons and oxygen vacancies, but it occurs at higher iron doping concentration ($> 0.3$) than in the case of the electronic conductivity ($> 0.1$). Both protons and oxygen vacancy conductivities show a minimum for 0.3 Fe, and the same profile is found for the calculated mobilities. This initial decrease in conductivities (mobilities) indicates that the iron centers are acting as proton/vacancy trap. By further increasing the amount of iron ($> 0.3$) a percolation path for protons and vacancies is created enabling a steep increase in the conductivities (and mobilities). In the case of the oxygen vacancies also the increased TM-O bond covalency favours the mobility because of the shrinking of oxygen ionic radii facilitating the oxygen migration.

The variation in the conductivity of protons and oxygen vacancies can be largely ascribed to a mobility effect.

## 3.3 Barium ferrate with redox-active dopants

Proton uptake is a key point in the choice of cathode material composition, but it is not the only property to consider [24,3,93]. Since these materials can be used as oxygen electrodes in PCFC and PCEC, the electronic conductivity also has to be considered. Unfortunately, it is often in conflict with the protonation capability of the material [24,3]. $Ba_{0.95}La_{0.05}FeO_{3-\delta}$ shows a moderate proton uptake of 0.7% at 400 °C in wet $N_2$, but its electronic conductivity is relatively poor (≈4 $Scm^{-1}$ at 400 °C in 10% $pO_2$). From SOFC cathode materials research, it is known that a partial substitution with Co, Ni, or Cu can increase the intrinsically low electronic conductivity of ferrate perovskites [94-96]. In the present section, a set of $(Ba_{0.95}La_{0.05})(Fe,TM)O_{3-\delta}$ perovskites in which 10-20% of iron is replaced with other first-row transition metals (TM) are investigated. The main interest is in exploring the dependence of proton uptake with materials composition, therefore the electronic structure aspects of these materials will largely be treated on a descriptive level (a detailed discussion of magnetic properties of Co, Ni, Cu -containing perovskites is beyond the scope of this thesis).

### 3.3.1 Oxygen stoichiometry and proton uptake

TGA isothermal and dynamic measurements for $(Ba_{0.95}La_{0.05})(Fe,TM)O_{3-\delta}$ are here discussed here for TM=Co, Ni, Cu (the attempt with Mn yielded a sample with hexagonal perovskite structure). The full series of van't Hoff and proton concentration vs temperature plots not reported in this section are included in **Appendix A**.

*TGA oxygen nonstoichiometry measurements.* The oxygen nonstoichiometry measurements follow the methods described in **Section 2.2.3**. While for composition with the B-site composed only by iron the absolute stoichiometry with iron in fully 3+ oxidation state is easily recognizable from the plateau at high T and low $pO_2$, the situation gets more complicated when other transition metal with mixed-valence are present. Unfortunately determining the absolute stoichiometry (*i.e.,* the oxidation state of the TMs) is not a trivial task. Even with a highly reducing atmosphere (up to 17% $H_2$ at 600°C) full decomposition to BaO, $La_2O_3$ and the transition metals in metallic form was achieved. Therefore, the absolute oxygen stoichiometries assignment in **Figure 58** is based on the apparent plateaus at high T in the lowest $pO_2$, combined with a consideration of the most plausible oxidation state of the TM dopant.

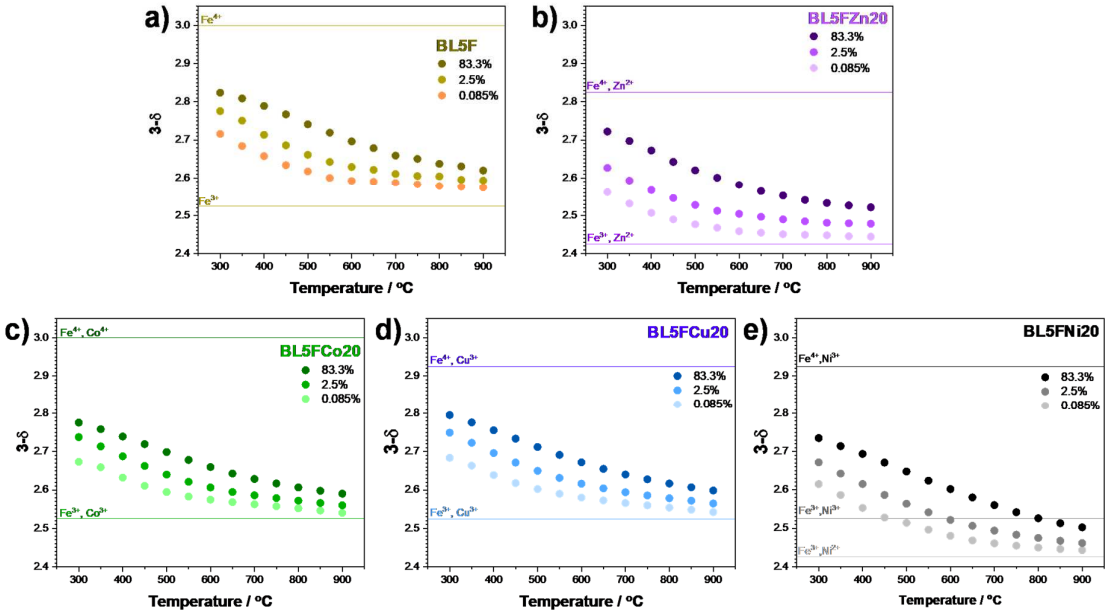


**Figure 58** Oxygen non-stoichiometry of (a) BL5F, (b) BL5FZn20 from [71], (c) BL5FCo20, (d) BL5FCu20, (e) BL5FNi20 measured in various $pO_2$. The horizontal lines refer to the oxygen stoichiometry for the indicated formal cation oxidation states.

Regarding the cobalt oxidation state, the plateau for the $Co^{3+}$ is less pronounced than for $Fe^{3+}$, but in $Ba_{0.5}Sr_{0.5}Co_{0.8}Fe_{0.2}O_{3-\delta}$ a comparably flat region is found at high *T*, which was largely assigned to $Co^{3+}$ in ref. [97] . Thus, the high-temperature plateau in **Figure 58(c)** is assigned to iron and cobalt both being in 3+ formal oxidation state.

The plateau for Cu is also assigned to all transition metal cations in the 3+ state based on the smaller lattice parameter (**Table 4**) of BL5FCu20 compared to BL5FZn20, which agrees with the Shannon ionic radii only if copper is predominantly $Cu^{3+}$. Moreover, $LaCuO_{3-\delta}$ perovskites with copper close to 3+ oxidation state are well known [98].

The assignment of the formal oxidation state of nickel is more complex. On one hand, the respective lattice parameter is the same of BL5FCu20 but the proton uptake is relatively high. This last point could suggest the assignment to $Ni^{2+}$ with its large ionic radius, which then would play the same role as $Zn^{2+}$ in generating local lattice distortion favouring the proton uptake. Both oxidation states, nickel as 3+ as well as 2+ are known in lanthanum nickelate (*cf.,* $LaNiO_3$ and $LaNiO_{2.5}$ the latter consists of 6-fold coordinated high spin $Ni^{2+}$ and square-planar low spin $Ni^{2+}$) [99]. The larger lattice parameter in BL5FNi20 compared to $LaNiO_3$ could also be taken as evidence for nickel being in the

2+ formal oxidation state. Thus, a final conclusion concerning the presence of $Ni^{2+}$ or $Ni^{3+}$ cannot be given here (and is anyway not a major objective in this thesis).

In fact, from **Figure 58** it is clear that the TM doping has only minor effects on the oxygen stoichiometry of the samples; in particular, the relative changes of $[V_O^{\bullet\bullet}]$ are in fact too small to explain the differences in the proton uptake discussed below.

*TGA hydration measurements.* The hydration measurements are performed as described in **Section 2.2.3**. **Figure 59** shows the proton concentration dependence with varying the cations composition. **Figure 60** depicts the temperature dependence of proton concentrations and the van't Hoff plots, while the $\Delta H^o_{hydr}$, $\Delta S^o_{hydr}$ and $\Delta G^o_{hydr}$(700K) are given in **Table 9**.

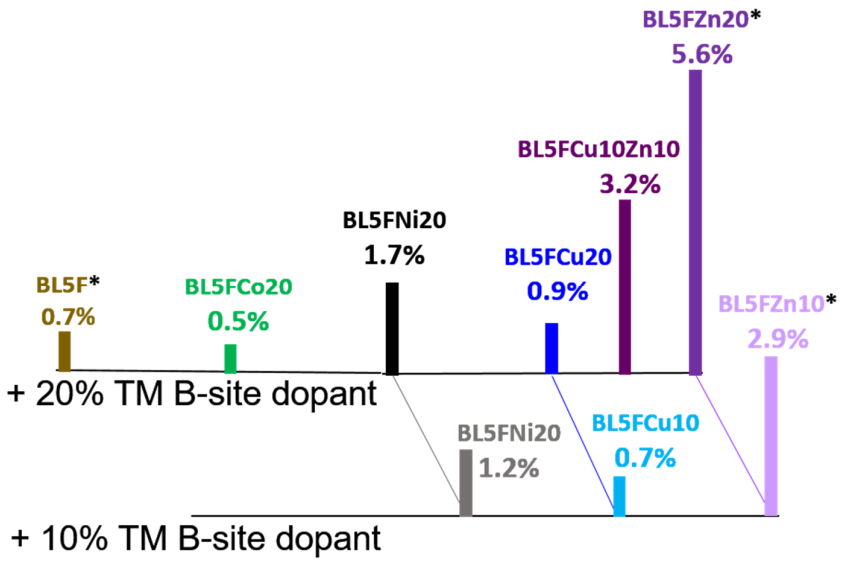


**Figure 59** Proton concentration at 400°C in 16.7 mbar of $pH_2O$ of $Ba_{0.95}La_{0.05}Fe_{0.8}(TM)_{0.2}O_{3-\delta}$ and $Ba_{0.95}La_{0.05}Fe_{0.9}(TM)_{0.1}O_{3-\delta}$. The data for BL5F, BL5FZn20 and BL5FZn10 have been measured by Dr. Zohourian and taken from ref. [24].

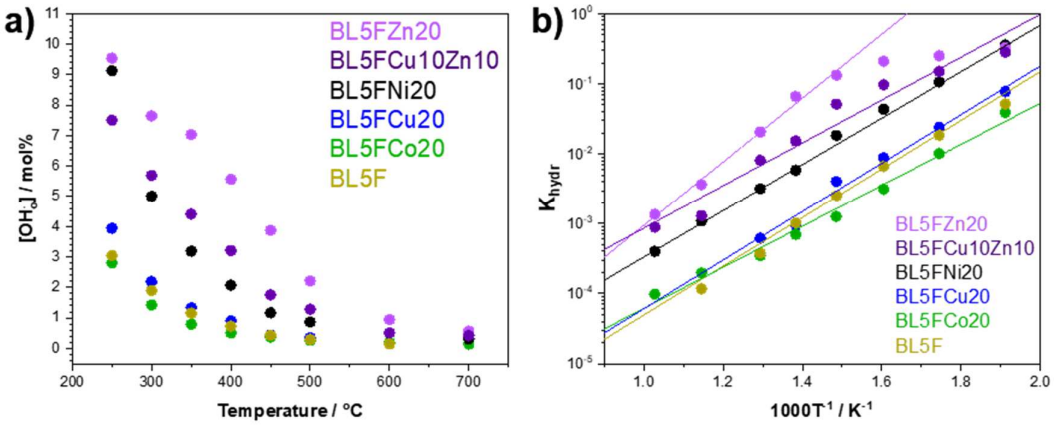


**Figure 60** (a) Proton concentration and (b) van't Hoff plots of the compositions with 20% of transition metal in the B-site. The data for BL5F and BL5FZn20 were measured by Dr. Zohourian and taken from ref. [24].

**Table 9** Summary of the hydration thermodynamic parameters for the transition metal series, calculated from the respective van't Hoff plots. BL5F, BL5FZn10 and BL5FZn20 data are from ref. [24].

| Sample | $\Delta H^{o}_{hydr}$ / kJmol$^{-1}$ | $\Delta S^{o}_{hydr}$ / JK$^{-1}$mol$^{-1}$ | $\Delta G^{o}_{hydr}$ / kJmol$^{-1}$ (700 K) |
|---|---|---|---|
| *BL5F | -62 ± 3 | -144 ± 5 | 39 ± 3 |
| BL5FCo20 | -56 ± 3 | -137 ± 4 | 40 ± 1 |
| BL5FNi20 | -63 ± 2 | -129 ± 3 | 27 ± 1 |
| BL5FNi10 | -62 ± 3 | -132 ± 4 | 30 ± 2 |
| BL5FCu20 | -66 ± 3 | -147 ± 4 | 37 ± 2 |
| BL5FCu10 | -59 ± 4 | -135 ± 5 | 36 ± 3 |
| *BL5FZn20 | -86 ± 5 | -143 ± 6 | 14 ± 2 |
| *BL5FZn10 | -53 ± 6 | -109 ± 10 | 23 ± 3 |
| BL5FCu10Zn10 | -59 ± 5 | -117 ± 8 | 23 ± 4 |

The data in **Figure 59** show that doping $Ba_{0.95}La_{0.05}FeO_{3-\delta}$ with nickel or zinc is beneficial for the proton uptake. Moreover, the comparison of BL5FZn10 vs BL5FZn20 and Bl5FNi20 vs BL5FNi10 indicates that the beneficial effect of adding zinc/nickel is roughly proportional to the dopant concentration. In **Section 3.1** and refs. [37,47] the increased proton uptake with Zn-doping was attributed to the local lattice distortion induced by the oversized $Zn^{2+}$, leading to a decrease of Fe-O bond covalency. A similar

behaviour could explain also the enhanced proton uptake with nickel doping. In fact, if Ni is in 2+ formal oxidation state, its ionic radius could be sufficiently large (0.69 Å [50]) to induce local distortion as well. However, in contrast to the case of Zn-doping, the assignment of formal nickel oxidation state is not unambiguous and the attempts already made did not provide a definitive answer. Using other methods such as X-ray Photoelectron Spectroscopy is challenging in this case because of the overlap with the other elements binding energies. Anyhow, the precise assignment of the formal oxidation state does not significantly affect the thermodynamic values included in **Table 9** since nickel doping varies the $V_O^{\bullet\bullet}$ concentration only slightly (**Figure 58(e)**). These arguments suggest that also other effects may be responsible for the enhanced proton uptake. The data in **Figure 59** and **Figure 60** show a decreased proton uptake for Co, and a slight improvement for Cu. The mixed composition BL5FCu10Zn10 is located in the middle between BL5FZn20 and BL5FCu20, and close to BL5FZn10.

In general, the TM-O bond covalency is found to increase with the *d* electrons number [100] , which in principle should lead to a decrease of the proton uptake moving along the transition metal row. This is not the case here, which further emphasizes that one simple descriptor cannot satisfactorily describe the hydration thermodynamics of triple conducting oxides. In fact, variation of the lattice parameters and local distortion influences the degree of covalency of the Fe-O bonds, and strictly speaking, the covalency and the degree of the O→Fe electron transfer are not directly proportional.

### 3.3.2 Electronic conductivity

**Figure 61** reports the electronic conductivities of the samples doped with 20% of transition metal, at different temperatures and $pO_2$. The electronic conductivity data are acquired on bar-shaped samples equilibrated at the different experimental conditions as described in **Section 2.2.7**. Additional plots for the conductivity of the samples doped with 10% transition metal, all the $pO_2$ dependences as well as the Arrhenius plots are included in **Appendix A**. The activation energies in the low-temperature region (derived from the Arrhenius plots in **Appendix A)** confirm that the electronic conduction proceeds via thermally activated small polaron hopping.

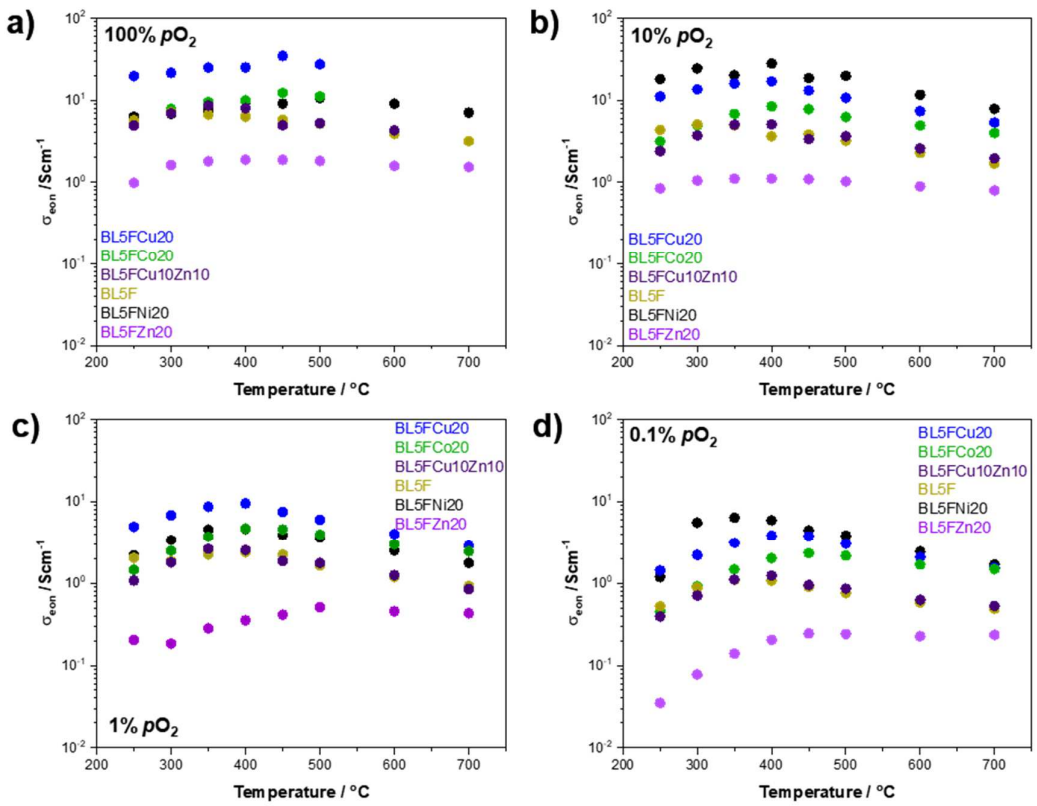


**Figure 61** Electronic conductivity of BL5F and 20% TM doped samples, in (a) 100%, (b) 10%, (c) 1% and (d) 0.1% $O_2$.

**Figure 61** shows that for the measured samples the electronic conductivities only increase up to a certain temperature, after which it starts to decrease significantly. The decrease can be explained by the release of lattice oxygen, compensated by the partial annihilation of electron holes. From this overview it is clear that the doping of BL5F with nickel, copper and cobalt is beneficial for the electronic conductivity, while Zn-doping is detrimental. The electronic conductivity depends on two quantities: the carrier concentration (in this case hole) and the mobility of the charge carrier. Considering that the relative changes of the samples' oxygen stoichiometry with $pO_2$ are fairly similar (*cf.*, **Figure 58**), one can attribute the variation of $\sigma_{eon}$ mainly to a change in the mobility among the different compositions.

### 3.3.3 Relation between proton uptake and $\sigma_{eon}$

Both protons and electron holes interact with the oxide ions in the material, therefore it is not too surprising to find some correlation between the proton concentrations and $\sigma_{eon}$. When comparing proton concentration and electronic conductivity for TM-doped barium ferrates, it has to be kept in mind that the variation of $[V_O^{\bullet\bullet}]$ is of minor importance since all these compositions are strongly oxygen-deficient, thus the relative changes in their $V_O^{\bullet\bullet}$concentration are small.

An anti-correlation between proton uptake and electronic conductivity was already reported in ref. [24], which was found to hold within materials group (barium ferrate; Co-doped ferrates; Zn-doped ferrates), however with some offset between the groups. There the explanation was that materials with higher electronic conductivity show higher TM-O bonds covalency disfavoring the proton uptake, as supported also by the arguments brought up in this thesis.

Including different redox-active transition metals in the material, the picture becomes more complex. In fact, for the compositions included in this section, one could – with a grain of salt – draw two different correlation lines, as shown in **Figure 62** ("inverse volcano").

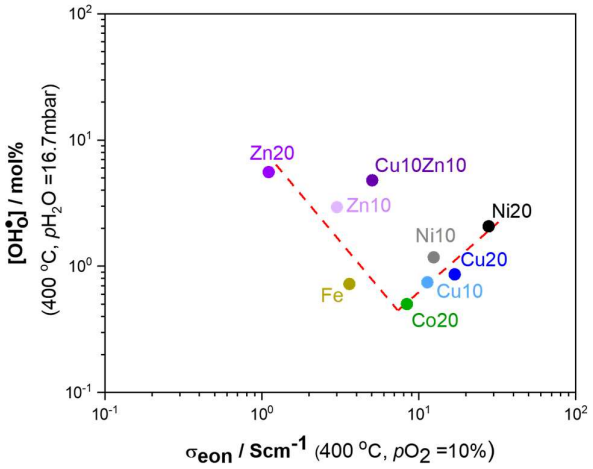


**Figure 62** Proton concentrations of $(Ba_{0.95}La_{0.05})(Fe,TM)O_{3-\delta}$ perovskites (400 °C in 16.7 mbar of $pH_2O$) vs. electronic conductivity (400 °C in 10% $pO_2$). The red dotted line only serves as a guide for the eyes.

From **Figure 62** is clear that the expected anti-correlation between protons and electronic conductivity holds for Zn, Fe, Co -containing samples. When introducing copper or nickel a positive correlation is found. A possible explanation of this behavior

could be that while Cu and Ni are expected to show an increased TM-O bond covalency, their higher occupancy of *d* orbitals (with respect to iron or cobalt) could limit the O→TM electron transfer, preserving the oxide ion basicity, thus still favoring the proton uptake. The beneficial effect of Cu-doping can also be seen by looking at the data point of BL5FCu10Zn10, which shows higher $\sigma_{eon}$ than BL5F and BL5FZn10 and higher proton uptake than BL5F.

Summarizing, this part of the thesis shows that variations in the cations composition lead to several effects, which are interdependent (local distortion, TM-O bond covalency, partial charge transfer, oxide ion basicity) and hard to disentangle. Specifically, it demonstrates that doping barium ferrate with other redox-active transition metals such as copper or nickel can improve both the electronic conductivity and the hydration. Moreover, a combined doping with nickel/copper and zinc can further improve the proton uptake of the material.

## 3.4 Influence of crystal structure and further oversized dopants on proton uptake

In this section, the role of the different crystal structures and oversized dopants not previously considered on $BaFeO_{3-\delta}$ will be explored with respect to proton uptake. It will be demonstrated that the cubic perovskite is the most suitable structure for proton uptake. The hydration properties of compositions with oversized dopants such as $Mg^{2+}$, $Zr^{4+}$, $Zn^{2+}$, $Y^{3+}$, $Ca^{2+}$ and their combinations occupying the B-site are also shown.

### 3.4.1 Effects of crystal structure on proton uptake

The hydration properties of the materials depend on the crystal structure. A comparison between cubic perovskites, hexagonal perovskites and $V_O^{\bullet\bullet}$-ordered orthorhombic structures in terms of their proton uptake is investigated. Exemplary XRD patterns are shown in **Figure 23**. These structures differ in their $BO_6$ connectivity: cubic and the orthorhombic o-$BaFeO_{2.5}$ (o-BF) exhibit corner sharing octahedra while the hexagonal h-$BaFeO_{3-\delta}$ (h-BF) has face sharing $BO_6$. Also the vacancy distribution is important for the proton uptake; in fact, having a random $V_O^{\bullet\bullet}$ arrangement in the structure typically favours proton uptake. An ordered oxygen vacancy sublattice implies that the vacancies are in a minimum of potential energy. So since they are stabilized the tendency of being hydrated is decreased. Another key point is the degree of covalency of the B-O bond: the more covalent this bond is, the more delocalized are the holes, and the less basic the oxide ions become because of the depleted electron density, thus the less favorable is the protonation.

The proton uptake for selected compositions with cubic, orthorhombic and hexagonal structures is given in **Figure 63**. BF can assume different crystal structure depending on the sintering gas atmosphere: in $O_2$ it is hexagonal [101], while in $N_2$ it turns into the orthorhombic superstructure $Ba_2Fe_2O_5$ with ordered $V_O^{\bullet\bullet}$ [102]. To obtain a cubic barium ferrate that is stable upon annealing, it is necessary to add 5% of La in the A-site in order to get a Goldschmidt tolerance factor closer to 1. Here, also a B-site doped composition is reported, BFMg10Ca10, which acquires a cubic structure when sintered at 1100 °C, and becomes hexagonal when sintered at 1300 °C. All the hydration plots are to be found in **Appendix A**.

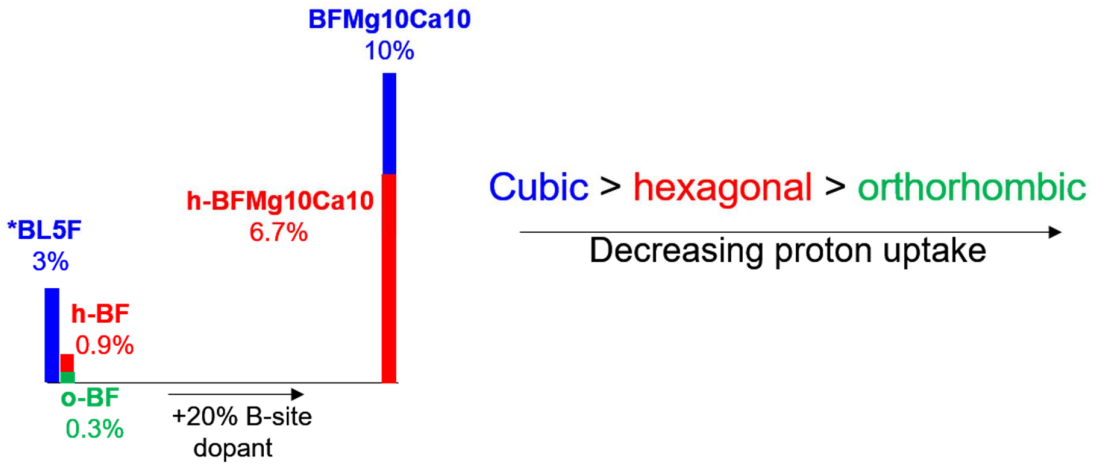


**Figure 63** Proton uptake at 250 °C in $pH_2O$=16.7 mbar for BF, BL5F and BFMg10Ca10. The different colours indicate the crystal structure: cubic (blue), hexagonal (red), orthorhombic (green). *Data point measured by Dr. Reihaneh Zohourian [37].

**Figure 63** indicates that the cubic perovskite structure favors proton uptake most, and the orthorhombic is favoring it least.

For the orthorhombic structure, the ordered unoccupied O sites are part of the regular crystal structure, *i.e.,* these are not oxygen vacancies in the defect-chemical sense. There is one unoccupied interstitial O site per $Ba_2Fe_2O_5$ formula unit, but its hydration is energetically less favorable. Thus, even if they have a high "vacancy" content and a low B-O bond covalency (resulting from a combination of 6-fold and 4-fold coordinated Fe and corresponding distortion or interruption of Fe-O-Fe connections), the negative effect of the vacancy-ordering prevails.

For the hexagonal structure, the low proton uptake could be related to the smaller vacancy content. Also the $BO_6$ face-sharing connections play a role for the hydration. On one hand, the strongly bent Fe-O-Fe at the face-sharing connections are expected to decrease Fe-O covalency and thus favor protonation. On the other hand, edges of these face sharing octahedra miss the probability of forming additional stabilizing hydrogen bonds as in the cubic perovskites. The cubic perovskites have the maximum proton uptake, even if they exhibit the larger degree of covalency of the B-O bond, but they present a high vacancy concentration, a disordered vacancy sublattice, and considerable possibilities to stabilize the proton via hydrogen bonds. As discussed in **Section 3.1**, by doping the B-site with a redox-inactive oversized ion, it is possible to decrease the degree

of the B-O bond covalency, favoring therefore proton uptake. However, a too large average B-site size will start to disfavor hydration, probably due to the formation of energetically inequivalent protonation sites. The latter aspect will be set out in the following section.

### 3.4.2 Effects of various oversized dopants on proton uptake

As clarified in **Section 3.1**, B-site redox-inactive oversized dopants play an important role in the proton uptake of ferrate perovskites. This is essentially due to the introduced local lattice distortion decreasing the Fe-O bonds covalency, therefore favoring the protonation of the more basic oxide ions.

The scope of this section is to identify trends of proton uptake related to the presence of several oversized dopants and their combinations. In particular, the hydration results for compositions containing $Ca^{2+}$, $Mg^{2+}$, $Zn^{2+}$, $Y^{3+}$ and $Zr^{4+}$ are covered. **Figure 64** shows the proton uptake at 250 °C in $pH_2O$ = 16.7 mbar for selected compositions. Their hydration plots as well as the extracted thermodynamic quantities are included in **Appendix A**.

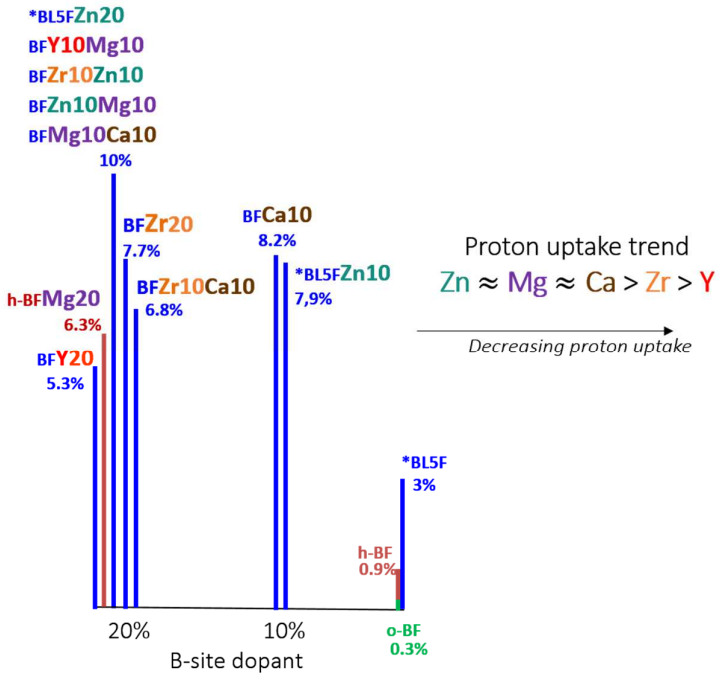


**Figure 64** Proton uptake at 250 °C in $pH_2O$ =16.7 mbar for different compositions with oversized dopants. The different colours indicate the crystal structure: cubic (blue),

hexagonal (red), orthorhombic (green). *Data point measured by Dr. Reihaneh Zohourian [24].

From **Figure 64** is possible to conclude that zinc, calcium and magnesium have a positive effect on proton uptake, while zirconium and yttrium are least favouring the protonation.
This becomes clear by looking in more details at the proton uptake of selected compositions, for example:

- $[OH_O^\bullet]_{Zn^{2+}} \approx [OH_O^\bullet]_{Mg^{2+}}$: BL5FZn20 and BFZn10Mg10 both incorporate 10% of protons.
- $[OH_O^\bullet]_{Zn^{2+}} \approx [OH_O^\bullet]_{Ca^{2+}}$: BL5FZn10 and BFCa10 have the same proton uptake within the error bar.
- $[OH_O^\bullet]_{Mg^{2+}} \approx [OH_O^\bullet]_{Ca^{2+}}$: both have an effect on protonation comparable to $Zn^{2+}$.
- $[OH_O^\bullet]_{Ca^{2+}} > [OH_O^\bullet]_{Zr^{4+}}$: BFCa10 incorporates more protons than BFZr10Ca10.
- $[OH_O^\bullet]_{Mg^{2+}}$, $[OH_O^\bullet]_{Zr^{4+}} > [OH_O^\bullet]_{Y^{3+}}$: BFZr20 is better than BFY20, and h-BFMg20 -even if hexagonal- performs better than BFY20.

To understand the underlying reasons is not trivial. Some considerations can be made by comparing the (weighted) average B-site size calculated from the ionic radii [50] and the proton uptake in **Figure 65**. There exists a region (the *maximum* of the "volcano") in which the compositions with an average B-size size between 0.66-0.68 Å are most keen to be protonated. The ones below 0.66 Å probably lack in local distortions for reducing the B-O bond covalency (the Goldschmidt tolerance factor for BL5F of 1.04 is close to the ideal value). Above 0.68 Å the B-site becomes too large, which can lead to the formation of energetically equivalent protonation sites decreasing the overall proton uptake capability.

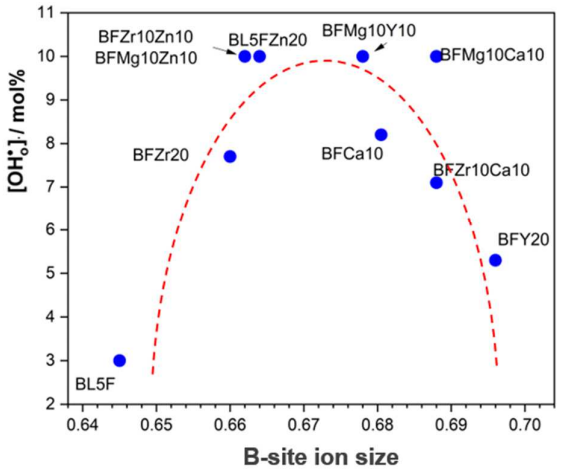


**Figure 65** Volcano plot of proton uptake (250 °C, $pH_2O$ = 16.7 mbar) vs average B-size of the B-cation (using Shannon ionic radii for 6-fold coordinated cations).

BFCa10 and BFZr20 are slightly negative outliers in this trend. The first one is in fact the only composition with only 10% of oversized dopant. Regarding BFZr20, $Zr^{4+}$ is not as good as $Mg^{2+}$, $Zn^{2+}$ and $Ca^{2+}$ for proton uptake. This could be related to the higher acidity of Zr-containing compositions given the higher valence of the zirconium ion.
This exploration leaves room for further fine-tuning of the composition but gives solid guidelines for the choice of dopants in order to improve the protonation of these perovskites.

# 4 Conclusions

This thesis is focused on the interplay of protonic defects, oxygen vacancies and electron holes in triple conducting oxides. As master example $BaFeO_{3-\delta}$ based perovskites are employed, which can be doped on the Ba as well as Fe site.

The first part of this work clarified the role played by oversized $Zn^{2+}$ and $Y^{3+}$ dopants in barium ferrate in enhancing the hydration properties of the material. The beneficial effect on protonation was attributed to a higher degree of disorder in the local structure of doped samples, which translates in B-O-B bonds buckling. The B-O-B buckling reduces the Fe-O bond covalency (less Fe*3d*-O*2p* orbital overlap) and decreases therefore the hole transfer from iron to oxygen. This leaves more negative charge density on the oxide ions, which increases their basicity and propensity for protonation. Another important finding is that a "clustering" of oxygen vacancies around some specific ions leads to energetically inequivalent protonation sites, decreasing the hydration capability of certain compositions (*i.e.,* heavily $Y^{3+}$ doped materials). These concepts can, in principle, be applied to understand the hydration properties of a larger set of perovskites doped with other oversized dopants.

In the second part, the solid solution series $BaZr_{0.88-x}Fe_xY_{0.12}O_{3-\boldsymbol{\delta}}$ ($0 \leq x \leq 0.8$) was investigated as model material, which ranges from an electrolyte-type material (low Fe-content) to cathode-type material (high Fe-content). This allows one to follow its thermodynamical, structural and electronic changes upon introducing different amounts of iron. Already only 10% of iron leads to the formation of an impurity band and to electronic percolation phenomena along the $FeO_6$ network, and decreases the degree of hydration by one order of magnitude. This can be related to Fe-O bond covalency and corresponding hole transfer from Fe to O. Its effect shows also up in the measured oxygen stoichiometries, which deviate from ideally dilute behavior and can be interpreted in terms of a hole-hole transfer. Although the hydration is disfavored by adding iron, this does not strongly affect the proton diffusion activation energies, which remain close to the value reported for $BaZr_{0.9}Y_{0.1}O_{2.95}$ electrolyte. For high iron contents (> 30%) percolation paths play a role also for proton and oxygen vacancy transport, which translates to an increase of their partial conductivities. Overall, the protonic conductivities are above $10^{-5}$-$10^{-6}$ $Scm^{-1}$ in the range of interest (operation temperatures of a PCFC). In fact, these values would allow for the activation of the bulk path in a PCFC, enhancing the overall catalytic activity.

The third part explores the effect of B-site doping with some *3d* redox-active transition metals focusing on proton uptake and electronic conductivity. Doping with Zn and Ni improved the hydration, and Co, Ni and Cu doping favored the electronic conductivity. In a simplistic picture, having a high TM-O bond covalency translates into higher electronic conductivity and to lower proton uptake because of increased TM→O electron hole transfer, which decreases the oxygen ions basicity. However, for Cu, Ni doped samples with high electronic conductivities, also high proton uptake is observed. This can be attributed to their high *d* orbital occupancy, which disfavors the TM→O electron hole transfer, preserving the basicity of the oxide ion even if the TM-O bond covalency is high. Therefore, the TM-O bond covalency cannot be used as a single descriptor for the hydration properties, and other effects also have to be considered.

The last part of this thesis investigates the hydration properties for different perovskite-related crystal structures. The major result is that the proton uptake depends on the crystal structure because of the interplay of effects like $BO_6$ octahedra connectivity (corner sharing, face sharing), possible $V_O^{\bullet\bullet}$-ordering, and TM-O bond covalency.

Summarizing, this thesis provides a systematic study on the effects arising from protonic defects, oxygen vacancies and electron holes in triple conducting oxides from a structural, electronic and defect chemical point of view. When dealing with the presence of three different and (often) interacting charge carriers in a material, many effects contribute and thus the hydration properties can be influenced in different ways as schematized in **Figure 66**. When aiming at optimizing a cathode material composition, the following aspects should be considered:

(i) Basicity is an important parameter for the proton uptake, given the incorporation of protons via an acid-base reaction. The TM→O hole transfer will decrease the basicity of the oxide ions.

(ii) Oversized dopants favor the hydration because they introduce local lattice distortion whose directly decrease the TM→O hole transfer.

(iii) A random oxygen vacancy distribution is preferred by avoiding the formation of energetically inequivalent oxygen sites, where typically some sites are less prone to hydrate.

(iv) Doping the barium ferrate with other redox-active transition metal is a good strategy to enhance its electronic conduction. Based on experience from SOFC cathode materials,

this is expected to be also beneficial for the oxygen reduction reaction. Combined doping with Zn and Cu/Ni can merge the advantages of both doping strategies.
(v) The cubic perovskite crystal structure provides an excellent basis for triple conducting oxides. Its corner sharing $BO_6$ octahedra connectivity supplies the required electronic conductivity. It also forms the optimal environment for protons with the possibility of forming additional hydrogen bonds, which favor proton incorporation as well as proton transfer. Nevertheless, related structures such as layered double perovskites or Ruddlesden-Popper phases could also be interesting.
(vi) The catalytic activity, the stability towards hydrothermal conditions and secondary phase formation, as well as the chemical and mechanical compatibility with the electrolyte should also paid attention to, but they are beyond the scope of the present work.

It is obvious that disentangling the effects that arise from the presence of three different and (often) interacting charge carriers is not trivial, and in some cases this could be done just partially or on a qualitative level. Nevertheless, these attempts are expected to be helpful in optimizing the performance and rationally designing oxygen electrodes for protonic ceramic fuel and electrolysis cells.

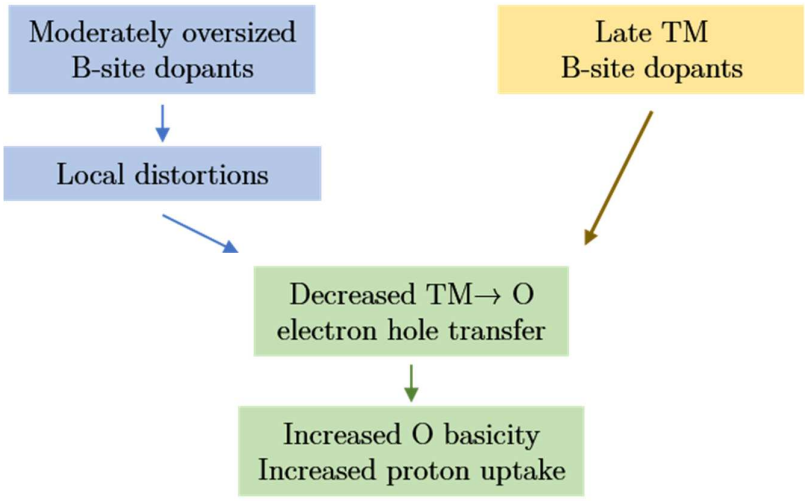


**Figure 66** Effects of B-site dopants in triple conducting perovskites, as deduced in the present thesis on the example of $BaFeO_3$. Doping with oversized dopants will improve only the proton uptake, while doping with the late TMs will improve both proton uptake and electronic conductivity. A combined doping is thus suggested.

# REFERENCES

(**1**) Kreuer, K.-D. Proton-conducting oxides. *Annu. Rev. Mater. Res.* **2003,** *33* (1), 333-359.

**(2)** Duan, C.; Huang, J.; Sullivan, N.; O'Hayre, R. Proton-conducting oxides for energy conversion and storage. *Appl. Phys. Rev.* **2020,** *7* (1), 011314.

**(3)** Merkle, R.; Hoedl, M. F.; Raimondi, G.; Zohourian, R.; Maier, J. Oxides with Mixed Protonicand Electronic Conductivity. *Annu. Rev. Mater. Res.* **2021,** (51), 461-493.

**(4)** Forrat, F.; Christen, M.; Dauge, G.; Danner, G.; Trevoux, P. Electrolyte Solide a base de $LaAlO_3$. Application aux Piles a Combustible. *Compt. Rend. Acad. Sci.* **1964,** *259* (17), 2813.

**(5)** Stotz, S.; Wagner, C. Die Löslichkeit von Wasserdampf und Wasserstoff in festen Oxiden. *Ber. Bunsenges. Phys. Chem.* **1966,** *70* (8), 781-788.

**(6)** Iwahara, H.; Uchida, H.; Maeda, N. High temperature fuel and steam electrolysis cells using proton conductive solid electrolytes. *J. Power Sources* **1982,** *7* (3), 293-301.

**(7)** Uchida, H.; Maeda, N.; Iwahara, H. Steam concentration cell using a high temperature type proton conductive solid electrolyte. *J. Appl. Electrochem.* **1982,** *12* (6), 645-651.

**(8)** Iwahara, H.; Esaka, T.; Uchida, H.; Maeda, N. Proton conduction in sintered oxides and its application to steam electrolysis for hydrogen production. *Solid State Ion.* **1981,** *3*, 359-363.

**(9)** Iwahara, H.; Uchida, H.; Yamasaki, I. High-temperature steam electrolysis using $SrCeO_3$-based proton conductive solid electrolyte. *Int. J. Hydrog. Energy* **1987,** *12* (2), 73-77.

**(10)** Iwahara, H. Hydrogen pumps using proton-conducting ceramics and their applications. *Solid State Ion.* **1999,** *125* (1-4), 271-278.

**(11)** Iwahara, H. Proton conducting ceramics and their applications. *Solid State Ion.* **1996,** *86*, 9-15.

**(12)** Uchida, H.; Maeda, N.; Iwahara, H. Relation between proton and hole conduction in $SrCeO_3$-based solid electrolytes under water-containing atmospheres at high temperatures. *Solid State Ion.* **1983,** *11* (2), 117-124.

**(13)** Iwahara, H.; Uchida, H.; Tanaka, S. High temperature-type proton conductive solid oxide fuel cells using various fuels. *J. Appl. Electrochem.* **1986,** *16* (5), 663-668.

**(14)** Hamakawa, S.; Hibino, T.; Iwahara, H. Electrochemical methane coupling using protonic conductors. *J. Electrochem. Soc.* **1993,** *140* (2), 459.

**(15)** Babilo, P.; Uda, T.; Haile, S. M. Processing of yttrium-doped barium zirconate for high proton conductivity. *J. Mater. Res.* **2007,** *22* (5), 1322-1330.

**(16)** Yamazaki, Y.; Hernandez-Sanchez, R.; Haile, S. M. High total proton conductivity in large-grained yttrium-doped barium zirconate. *Chem. Mater.* **2009,** *21* (13), 2755-2762.
**(17)** Tong, J.; Clark, D.; Bernau, L.; Sanders, M.; O'Hayre, R. Solid-state reactive sintering mechanism for large-grained yttrium-doped barium zirconate proton conducting ceramics. *J. Mater. Chem.* **2010,** *20* (30), 6333-6341.
**(18)** Nikodemski, S.; Tong, J.; O'Hayre, R. Solid-state reactive sintering mechanism for proton conducting ceramics. *Solid State Ion.* **2013,** *253*, 201-210.
**(19)** Tong, J.; Clark, D.; Hoban, M.; O'Hayre, R. Cost-effective solid-state reactive sintering method for high conductivity proton conducting yttrium-doped barium zirconium ceramics. *Solid State Ion.* **2010,** *181* (11-12), 496-503.
**(20)** Duan, C.; Tong, J.; Shang, M.; Nikodemski, S.; Sanders, M.; Ricote, S.; Almansoori, A.; O'Hayre, R. Readily processed protonic ceramic fuel cells with high performance at low temperatures. *Science* **2015,** *349* (6254), 1321-1326.
**(21)** Merkle, R.; Poetzsch, D.; Maier, J. Oxygen reduction reaction at cathodes on proton conducting oxide electrolytes: contribution from three phase boundary compared to bulk path. *ECS Trans.* **2015,** *66* (2), 95.
**(22)** Tong, J.; Yang, W.; Zhu, B.; Cai, R. Investigation of ideal zirconium-doped perovskite-type ceramic membrane materials for oxygen separation. *J. Membr. Sci.* **2002,** *203* (1-2), 175-189.
**(23)** Choi, S.; Kucharczyk, C. J.; Liang, Y.; Zhang, X.; Takeuchi, I.; Ji, H.-I.; Haile, S. M. Exceptional power density and stability at intermediate temperatures in protonic ceramic fuel cells. *Nat. Energy* **2018,** *3* (3), 202-210.
**(24)** Zohourian, R.; Merkle, R.; Raimondi, G.; Maier, J. Mixed-conducting perovskites as cathode materials for protonic ceramic fuel cells: understanding the trends in proton uptake. *Adv. Funct. Mater.* **2018,** *28* (35), 1801241.
**(25)** Wang, Z.; Yang, W.; Shafi, S. P.; Bi, L.; Wang, Z.; Peng, R.; Xia, C.; Liu, W.; Lu, Y. A high performance cathode for proton conducting solid oxide fuel cells. *J. Mater. Chem. A* **2015,** *3* (16), 8405-8412.
**(26)** Sukkurji, P. A.; Molinari, A.; Benes, A.; Loho, C.; Chakravadhanula, V. S. K.; Garlapati, S. K.; Kruk, R.; Clemens, O. Structure and conductivity of epitaxial thin films of barium ferrite and its hydrated form $BaFeO_{2.5-x+\delta}(OH)_{2x}$. *J. Phys. D: Appl. Phys.* **2017,** *50* (11), 115302.
**(27)** Kasyanova, A. V.; Tarutina, L. R.; Rudenko, A. O.; Lyagaeva, J. G.; Medvedev, D. A. Ba (Ce,Zr)$O_3$-based electrodes for protonic ceramic electrochemical cells: towards highly compatible functionality and triple-conducting behaviour. *Russ. Chem. Rev.* **2020,** *89* (6), 667.

**(28)** Poetzsch, D.; Merkle, R.; Maier, J. Stoichiometry variation in materials with three mobile carriers—thermodynamics and transport kinetics exemplified for protons, oxygen vacancies, and holes. *Adv. Funct. Mater.* **2015,** *25* (10), 1542-1557.
**(29)** Kreuer, K. On the complexity of proton conduction phenomena. *Solid State Ion.* **2000,** *136*, 149-160.
**(30)** Longo, A.; Giannici, F.; Balerna, A.; Ingrao, C.; Deganello, F.; Martorana, A. Local environment of yttrium in Y-doped barium cerate compounds. *Chem. Mater.* **2006,** *18* (24), 5782-5788.
**(31)** Bjørheim, T. S.; Hoedl, M. F.; Merkle, R.; Kotomin, E. A.; Maier, J. Proton, hydroxide ion, and oxide ion affinities of closed-shell oxides: importance for the hydration reaction and correlation to electronic structure. *J. Phys. Chem. C* **2019,** *124* (2), 1277-1284.
**(32)** Poetzsch, D.; Merkle, R.; Maier, J. Proton conductivity in mixed-conducting BSFZ perovskite from thermogravimetric relaxation. *J. Phys. Chem. Chem. Phys.* **2014,** *16* (31), 16446-16453.
**(33)** Shinjo, T.; Ichida, T.; Takada, T. $Fe^{57}$ Mössbauer Effect and Magnetic susceptibility of hexavalent iron compounds; $K_2FeO_4$ and $BaFeO_4$. *J. Phys. Soc. Japan* **1970,** *29*, 11-116.
**(34)** Gallagher, P. K.; MacChesney, J. B.; Buchanan, D. N. E. Mössbauer effect in the system $BaFe_{2.5\text{-}3.0}$. *J. Chem. Phys.* **1965,** *43*, 516-520.
**(35)** Munir, Z.; Anselmi-Tamburini, U.; Ohyanagi, M. The effect of electric field and pressure on the synthesis and consolidation of materials: A review of the spark plasma sintering method. *J. Mater. Sci.* **2006,** *41* (3), 763-777.
**(36)** Vračar, M.; Kuzmin, A.; Merkle, R.; Purans, J.; Kotomin, E.; Maier, J.; Mathon, O. Jahn-Teller distortion around $Fe^{4+}$ in $SrFe_xTi_{1-x}O_{3-\delta}$ from X-ray absorption spectroscopy, X-ray diffraction, and vibrational spectroscopy. *Phys. Rev. B* **2007,** *76* (17), 174107.
**(37)** Raimondi, G.; Giannici, F.; Longo, A.; Merkle, R.; Chiara, A.; Hoedl, M. F.; Martorana, A.; Maier, J. X-ray Spectroscopy of $(Ba,Sr,La)(Fe,Zn,Y)O_{3-\delta}$ Identifies Structural and Electronic Features Favoring Proton Uptake. *Chem. Mater.* **2020,** *32* (19), 8502-8511.
**(38)** Clementiev, K. V. XAFSmass, freeware:
www.cells.es/Beamlines/CLAESS/software/xafsmass.html.
**(39)** Stern, E. Theory of the extended x-ray-absorption fine structure. *Phys. Rev. B* **1974,** *10* (8), 3027.
**(40)** Klementev, K. V. Extraction of the fine structure from x-ray absorption spectra. *J. Phys. D: Appl. Phys.* **2001,** *34* (2), 209.

**(41)** Rehr, J. J.; Kas, J. J.; Prange, M. P.; Sorini, A. P.; Takimoto, Y.; Vila, F. Ab initio theory and calculations of X-ray spectra. *J. Compt. Rend. Phys.* **2009,** *10* (6), 548-559.

**(42)** Ravel, B. ATOMS: crystallography for the X-ray absorption spectroscopist. *J. Synchrotron Radiat.* **2001,** *8* (2), 314-316.

**(43)** Huotari, S.; Sahle, C. J.; Henriquet, C.; Al-Zein, A.; Martel, K.; Simonelli, L.; Verbeni, R.; Gonzalez, H.; Lagier, M.-C.; Ponchut, C. A large-solid-angle X-ray Raman scattering spectrometer at ID20 of the European Synchrotron Radiation Facility. *Journal of synchrotron radiation* **2017,** *24* (2), 521-530.

**(44)** Sahle, C. J.; Mirone, A.; Niskanen, J.; Inkinen, J.; Krisch, M.; Huotari, S. Planning, performing and analyzing X-ray Raman scattering experiments. *J. Synchrotron Radiat.* **2015,** *22* (2), 400-409.

**(45)** Yoly, Y.; Cavallari, C.; Guda, S. A.; Sahle Ch, J. Full-Potential Simulation of X-ray Raman Scattering Spectroscopy. *J. Chem. Theory Comput.* **2017,** *5* (13), 2172-2177.

**(46)** Yoly, Y.; Cabaret, D.; Renevier, H.; Natoli, C. Electron Population Analysis by Full-Potential X-Ray Absorption Simulations. *Phys. Rev. Lett.* **1999,** (82), 2398-2401.

**(47)** Raimondi, G.; Longo, A.; Giannici, F.; Merkle, R.; Hoedl, M. F.; Chiara, A.; Sahle, C. J.; Maier, J. Electronic modifications in (Ba,La)(Fe,Zn,Y)$O_{3-\delta}$. *J. Mater. Chem. A* **2022**, *in revision.*

**(48)** Poetzsch, D.; Merkle, R.; Maier, J. Proton uptake in the $H^+$-SOFC cathode material $Ba_{0.5}Sr_{0.5}Fe_{0.8}Zn_{0.2}O_{3-\delta}$: transition from hydration to hydrogenation with increasing oxygen partial pressure. *Faraday Discuss.* **2015,** *182*, 129-143.

**(49)** Zohourian, R.; Merkle, R.; Maier, J. Proton uptake into the protonic cathode material $BaCo_{0.4}Fe_{0.4}Zr_{0.2}O_{3-\delta}$ and comparison to protonic electrolyte materials. *Solid State Ion.* **2017,** *299*, 64-69.

**(50)** Shannon, R.; Prewitt, C. Revised values of effective ionic radii. *Acta Crystallogr. B Struct. Cryst. Cryst. Chem.* **1970,** *26* (7), 1046-1048.

**(51)** Lein, H. L.; Wiik, K.; Grande, T. Thermal and chemical expansion of mixed conducting $La_{0.5}Sr_{0.5}Fe_{1-x}Co_xO_{3-\delta}$ materials. *Solid State Ion.* **2006,** *177* (19-25), 1795-1798.

**(52)** Hoedl, M. F.; Gryaznov, D.; Merkle, R.; Kotomin, E. A.; Maier, J. Interdependence of Oxygenation and Hydration in Mixed-Conducting (Ba,Sr)$FeO_{3-\delta}$ Perovskites Studied by Density Functional Theory. *J. Phys. Chem. C* **2020,** *124* (22), 11780-11789.

**(53)** De Jong, M.; Chen, W.; Angsten, T.; Jain, A.; Notestine, R.; Gamst, A.; Sluiter, M.; Ande, C. K.; Van Der Zwaag, S.; Plata, J. J. Charting the complete elastic properties of inorganic crystalline compounds. *Sci. data* **2015,** *2* (1), 1-13.

**(54)** Medarde, M.; Mesot, J.; Lacorre, P.; Rosenkranz, S.; Fischer, P.; Gobrecht, K. High-pressure neutron-diffraction study of the metallization process in $PrNiO_3$. *Phys. Rev. B* **1995,** *52* (13), 9248.

**(55)** Radaelli, P.; Iannone, G.; Marezio, M.; Hwang, H.; Cheong, S.; Jorgensen, J.; Argyriou, D. Structural effects on the magnetic and transport properties of perovskite $A_{1-x}A'_xMnO_3$ (x= 0.25, 0.30). *Phys. Rev. B* **1997,** *56* (13), 8265.

**(56)** Salamon, M. B.; Jaime, M. The physics of manganites: Structure and transport. *Rev. Mod. Phys.* **2001,** *73* (3), 583.

**(57)** Fehse, M.; Sahle Ch, J.; Hogan, M. P.; Cavallari, C.; Kelder, E. M.; Alfredsson, M.; Longo, A. Bulk-Sensitive Soft X-ray Edge Probing for Elucidation of Charge Compensation in Battery Electrodes. *J. Phys. Chem. C* **2019,** *123*, 24396-24403.

**(58)** Benfatto, M.; Natoli, C. A unified scheme of interpretation of the X-ray absorption spectra used as structural probe. *J. Non-Cryst. Solids* **1987,** *95*, 319-326.

**(59)** Frati, F.; Hunault, M.; de Groot, F. M. F. Oxygen K-edge X-ray Absorption Spectra. *Chem Rev* **2020,** *120* (9), 4056-4110.

**(60)** Mueller, D. N.; De Souza, R. A.; Brendt, J.; Samuelis, D.; Martin, M. Oxidation states of the transition metal cations in the highly nonstoichiometric perovskite-type oxide $Ba_{0.1}Sr_{0.9}Co_{0.8}Fe_{0.2}O_{3-\delta}$. *J. Mater. Chem.* **2009,** *19* (14), 1960-1963.

**(61)** Wilke, M.; Farges, F.; Petit, P.-E.; Brown Jr, G. E.; Martin, F. Oxidation state and coordination of Fe in minerals: An Fe *K*-XANES spectroscopic study. *J. Am. Mineral.* **2001,** *86* (5-6), 714-730.

**(62)** Itoh, T.; Shirasaki, S.; Ofuchi, H.; Hirayama, S.; Honma, T.; Nakayama, M. Oxygen partial pressure dependence of in situ X-ray absorption spectroscopy at the Co and Fe *K*-edges for $La_{0.6}Sr_{0.4}Co_{0.2}Fe_{0.8}O_{3-\delta}$. *Solid State Commun.* **2012,** *152* (4), 278-283.

**(63)** Woolley, R. J.; Illy, B. N.; Ryan, M. P.; Skinner, S. In situ determination of the nickel oxidation state in $La_2NiO_{4+\delta}$ and $La_4Ni_3O_{10-\delta}$ using X-ray absorption near-edge structure. *J. Mater. Chem.* **2011,** *21* (46), 18592-18596.

**(64)** Kim, D.-Y.; Miyoshi, S.; Tsuchiya, T.; Yamaguchi, S. Electronic defect formation in Fe-doped $BaZrO_3$ studied by X-ray absorption spectroscopy. *Chem. Mater.* **2014,** *26* (2), 927-934.

**(65)** Hong, W. T.; Stoerzinger, K. A.; Lee, Y.-L.; Giordano, L.; Grimaud, A.; Johnson, A. M.; Hwang, J.; Crumlin, E. J.; Yang, W.; Shao-Horn, Y. Charge-transfer-energy-dependent oxygen evolution reaction mechanisms for perovskite oxides. *Energy Environ. Sci.* **2017,** *10* (10), 2190-2200.

**(66)** Hombo, J.; Matsumoto, Y.; Kawano, T. Electrical conductivities of $SrFeO_3$ and $BaFeO_3$ perovskites. *J. Sol. St. Chem* **1990,** (84), 138-143.

**(67)** Bouwmeester, H.J.M.; Kruidhof, H.; Burggraaf, A. Importance of the surface exchange kinetics as rate limiting step in oxygen permeation through mixed-conducting oxides**.** *Solid State Ion.* **1994,** *72*, 185-194.
**(68)** Poetzsch, D.; Merkle, R.; Maier, J. Proton conductivity in mixed-conducting BSFZ perovskite from thermogravimetric relaxation. *Phys. Chem. Chem. Phys.* **2014,** *16* (31), 16446-16453.
**(69)** Kreuer, K. D.; Schönherr, E.; Maier, J. Protons and oxygen diffusion in $BaCeO_3$ based compounds: A combined thermal gravimetric analysis and conductivity study. *Solid State Ion.* **1994,** *70*, 278-284.
**(70)** Draber, F. M.; C. Ader; J. P. Arnold; S. Eisele; S. Grieshammer; S. Yamaguchi; Martin, M. Nanoscale percolation in doped $BaZrO_3$ for high proton mobility. *Nat. Mater.* **2020,** *19*, 338-347.
**(71)** Zohourian, R. Mixed-conducting perovskites as cathodes in protonic ceramic fuel cells: defect chemistry and transport properties. University of Stuttgart, **2018**.
**(72)** Mizusaki, J.; Mima, Y.; Yamauchi, S.; Fueki, K.; Tagawa, H. Nonstoichiometry of the perovskite-type oxides $La_{1-x}Sr_xCoO_{3-\delta}$. *J. Sol. St. Chem* **1989,** *80*, 102-111.
**(73)** Zohourian, R.; Merkle, R.; Maier, J. Bulk Defect Chemistry of PCFC Cathode Materials: Discussion of Defect Interactions *ECS Trans.* **2017,** *77* (10), 133-138.
**(74)** Merkle, R.; Maier, J. How Is Oxygen Incorporated into Oxides? A Comprehensive Kinetic Study of a Simple Solid-State Reaction with $SrTiO_3$ as a Model Material. *Angew. Chem. Int. Ed.* **2008,** *47*, 3874-3894.
**(75)** McLachlan, D. S.; Blaszkiewicz, M.; Newnham, R. E. Electrical Resistivity of Composites. *J. Am. Ceram. Soc.* **1990,** *73*, 2187-2203.
**(76)** Stauffer, D. *Percolation Theory*, Taylor & Francis: **1985**.
**(77)** Han, D. G.; Choi, G. M. Computer simulation of the electrical conductivity of composites: the effect of geometrical arrangement. *Solid State Ion.* **1998,** *106*, 71-87.
**(78)** Fonseca, F. C..; Muccillo, R. Impedance spectroscopy analysis of percolation in (yttria-stabilized zirconia)-yttria ceramic composites. *Solid State Ion.* **2004**, *166*, 157-165.
**(79)** Kim, D.; Miyoshi, S.; Tsuchiya, T.; Yamaguchi, S. Percolation conductivity in $BaZrO_3$–$BaFeO_3$ solid solutions. *Solid State Ion.* **2014,** *262*, 875-878.
**(80)** Rao, Y.; Zhong, S.; He, F.; Wang, Z.; Peng, R.; Lu, Y. Cobalt-doped $BaZrO_3$: A single phase air electrode material for reversible solid oxide cells. *Int. J. Hydrog. Energy* **2012,** *37*, 12522-12527.
**(81)** Rotschild, A.; Menesklou, W.; Tuller, H. L.; Ivers-Tiffée, E. Electronic Structure, Defect Chemistry, and Transport Properties of $SrTi_{1-x}Fe_xO_{3-y}$ Solid Solutions. *Chem. Mater.* **2006,** *18*, 3651-3659.

**(82)** Liu, Y.; Baumann, S.; Schulze-Kueppers, F.; Mueller, D. N.; Guillon, O. Co and Fe co-doping influence on functional properties of $SrTiO_3$ for use as oxygen transport membranes. *J. Eur. Ceram. Soc.* **2018,** *38*, 5058-5066.
**(83)** Bishop, S. R.; Stefanik, T. S.; Tuller, H. L. Defects and transport in $Pr_xCe_{1-x}O_{2-\delta}$: Composition trends. *J. Mater. Res,* **2012,** *27*, 2009-2016.
**(84)** Narasimhan, C. S.; Swamy, C. S. Studies on the solid state properties of the solid solution system $MgAl_{2-x}Fe_xO_4$. *Phys. Status Solidi* **1980,** *59*, 817-826.
**(85)** Yoshiasa, A.; Ohtaka, O.; Sakamoto, D.; Andrault, D.; Fukui, H.; Okube, M. Pressure and compositional dependence of electric conductivity in the $Mg_{1-x}Fe_xO_{1-\delta}$ (x=0.01–0.40) solid-solution. *Solid State Ion.* **2009,** *180*, 501-505.
**(86)** Koumoto, K.; Yamayoshi, K.; Yanagida, H. Electrical Conduction in $Co_{1-x}Mg_xO$. *J. Am. Ceram. Soc.* **1983,** *66*, 42-45.
**(87)** Nomura, K.; Kageyama, H. Transport properties of $BaZr_{0.8}Y_{0.2}O_{3-\delta}$ perovskite. *Solid State Ion.* **2007,** *178*, 661-665.
**(88)** Maier, J. *Physical Chemistry of Ionic Materials*, Wiley. **2004**.
**(89)** Mizusaki, J.; Yoshihiro, M.; Yamaguchi, S.; Fueki, K. Nonstoichiometry and defect structure of the perovskite-type oxides $La_{1-x}Sr_xFeO_{3-\delta}$. *J. Solid State Chem* **1985,** *58*, 257-266.
**(90)** Schober, T.; Bohn, H. G. Water Vapor Solubility and Electrochemical Characterization of the High Temperature Proton Conductor $BaZr_{0.9}Y_{0.1}O_{2.95}$. *Solid State Ion.* **2000,** *127*, 351-360.
**(91)** Wang, L.; Merkle, R.; Maier, J.; Acartürk, T.; Starke, U. Oxygen tracer diffusion in dense $Ba_{0.5}Sr_{0.5}Co_{0.8}Fe_{0.2}O_{3-\delta}$. *Appl. Phys. Lett.* **2009,** *94*.
**(92)** De Souza, R. A. Oxygen Diffusion in $SrTiO_3$ and Related Perovskite Oxides *Adv. Funct. Mater.* **2015,** *25*, 6326-6342.
**(93)** Papac, M.; Stefanović, V.; Zakutayev, A.; Hayre, R. O. Triple ionic–electronic conducting oxides for next-generation electrochemical devices. *Nat. Mater.* **2021,** *20*, 301-313.
**(94)** Gao, Z.; Mogni, L. V.; Miller, E. C.; Railsback, J. G.; Barnett, S. A. A perspective on low-temperature solid oxide fuel cells. *Energ. Environmen. Sci.* **2016,** *9*, 1062-1644.
**(95)** Jun, A.; Kim, J.; Shin, J.; Kim, G. Perovskite as a Cathode Material: A Review of its Role in Solid-Oxide Fuel Cell Technology. *Chem. Electro. Chem.* **2016,** *3*, 511-530.
**(96)** Hashim, S. S.; Liang, F.; Zhou, W.; Sunarso, J. Cobalt-Free Perovskite Cathodes for Solid Oxide Fuel Cells. *Chem. Electro. Chem.* **2019,** *6*, 3549-3569.
**(97)** Bucher, E.; Egger, A.; Ried, P.; Sitte, W.; Holtappels, P. Oxygen nonstoichiometry and exchange kinetics of $Ba_{0.5}Sr_{0.5}Co_{0.8}Fe_{0.2}O_{3-\delta}$. *Solid State Ion.* **2008,** *179*, 1032-1035.

**(98)** Bringley, J. F.; Scott, B. A.; Placa, S. J. L.; Boehme, R. F.; Shaw, T. M.; McElfresh, M. W.; Trail, S. S.; Cox, D. E. Synthesis of the defect perovskite series $LaCuO_{3-\delta}$ with copper valence varying from 2+ to 3+. *Nature* **1990,** *347*, 6417-6426.
**(99)** Alonso, J. A.; Martinez-Lope, M. J.; Garcia-Munoz, J. L.; Fernandez-Diaz, M. T. A structural and magnetic study of the defect perovskite $LaNiO_{2.5}$ from high-resolution neutron diffraction data. *J. Phys. Condens. Matter* **1997,** *9*.
**(100)** Goodenough, J. B. Covalency Criterion for Localized vs Collective Electrons in Oxides with the Perovskite Structure. *J. Appl. Phys.* **1966,** *37* (3), 1415-1422.
**(101)** Mori, S. Phase Transformation in Barium Orthoferrate, $BaFeO_{3-x}$. *J. Am. Ceram. Soc.* **1966,** *49*, 600-605.
**(102)** Zou, X. D.; Hovmöller, S.; Parras, M.; González-Calbet, J. M.; Vallet-Regi, M.; Grenier, J. C. The complex perovskite-related superstructure $Ba_2Fe_2O_5$ solved by HREM and CIP. *Acta Cryst.* **1993,** *A49*, 27-35.

# 1 Supplementary Information

## Hydration plots of B15SF and BFY20

The experimental results from TGA hydration experiments for B15SF and BFY20 are reported in **Figure A 1**.

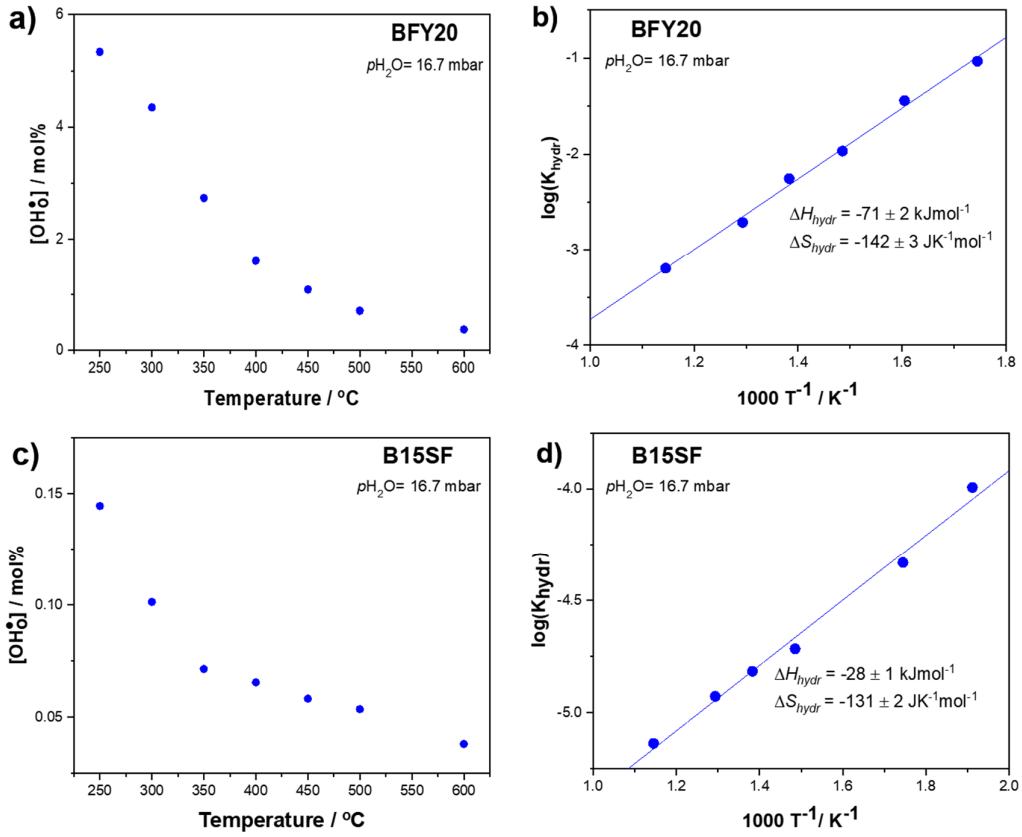


**Figure A 1** Proton concentration vs temperature and van't Hoff plots of (a-b) BFY20, and (c-d) B15SF.

## Hydration plots of BZYFe solid solution series

The experimental results from TGA hydration experiments for BZYF0, BZYF06, BZYF10, BZYF20, BZYF50, BZYF80 are reported in **Figure A 2** and **Figure A 3**.

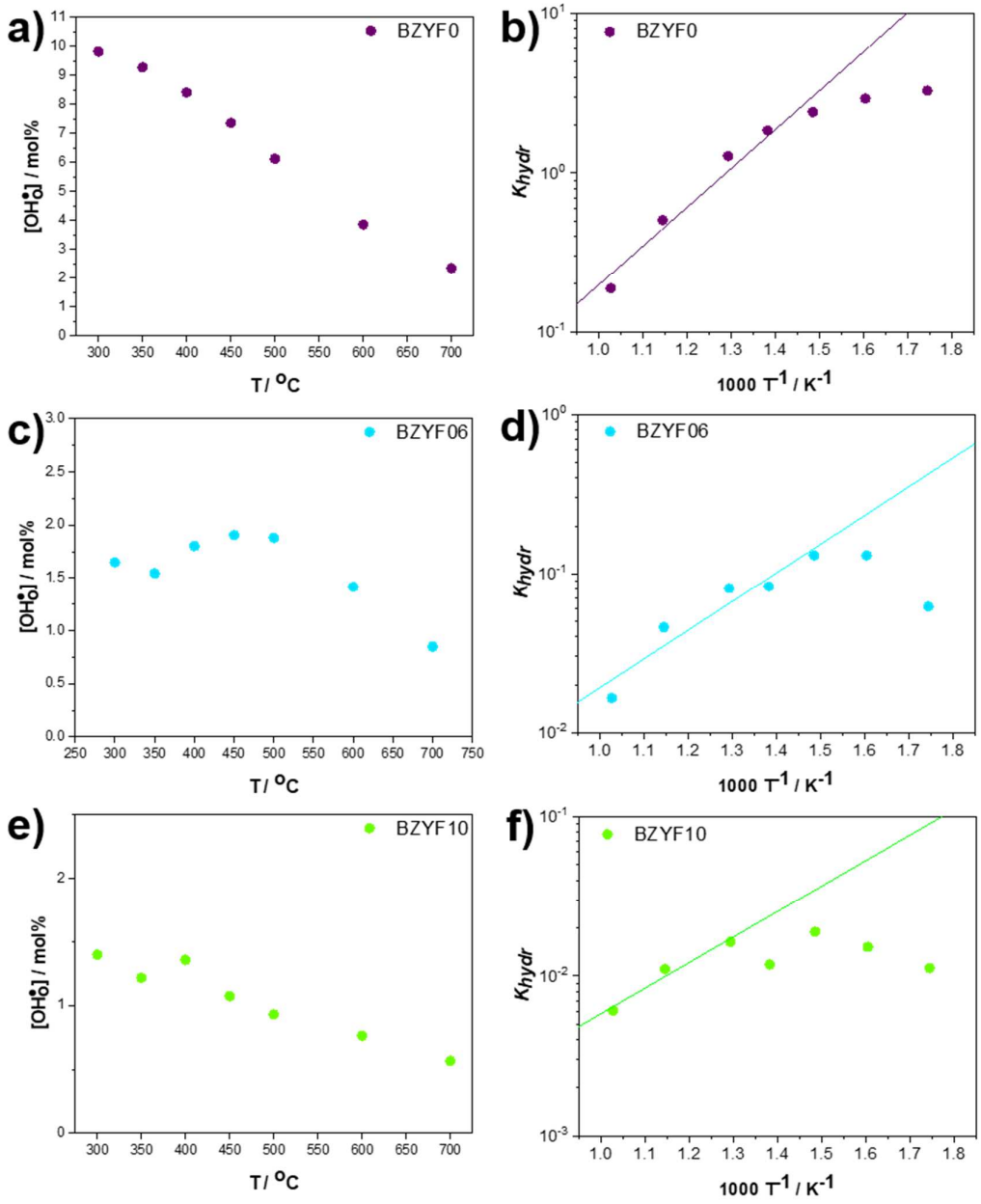


**Figure A 2** Proton concentration vs temperature and van't Hoff plots of (a-b) BZYF0, (c-d) BZYF06, and (e-f) BZYF10.

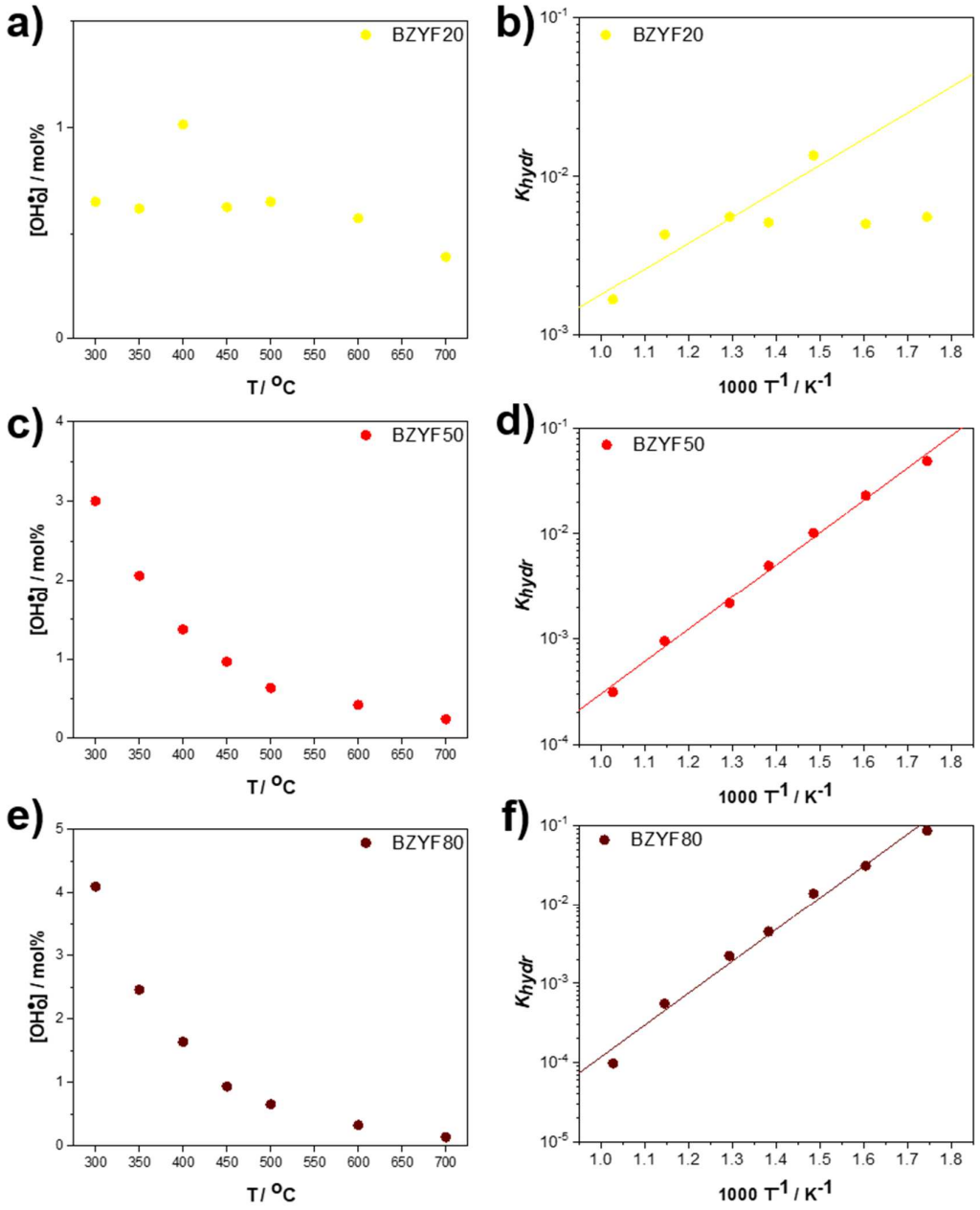


**Figure A 3** Proton concentration vs temperature and van't Hoff plots of (a-b) BZYF20, (c-d) BZYF50, and (e-f) BZYF80.

## ADDITIONAL PLOTS FOR THE MATERIALS INCLUDED IN SECTION 3.3

The experimental results from TGA hydration experiments of all the compositions included in **Section 3.3**.

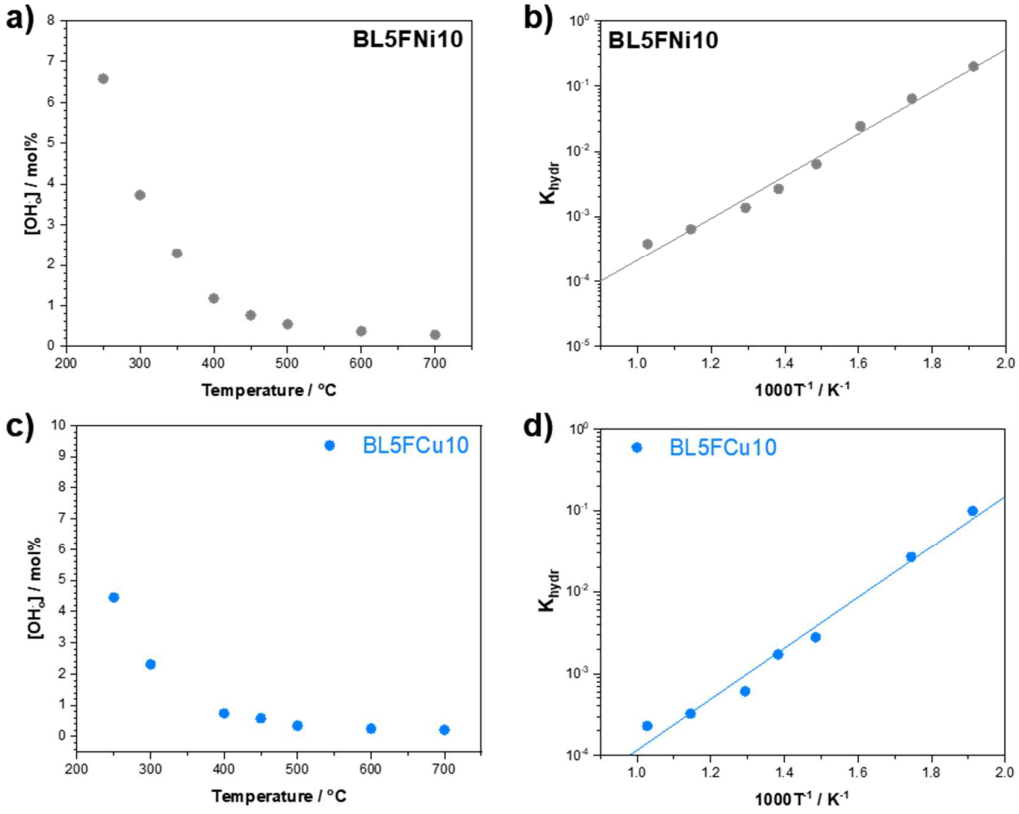


**Figure A 4** (a,c) Proton concentration vs temperature, (b,d) van't Hoff plots of BL5FNi10 and BL5FCu10. $\Delta H_{hydr}{}^{o}$, $\Delta S_{hydr}{}^{o}$ and $\Delta G_{hydr}{}^{o}$ are included in **Table 9**.

The following part is devoted to: (i) Arrhenius plots (ii) conductivity $pO_2$ dependences at 450 °C and 600 °C, (iii) Arrhenius plots of quenching experiments, for all the samples included in **Section 3.3**. All the data shown in the panels(a,b) are equilibrated at the corresponding temperatures and $pO_2$. The data in panels(c,d) belong to the samples quenched from 700 °C to RT. In the case of BL5F also the mobilities are given, since the hole concentration is known. The activation energies for equilibrated samples are extracted from the low-temperature region. The fact that there is a range with positive activation energies indicates that the *p*-type conductivity occurs via small polaron hopping, as typical for most Fe perovskites (apart from fully stoichiometric $SrFeO_3$). As the oxygen exchange reaction is not frozen-in, these are effective activation energies

comprising the hole migration barrier as well as the temperature dependence of the hole concentration (at high $T$ the latter dominates, leading to an apparently negative activation energy). In the case of the samples measured with frozen-in oxygen stoichiometry the activation energies refer solely to the hole migration barrier.

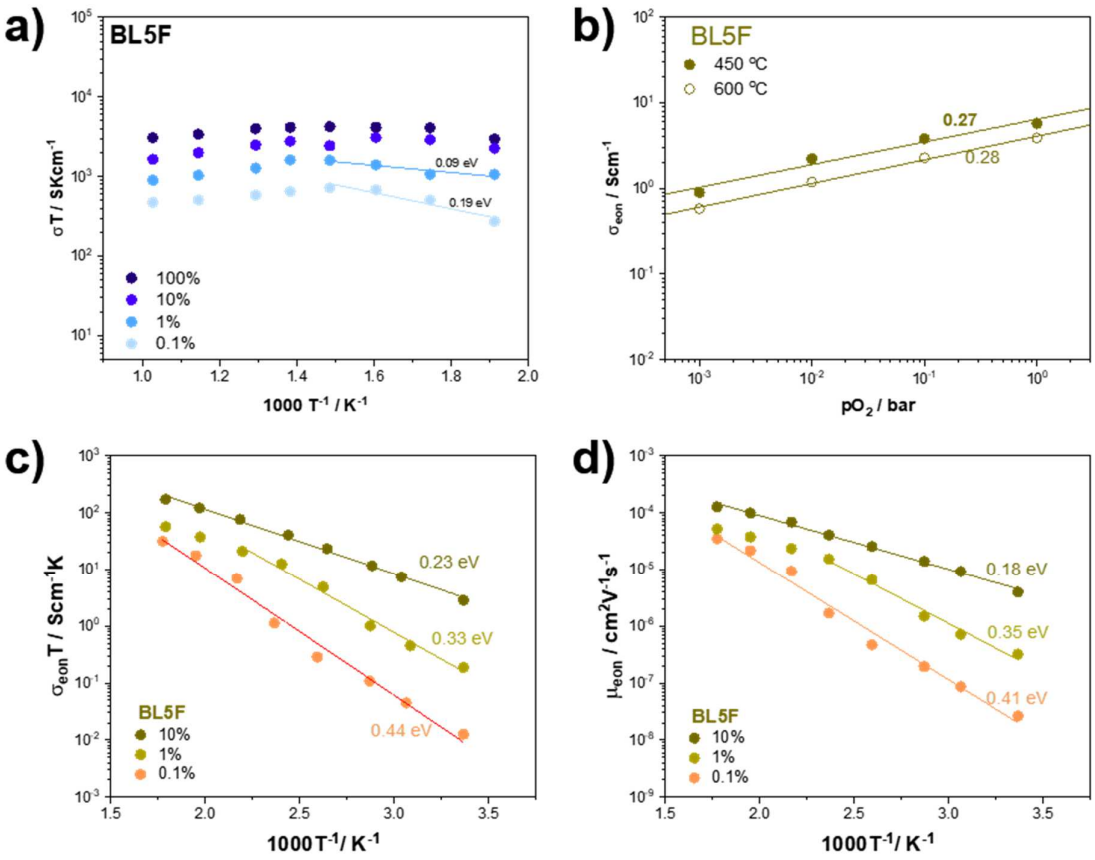


**Figure A 5** (a) Arrhenius plots at all the $pO_2$, (b) Conductivity vs $pO_2$ at 600 °C and 450 °C, the number near the regression line is the slope, (c) Arrhenius plot measured with frozen-in oxygen stoichiometry, (d) hole mobilities, for BL5F.

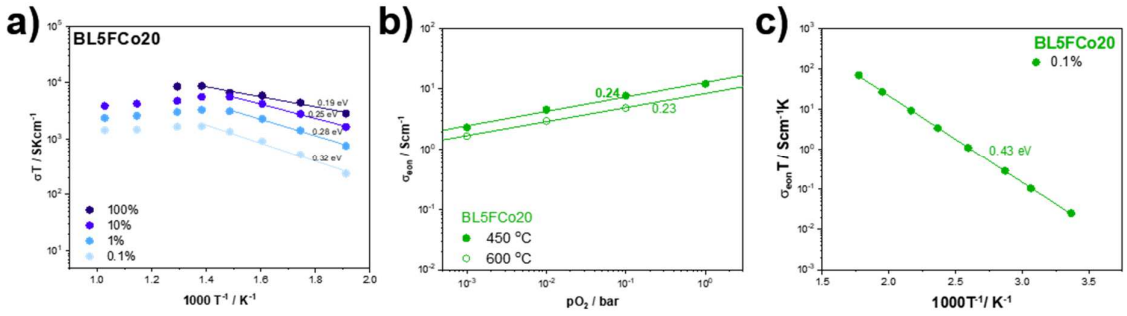


**Figure A 6** (a) Arrhenius plots at all the measured $pO_2$, (b) Conductivity vs $pO_2$ at 600 °C and 450 °C, the number near the regression line is the slope, (c) Arrhenius plot measured with frozen-in oxygen stoichiometry, of BL5FCo20.

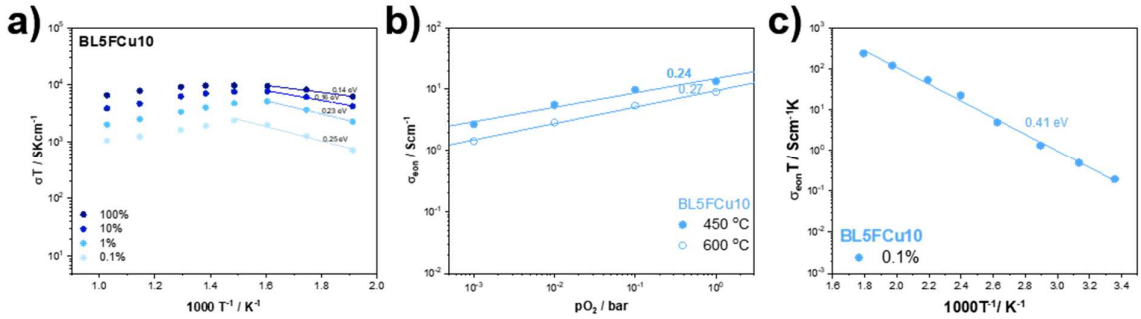


**Figure A 7** (a) Arrhenius plots at all the measured $pO_2$, (b) Conductivity vs $pO_2$ at 600 °C and 450 °C, the number near the regression line is the slope, (c) Arrhenius plot measured with frozen-in oxygen stoichiometry, of BL5FCu10.

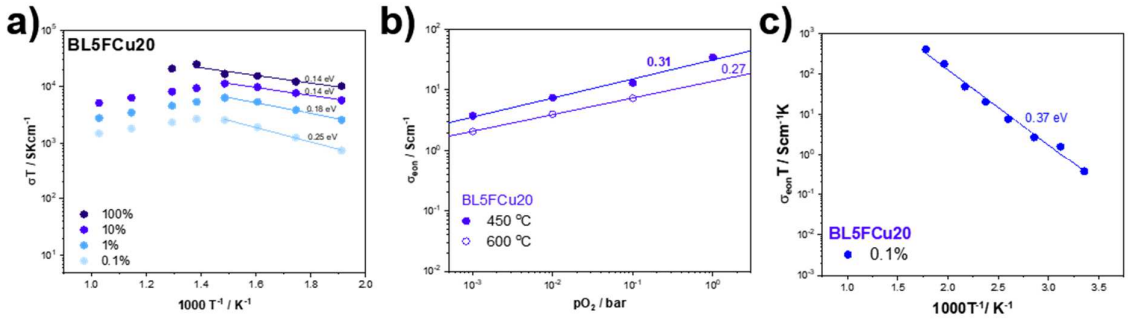


**Figure A 8** (a) Arrhenius plots at all the measured $pO_2$, (b) Conductivity vs $pO_2$ at 600 °C and 450 °C, the number near the regression line is the slope, (c) Arrhenius plot measured with frozen-in oxygen stoichiometry, of BL5FCu20.

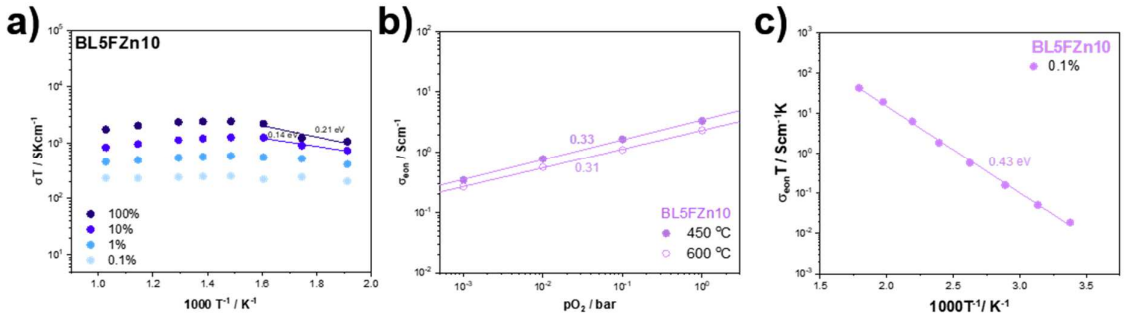


**Figure A 9** (a) Arrhenius plots at all the measured $pO_2$, (b) Conductivity vs $pO_2$ at 600 °C and 450 °C, the number near the regression line is the slope, (c) Arrhenius plot measured with frozen-in oxygen stoichiometry, of BL5FZn10.

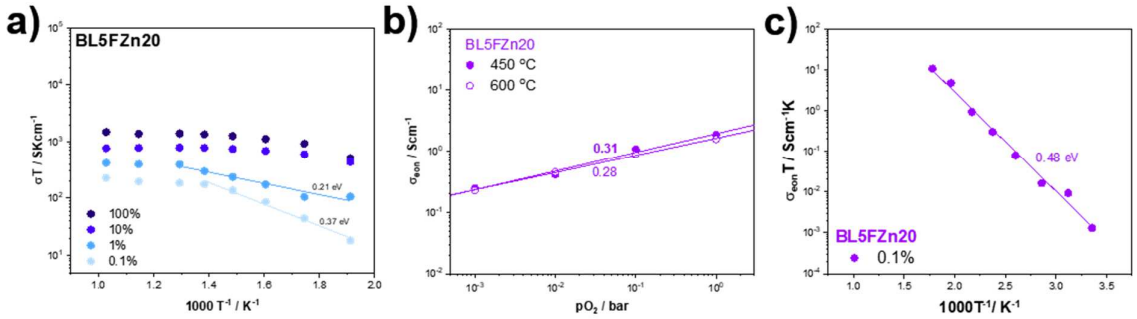


**Figure A 10** (a) Arrhenius plots at all the measured $pO_2$, (b) Conductivity vs $pO_2$ at 600 °C and 450 °C, the number near the regression line is the slope, (c) Arrhenius plot measured with frozen-in oxygen stoichiometry, of BL5FZn20.

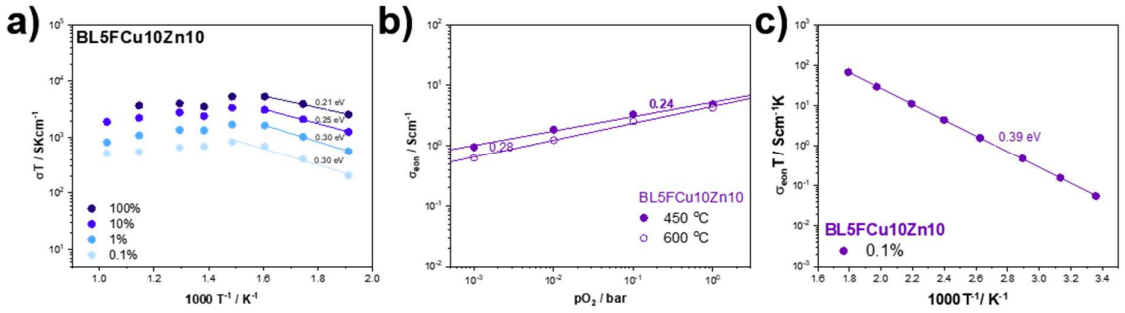


**Figure A 11** (a) Arrhenius plots at all the measured $pO_2$, (b) Conductivity vs $pO_2$ at 600 °C and 450 °C, the number near the regression line is the slope, (c) Arrhenius plot measured with frozen-in oxygen stoichiometry, of BL5FCu10Zn10.

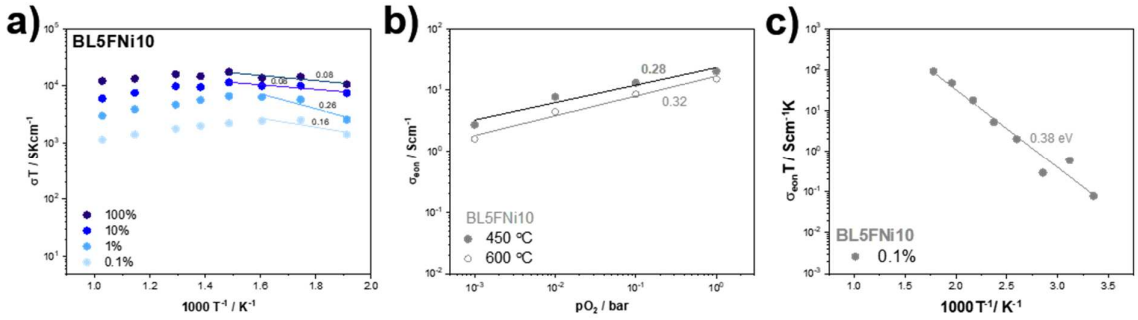


**Figure A 12** (a) Arrhenius plots at all measured the $pO_2$, (b) Conductivity vs $pO_2$ at 600 °C and 450 °C, the number near the regression line is the slope, (c) Arrhenius plot measured with frozen-in oxygen stoichiometry, of BL5FNi10.

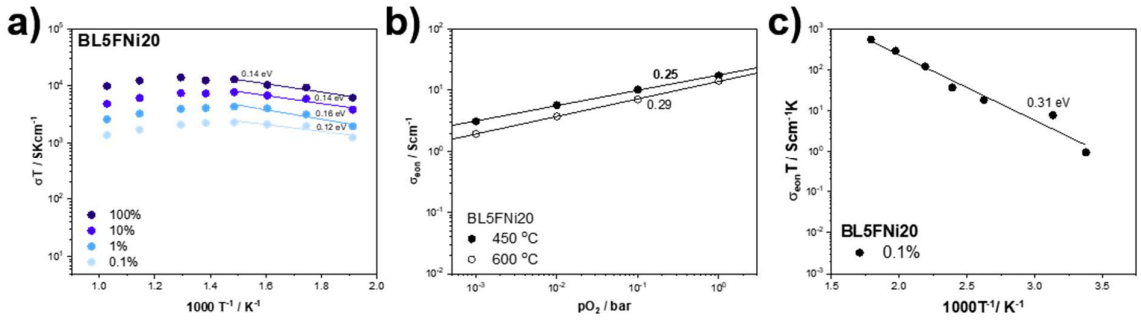


**Figure A 13** (a) Arrhenius plots at all measured the $pO_2$, (b) Conductivity vs $pO_2$ at 600 °C and 450 °C, the number near the regression line is the slope, (c) Arrhenius plot measured with frozen-in oxygen stoichiometry, of BL5FNi20.

## ADDITIONAL PLOTS FOR THE MATERIALS INCLUDED IN SECTION 3.4

The experimental results from TGA hydration experiments of all the compositions included in **Section 3.4** are given here. The hydration values for $\Delta H_{hydr}{}^{o}$, $\Delta S_{hydr}{}^{o}$ and $\Delta G_{hydr}{}^{o}$ are included in **Table A 1**.

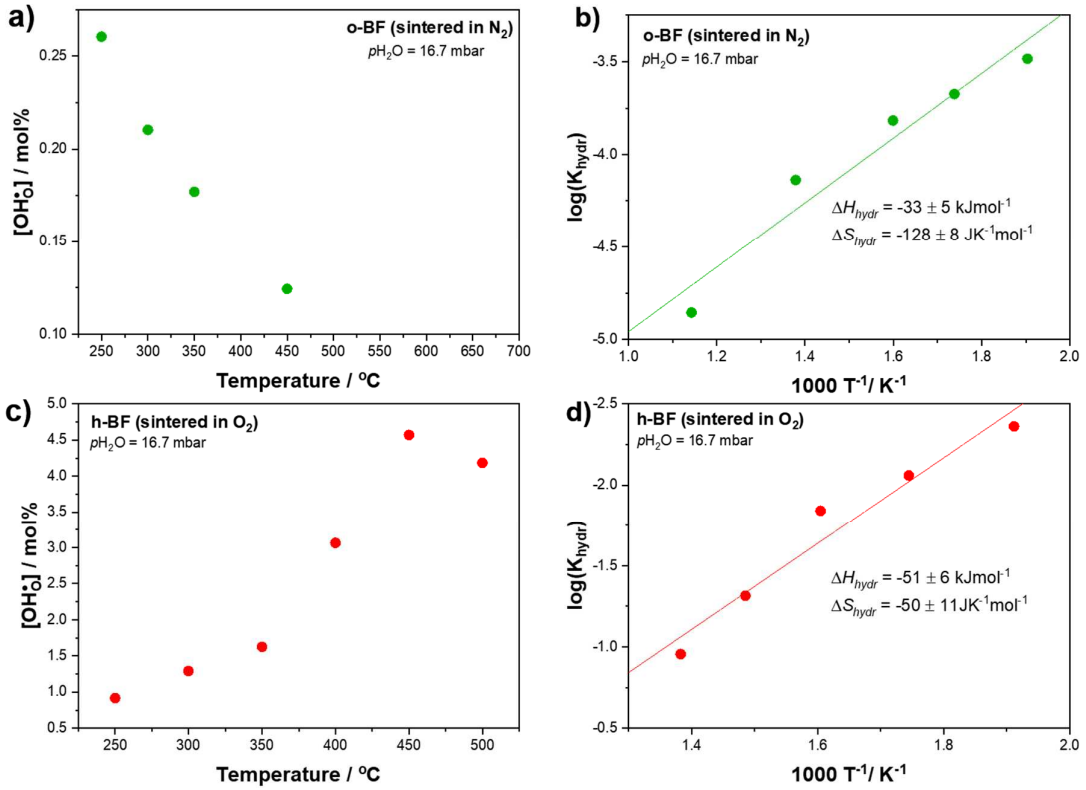


**Figure A 14** (a-b) Proton concentration vs temperature and van't Hoff plots of o-BF, and (c-d) h-BF.

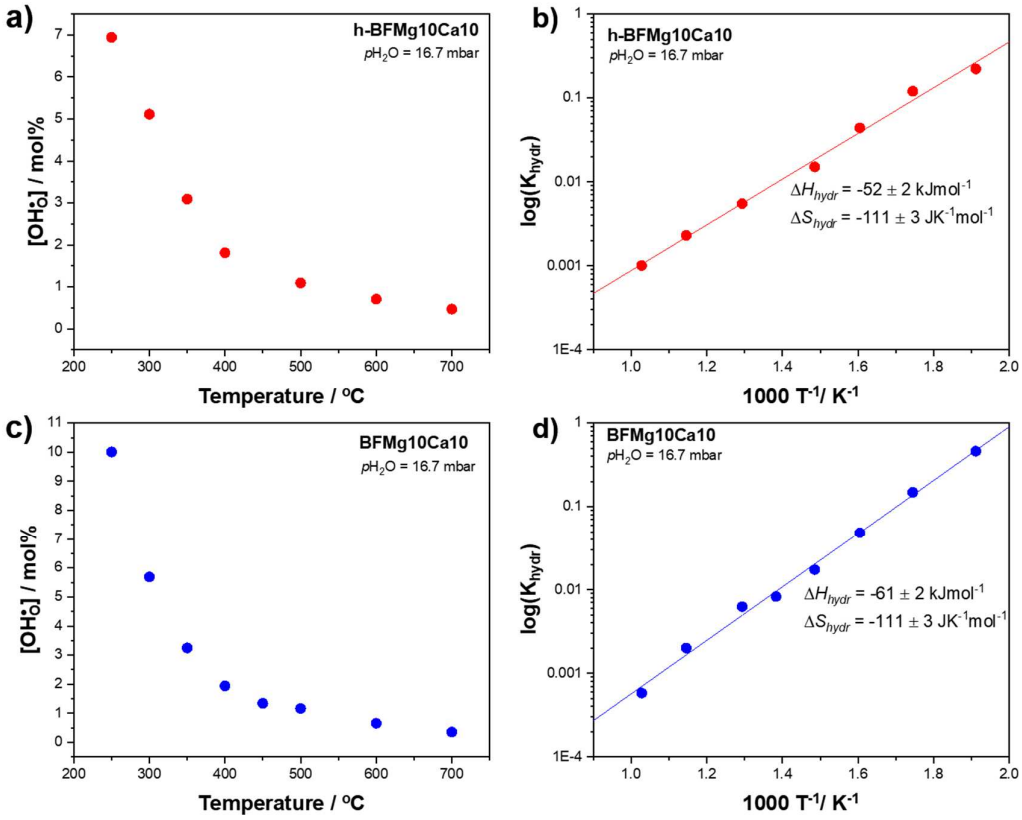


**Figure A 15** Proton concentration vs temperature and van't Hoff plots of h-(a-b) BFMg10Ca10, and (c-d) BFMg10Ca10.

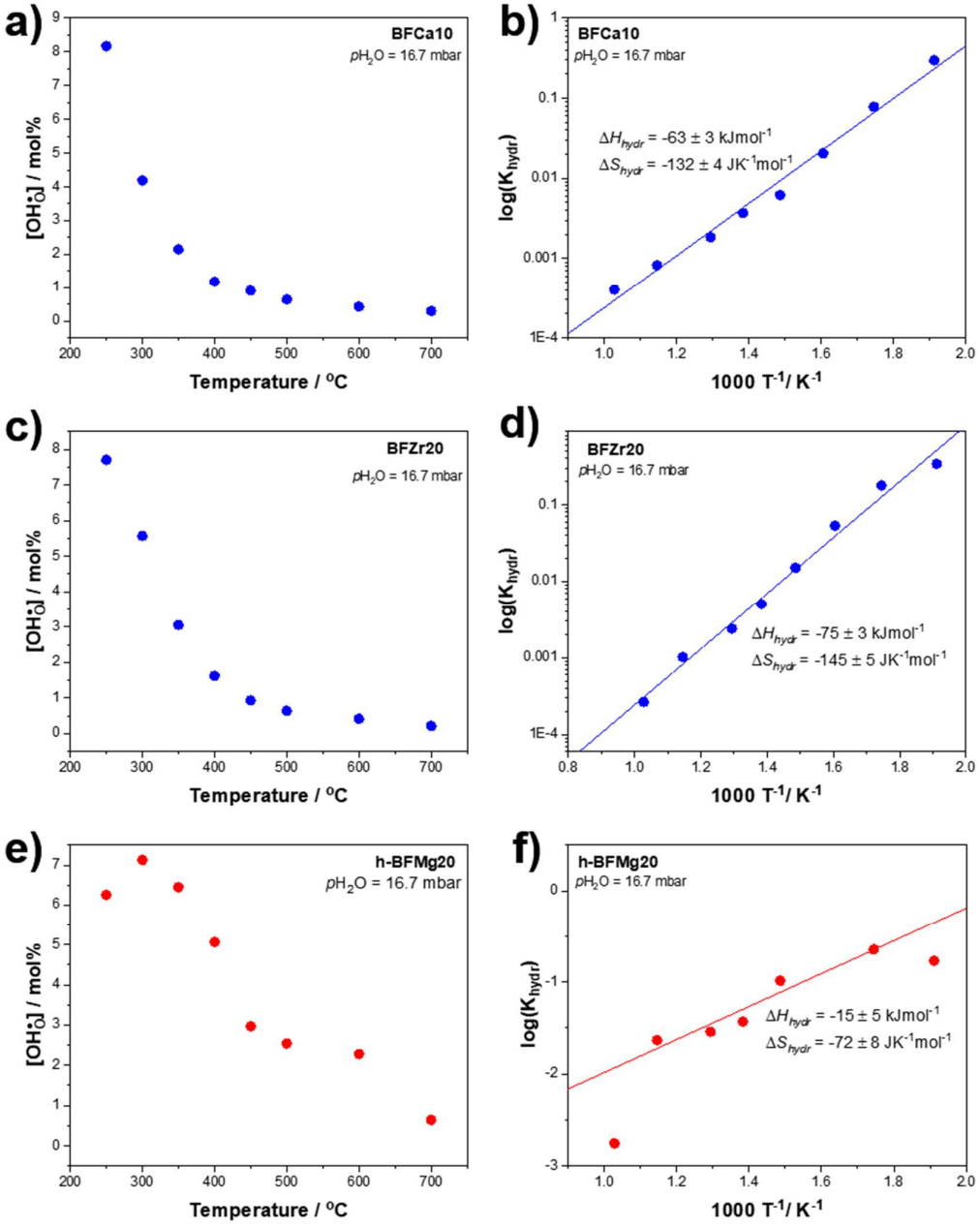


**Figure A 16** Proton concentration vs temperature and van't Hoff plots of (a-b) h-BFCa10, (c-d) BFZr20, and (e-f) h-BFMg20.

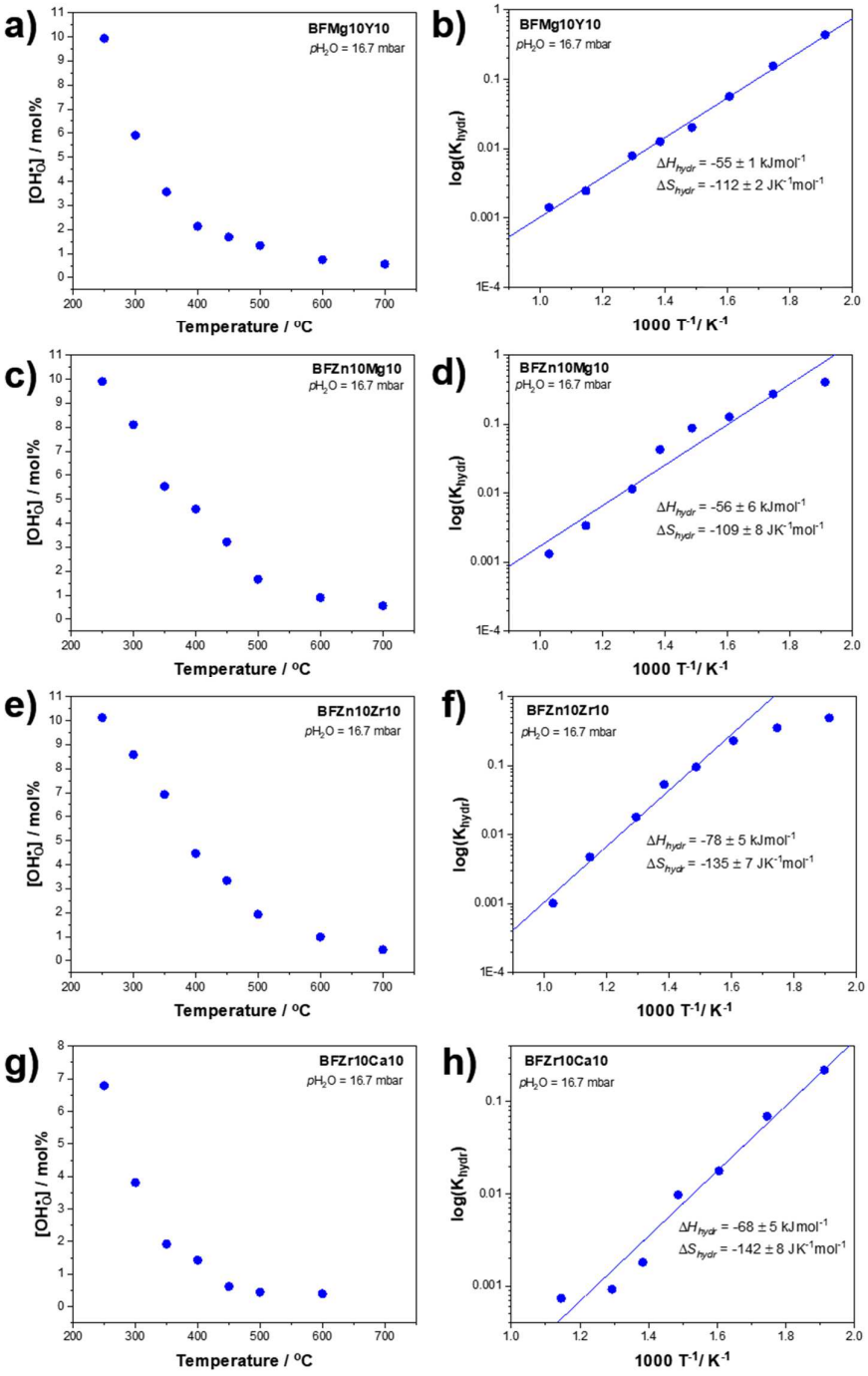


**Figure A 17** Proton concentration vs temperature and van't Hoff plots of (a-b) h-BFMg10Y10, (c-d) BFZn10Mg10, (e-f) BFZn10Zr10, and (g-h) BFZr10Ca10.

**Table A 1** Summary of the hydration thermodynamic parameters for the compositions included in **Section 3.4**, calculated from the respective van't Hoff plots (samples with frozen-in oxygenation reaction; all iron in 3+ state).

| samples | $\Delta H^{o}_{hydr}$ / kJmol$^{-1}$ | $\Delta S^{o}_{hydr}$ / JK$^{-1}$mol$^{-1}$ | $\Delta G^{o}_{hydr}$ / kJmol$^{-1}$ (700 K) |
|---|---|---|---|
| h-BF | -51 ± 6 | -50 ± 11 | -16 ± 3 |
| o-BF | -33 ± 5 | -128 ± 8 | 57 ± 3 |
| h-BFMg10Ca10 | -52 ± 2 | -111 ± 3 | 26 ± 1 |
| BFMg10Ca10 | -61 ± 2 | -123 ± 3 | 25 ± 1 |
| BFCa10 | -63 ± 3 | -132 ± 4 | 29 ± 2 |
| BFZr20 | -75 ± 3 | -145 ± 5 | 27 ± 2 |
| h-BFMg20 | -15 ± 5 | -72 ± 8 | 35 ± 2 |
| BFMg10Y10 | -55 ± 1 | -112 ± 2 | 23 ± 1 |
| BFZn10Zr10 | -78 ± 5 | -135 ± 6 | 17 ± 2 |
| BFZn10Mg10 | -56 ± 6 | -109 ± 8 | 20 ± 4 |
| BFZr10Ca10 | -68 ± 5 | -142 ± 8 | 31 ± 4 |